Usability and limitations of dimensionless scaling laws in Laser Powder Bed Fusion

Zur Erlangung des akademischen Grades einer

DOKTORIN DER INGENIEURWISSENSCHAFTEN (Dr.-Ing.)

von der KIT-Fakultät für Maschinenbau des
Karlsruher Instituts für Technologie (KIT)

angenommene

DISSERTATION

von

M. Sc. Theresa Hanemann

Tag der mündlichen Prüfung:	21.09.2022
Hauptreferent:	Prof. Dr.-Ing. Martin Heilmaier
Korreferentin:	Prof. Xinhua Wu

Kurzfassung

In den letzten Jahrzenten fand die Technologie des pulverbettbasierten Laserstrahlschmelzens (engl. Laser Powder Bed Fusion (LPBF)) neben der Prototypenfertigung zunehmend Anwendung in der industriellen Herstellung von Endprodukten. Um den damit gestiegenen Anforderungen an Bauteilqualität, Produktivität und Reproduzierbarkeit sowie der Erweiterung des verfügbaren Legierungs-Portfolios gerecht zu werden, müssen Prozessparameter für neue Legierungsysteme entwickelt und bereits bestehende Prozesse entsprechend den höheren Anforderungen und neuen Maschinenkonfigurationen angepasst werden. Auf Grund der Komplexität des pulverbettbasierten Laserstrahlschmelzens werden Prozessfenster üblicherweise in einem kosten- und zeitaufwendigen Trial-and-Error-Verfahren entwickelt. Ein möglicher Ansatz die experimentelle Komplexität zu reduzieren besteht darin, verschiedene Prozessparameter zu einer Variable zu gruppieren und den Effekt dieser Variable als Ganzes zu evaluieren. Dieses Vorgehen findet gängige Anwendung in Formulierungen für den Energieeintrag. Allerdings berücksichtigen diese Energieeinträge keine Unterschiede in den physikalischen Materialeigenschaften verschiedener Legierungen womit die Übertragbarkeit von Prozessparametern zwischen Legierungssystemen erschwert wird. Dimensionslose Skalierungsgesetze könnten hier einen Vorteil bieten, da sie die relevanten thermophysikalischen Materialeigenschaften mit einbeziehen und damit das Schmelzverhalten materialunabhängig beschreiben. In der vorliegenden Arbeit wurde die Anwendbarkeit der dimensionslosen Enthalpie H^* - Verhältnis aus der durch den Laser in das Material eingebrachten zu der zum Aufschmelzen benötigten Energie - zur Charakterisierung der Schmelzbadgeometrie und der Formulierung eines gemeinsamen Prozessfensters für verschiedene Werkstoffe untersucht. Dafür wurden einzelne Schmelzspuren in einem breiten Parameterbereich und mit verschiedenen Legierungen auf Basis von Ni (EN 2.4668), Fe (EN 1.2709, EN 1.4404), Ti (EN 3.7164) und Al (EN AC-43000) hergestellt und deren Schmelzbadmorphologie sowie Stabilität evaluiert. Die Untersuchungen zeigen, dass die dimensionslose Enthalpie alleine nicht ausreicht um die Schmelzbaddimensionen hinreichend zu beschreiben. Daher wurde der Einfluss der Wärmeverteilung ausgedrückt durch die Peclet Zahl Pe - Verhältnis aus Wärmeverteilung durch Konvektion zu Wärmeleitung - mit in den Untersuchungsrahmen aufgenommen. Bei konstanter dimensionsloser Enthalpie wurde eine nicht-monotone Abhängigkeit der Schmelzbadtiefe von der Peclet Zahl beobachtet. Bereiche niedriger und hoher Peclet Zahlen zeigten eine unterschiedliche Steigung und Vorzeichen dieser Abhängigkeit. Als Hypothese wurde aufgestellt, dass das unterschiedliche Verhalten auf eine Erhöhung der Wärmeverluste durch Wärmeleitung zusammen mit einer Umverteilung der Wärme innerhalb des Schmelzbades bei niedrigen Peclet Zahlen zurückgeführt werden kann. Für hohe Peclet Zahlen konnte eine quantitative Beziehung zwischen Peclet Zahl und Schmelzbadtiefe bei konstanter dimensionsloser Enthalpie aufgestellt werden. Basierend hierauf wurden zwei neue dimensionslose Kennzahlen zur Charakterisierung der Schmelzbadtiefe und -breite eingeführt

(H^*_{cd} und H^*_{cw}). Mit diesen beiden dimensionslosen Kennzahlen konnten die Schmelzbaddimensionen für die untersuchten Werkstoffe im Bereich des Tiefschweißens mit einem Fehler von $\pm$32% und $\pm$20% für Schmelzbadtiefe und Schmelzbadbreite vorhergesagt werden. Des Weiteren konnte die Skalierung mit H^*_{cd} verwendet werden, um ein gemeinsames Prozessfenster für Fe-, Ni- und Ti-basierte Legierungen zu definieren. Das gefundene Prozessfenster konnte allerdings nicht für Al-basierte Legierungen verifiziert werden und weitere Forschung ist nötig um die beobachtete Abweichung zu erklären. Die Verwendung von H^*_{cd} zur Vorhersage des Prozessfensters ist in einem materialspezifischen Bereich der Scangeschwindigkeit limitiert. Wobei der Verlust der Anwendbarkeit von H^*_{cd} zur Tiefenvorhersage bei kleinen Peclet Zahlen das untere und der Beginn des Humping-Phänomens das obere Limit darstellt.

Abstract

Over the past decades, Laser Powder Bed Fusion (LPBF) has evolved from a prototyping to a manufacturing technology leading to increasing requirements on part quality, productivity, and reproducibility. In addition, there is a high interest in extending the portfolio of available alloys. To satisfy those demands, suitable processing parameters have to be developed for new alloy systems and existing processes have to be adapted for refined requirements or new machine systems. Due to the complexity of the LPBF process, development of process windows is often done on a trial-and-error basis which can be time and cost intensive. One approach to reduce experimental complexity is to group process parameters and evaluate their combined effect, such as done with energy input definitions. However, those energy input expressions do not contain physical material properties, making it difficult to transfer process parameters to varying materials. Dimensionless scaling laws could help to overcome this drawback by including relevant thermophysical material parameters. In this work, the usability of the dimensionless enthalpy H^* - relating the energy input from the laser to the energy necessary for melting - to characterize melt pool geometry and to formulate a common process window for different materials was investigated. Single line scans were produced and evaluated with respect to their stability and melt pool morphology in a broad range of processing parameters for a variety of alloy systems based on Ni (EN 2.4668), Fe (EN 1.2709, EN 1.4404), Ti (EN 3.7164), and Al (EN AC-43000). The dimensionless enthalpy alone is shown to be not feasible to correlate melt pool dimensions. Therefore, the influence of heat distribution characterized by the Peclet number Pe - defining the ratio between heat convection and heat conduction - was included within the investigations. At constant dimensionless enthalpy melt pool depth was observed to vary non-monotonically with changing the Peclet number. The relation differed in slope and sign for high and low Peclet number regions. It was hypothesized that this variation is caused by an increase in heat loss due to conduction as well as redistribution of heat inside the molten material at low Peclet numbers. A quantitative scaling of melt pool width and depth in relation to the Peclet number was derived for high Peclet numbers. Two new dimensionless numbers were introduced based on this scaling to characterize melt pool depth and width (H^*_{cd} and H^*_{cw}). With those two dimensionless numbers, melt pool dimensions were observed to follow common trend lines for all investigated alloys with an prediction error in keyhole mode of $\pm$32% and $\pm$20% for melt pool depth and width, respectively. Furthermore, the scaling of H^*_{cd} with melt pool depth enables the definition of a common process window for Fe-, Ni- and Ti-based alloys. However, the proposed process window range could not be verified for the Al-based alloy and further research is necessary to understand the different behavior. The use of H^*_{cd} to determine a process window was found to be valid only in a material specific velocity range limited by the loss of validity of H^*_{cd} to predict melt pool depth at small Peclet numbers as lower and the onset of the humping phenomenon as upper bound.

Contents

List of abbreviations and symbols

Abbreviations

AM	Additive Manufacturing
Bal	Balance
CAD	Computer Aided Design
CNC	Computerized Numerical Control
EPLT	Effective powder layer thickness
GUI	Graphical user interface
HS	High speed
IR	Infrared
LPBF	Laser Powder Bed Fusion
PBF	Powder Bed Fusion
PS	Parameter set
RT	Room temperature
STL	Standard Tessellation Language
UTS	Ultimate tensile strength
WSA	Weld Seam Analyzer

Symbols

A	Absorptivity	
AED	Areal Energy Density	$\mathrm{J/m^2}$
a	Laser focus diameter	µm
α_L	Angle of deflection	°
c_p	Specific heat capacity	$\mathrm{J/(kg\,K)}$
D	Thermal diffusivity	$\mathrm{m^2/s}$
D_l	Thermal diffusivity at $T_{liquidus}$	$\mathrm{m^2/s}$
d	Melt pool depth	µm
d^*	Dimensionless melt pool depth	
d_l^*	Lower critical dimensionless melt pool depth	
d_p^*	Predicted dimensionless melt pool depth	
d_t	Total melt pool depth	µm
d_t^*	Dimensionless total melt pool depth	
d_u^*	Upper critical dimensionless melt pool depth	

ΔT	Temperature difference between $T_{solidus}$ and T_0	K
ΔT_{max}	Temperature difference between T_c and $T_{solidus}$	K
η	Dynamic viscosity	$\mathrm{mPa\,s}$
η_m	Multi track efficiency for melting	
η_v	Multi track efficiency for vaporization	
Fo	Fourier number	
γ	Kinematic viscosity	$\mathrm{m^2/s}$
H^*	Dimensionless enthalpy	
H^*_{cd}	Depth corrected dimensionless enthalpy	
H^*_{cdl}	Lower critical depth corrected dimensionless enthalpy	
H^*_{cdu}	Upper critical depth corrected dimensionless enthalpy	
H^*_{cw}	Width corrected dimensionless enthalpy	
h	Melt pool height	$\mu\mathrm{m}$
h^*	Dimensionless melt pool height	
h_{LEV}	Energy input per volume	$\mathrm{J/m^3}$
h_d	Hatch distance	$\mu\mathrm{m}$
h_f	Latent heat for melting	$\mathrm{J/kg}$
h_l	Hatch length	mm
h_m	Effective melting height	$\mu\mathrm{m}$
h_{pow}	Effective powder layer thickness	$\mu\mathrm{m}$
$h_{pow,Ref}$	Powder layer height above reference surface	$\mu\mathrm{m}$
h_s	Enthalpy for melting	$\mathrm{J/kg}$
h_v	Enthalpy for vaporization	$\mathrm{J/kg}$
i	Number of dimensionless numbers	
k	Thermal conductivity	$\mathrm{W/(m\,K)}$
k_l	Thermal conductivity at $T_{liquidus}$	$\mathrm{W/(m\,K)}$
L	Characteristic length	m
L_d	Thermal diffusion length	$\mu\mathrm{m}$
L^*_d	Normalized thermal diffusion length	
L_F	Lack-of-fusion number	
LED	Linear Energy Density	$\mathrm{J/m}$
l	Melt pool length	$\mu\mathrm{m}$
l_t	Nominal layer thickness	$\mu\mathrm{m}$
l^*_t	Dimensionless nominal layer thickness	$\mu\mathrm{m}$
Ma	Marangoni number	

m_{H_2O}	Mass in water	kg
m_{air}	Mass in air	kg
n	Number of independent variables	
Oh	Ohnesorge number	
P	Laser power	W
P_R	Reference laser power	W
Pe	Peclet number	
Pe_{MP}	Melt pool Peclet number	
Φ	Contact width angle	°
ψ	Contact angle	°
Q^*	Non-dimensional heat input	
q	Number of fundamental units	
R	Aspect ratio	
Re	Reynolds number	
ρ	Density	$\mathrm{kg/m^3}$
ρ_{H_2O}	Density of water	$\mathrm{kg/m^3}$
ρ_{PB}	Relative powder bed density	%
ρ_r	Relative density	%
ρ_s	Measured density of solid	$\mathrm{kg/m^3}$
s	Number of layers	
σ	Surface tension	mN/m
T	Temperature	K
T_0	Initial temperature	K
T_b	Boiling temperature	K
T_c	Maximum surface temperature	K
$T_{liquidus}$	Liquidus temperature	K
T_s	Surface temperature	K
$T_{solidus}$	Solidus temperature	K
t	Interaction time	s
Θ	Keyhole front wall angle	°
U	Characteristic velocity	m/s
u	Scan speed	mm/s
u_0	Critical speed	mm/s
u_{Hump}	Critical humping speed	mm/s
u_{MP}	Velocity of liquid metal within melt pool	mm/s

u_R	Reference scan speed	$\mathrm{mm/s}$
V	Volume	m^3
VED	Volume Energy Density	$\mathrm{J/m}^3$
We	Weber number	
w	Melt pool width	µm
w^*	Dimensionless melt pool width	
w_{KH}	Keyhole diameter	µm
$z_{solidus}$	Z-coordinate of solidus isotherm	µm

1 Introduction

In the past 30 years, Additive Manufacturing (AM) has matured from prototyping to an industrial technology. While functional prototypes - with 19.3% - represented the largest share in AM applications in 2011 [1], they got outpaced by parts produced for end use applications in 2020 by an application share of 24.6% to 30.9% [2]. With a production volume of more than half a million parts per day clear aligners from Align Technology is considered a success story for mass customization using AM within the polymer sector [3]. While industrialization of polymer AM faces lower system and production costs, metal AM has also been successfully integrated into end user products - demonstrated by BMW by the inclusion of a metal AMed roof bracket into serial production of the BMW i8 Roadster [4]. Despite stagnation of metal AM systems revenue growth in the last years [2] and slowed economic growth due to the COVID-19 pandemic, annual growth rates of 24% till 2025 are expected [5]. Besides its negative influence on world economics, the pandemic might also give new chances to broaden AM applications with businesses questioning traditional supply chains, thereby fostering industrialization of AM [6].

According to the AMPOWER Report [5], Laser Powder Bed Fusion (LPBF), which uses a powder bed as feedstock and a laser to selectively melt specific regions of powder, is still the dominant metal AM technology with applications ranging from medical [7, 8] and aerospace [9, 10] to tooling [11, 12] and customer luxury goods [13]. However, there are still drawbacks of LPBF limiting a widespread utilization and industrialization, such as restricted build volumes, a necessity of post-processing to reduce surface roughness and residual stresses, as well as limited standardization [14]. Furthermore, the range of commercially available alloys for LPBF is mainly limited to cast Al alloys, selected steels, Ti6Al4V and commercially pure Ti, Ni-superalloys, and some Cu-alloys. However, to introduce new alloy systems into the LPBF market a feasible process window has to be found for each new material. In addition, process parameters have to be adapted for different machine systems. This is commonly done using experiment-based trial-and-error strategies which are time and resource consuming. The same applies to established alloy systems where process parameters are constantly under revision to enhance production quality and/or speed, which are both critical factors for the industrialization of AM. In general, there does not exist one optimum set of process parameters for every use case and they have to be carefully selected and adapted.

To enable process developers and application engineers to select suitable processing parameters, three different strategies can be applied: 1. Fast screening techniques with creation of dimensional process maps [15–17], 2. Simulation of melt pool dimensions and stability [18–22], 3. Process parameter selection from scaling law based dimensionless process maps [23–31]. In the first case, typically, a high number of small scale samples which can be evaluated in a timely manner are built with a wide range of process parameter combinations to give first

estimations of properties and determine a parameter subspace for more detailed investigations [16]. Instead of three dimensional parts, single scan tracks can be utilized for fast screening of suitable process parameter combinations, further reducing material waste and build time [15]. Satisfactory process parameter combinations can then be transferred and additional parameters relevant for three dimensional parts, such as hatch distance, can be adapted based on knowledge of melt pool size from single scan track experiments. Although those fast screening techniques certainly reduce development time and costs, experiments have to be repeated for each material investigated and changes in hardware setting, e.g., laser beam size. In the second approach, material and machine specific properties can be included to derive suitable processing parameter combinations prior to experimental investigation. In addition, numerical models enable further insights into physical phenomena and melt pool characteristics that are difficult or impossible to observe experimentally, such as melt pool convection [18, 32], temperature distribution [33], and solidification characteristics [34]. However, fast interaction times in LPBF and small length scales make accurate simulations quite challenging and time consuming [35]. Furthermore, models and their simplifications have to be validated experimentally, introducing additional costs to computing time and hardware. Finally, the application of dimensionless scaling laws to connect characteristic dimensionless numbers with process outcomes - such as single scan track dimensions [24–27] or relative part density [23, 28, 29] - has seen increased research interest. Those characteristic dimensionless numbers contain process parameters as well as material dependent thermophysical properties such that process outcomes can be described in a material and machine agnostic way. Thus, viable process parameter combinations can be transferred to new alloys, provided the knowledge about thermophysical properties of these new materials exists [30, 31]. Ideally, the chosen dimensionless numbers represent physical phenomena, thereby, giving additional process insights.

Within the presented work, this new approach is investigated and utilized to characterize melt pool dimensions and process windows for alloys with different thermophysical properties. The first part of this work concentrates on the applicability of the dimensionless enthalpy to scale melt pool width and depth of single scan tracks. Since melt pool depth can be closely related to stability and defect formation within single scan tracks, the viability of the dimensionless enthalpy to describe a material agnostic process window is investigated as a second aspect. Corresponding limitations are identified and discussed in context of their relevance for industrial processes. An outlook is given on the applicability of single scan track results to the fabrication of three dimensional parts.

2 Fundamentals

2.1 Laser Powder Bed Fusion (LPBF)

2.1.1 Process description

Laser Powder Bed Fusion (LPBF) is a subcategory of Powder bed fusion (PBF), which is one of the seven additive manufacturing techniques defined by the standards DIN EN ISO / ASTM 52900 [36]. Additive manufacturing enables the direct production of three-dimensional objects from virtual Computer Aided Design (CAD) data by layer-wise addition of material, in contrast to conventional subtractive or formative processes, such as Computerized Numerical Control (CNC) machining and casting. In the case of LPBF, the metallic feedstock material is provided as powder bed and the powder particles are fused selectively by a laser. The production sequence from CAD file to a finished three dimensional part is shown in Figure 2.1. The CAD model is converted into a Standard Tessellation Language (STL) file, which is then sliced into single layers. Those layers are processed in sequential cycles according to the provided machine and scanning parameters until the part is finished. Each cycle consists of the three following steps: First, a thin layer of powder, typically between $20\,\mu m$ to $100\,\mu m$ [37], is applied onto a build area by a recoater blade or roller. Subsequently, the powder is scanned by a laser according to the data from the slice file. Due to an increased absorptivity of most metals in the infrared (IR) spectrum, IR fibre lasers of $1060\,nm$ to $1080\,nm$ [37] wavelengths are most commonly used instead of CO_2 lasers. Beam diameters typically range from $50\,\mu m$ to $100\,\mu m$ [38]. Finally, the build platform is lowered and a new cycle starts. The components are built onto a base plate to prevent part distortion and ensure heat conduction from the process zone. Many commercial LPBF systems enable preheating of the base plate to further reduce thermal stresses during fabrication. To avoid oxidation caused by the high oxygen affinity of molten metals, especially

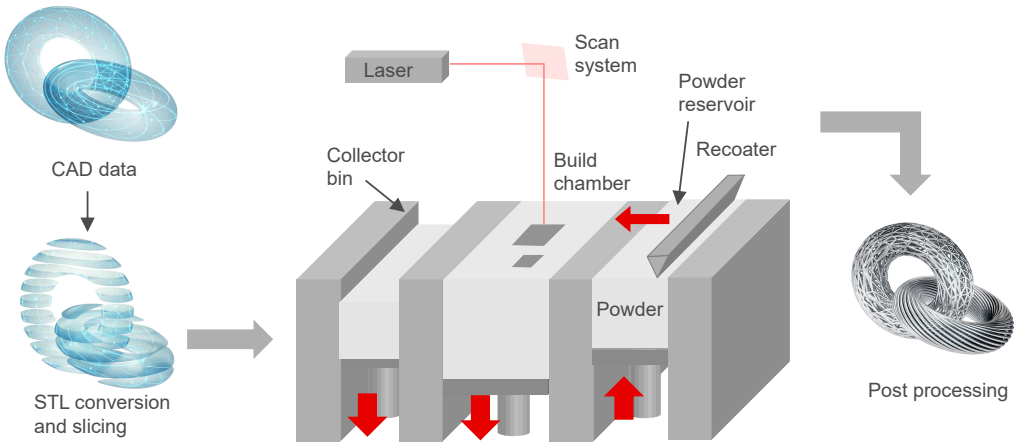

Figure 2.1: Schematic of LPBF system and virtual part preparation

Ti- and Al-alloys, and to reduce contamination of the process area by process by-products, such as spatter or smoke, an inert shielding gas, commonly Argon or Nitrogen, is guided over the process area. After processing, the part is removed from the build platform and post-processed, e.g., cleaned from remaining powder and surface and/or heat treated. Unused powder is collected in an overflow bin and can be reused. [37, 38, 40]

As production costs do not strongly scale with part complexity, LPBF is a suitable processing technique for small to medium lot production with high need for customization and freedom of design [39]. Therefore, it is especially suitable for medical applications with complex bionic implant designs that mimic natural bone structures [8] and topology optimized light weight components in the aerospace sector [10]. LPBF can also present a suitable manufacturing option in tooling, decreasing prototyping time and enabling fast tool design iterations [11]. Example parts made via LPBF for the different industry sectors are shown in Figure 2.2. Additional benefits of LPBF are reduced material waste and the ability to manufacture multi-component parts in a single manufacturing step, reducing the need for assembly. However, the layered buildup and powder adhesion lead to high surface roughness, typically between $7\,\mu m$ to $20\,\mu m$ [38]. Although lower surface roughness can in general be achieved by LPBF compared to other metal AM techniques such as electron beam melting or direct energy deposition, resulting surface quality is still insufficient for most applications [38, 40]. Therefore, post-process surface finishing treatments are necessary. Another drawback of LPBF is part deformation due to internal stresses introduced during manufacturing [40]. Furthermore, overhangs or cavities need to be braced by additional support structures to prevent deformation and enable heat conduction to the base plate. This enhances material waste and requires post processing to remove support structures. A major drawback for large scale industrialization of LPBF is the constrained build chamber volumes and low build rates [41]. However, there are now multi-laser systems commercially available to increase productivity by parallel scanning and larger machines are developed to increase build volumes. Another important point in the industrialization of LPBF is the range of fabricable metals and alloys. Today, alloys widely available for metal AM as powder feedstock

Figure 2.2: Example parts made by LPBF for different industrial applications; a) acetabular cup for hip implants made from Ti6Al4V, b) satellite bracket from AlSi10Mg, and c) mold with conformal cooling channels made from maraging steel

include Ni-based alloys, such as IN718[1] and IN939[1] , Ti-based alloys, mainly Ti6Al4V and commercially pure Ti, Al-based alloys, mainly AlSi10Mg, austenitic stainless steels, such as 316L, as well as tool steels, like M300 and H13, and some Cu-alloys [43–45]. However, research effort is taken to broaden the material selection for LPBF to high strength Al-alloys [46] or functional materials, e.g., shape memory or magnetic alloys [47].

2.1.2 Process parameters and terminology

LPBF is a quiet complex process with many process parameters influencing part microstructure [37], texture [48], mechanical properties [38], surface roughness [49], internal stresses [50], as well as build rates [51]. According to VanElsen [52], there can be easily named more than 50 parameters influencing the build process. Since a holistic discussion of all parameters is outside the scope of this work, only a selected group of parameters, important for the understanding of this thesis, will be explained in more detail in the following. The interested reader is referred to [52] and [53] for a complete review.

2.1.2.1 Energy input parameter

In LPBF, three dimensional parts are created layer by layer and track[2] by track with a laser melting neighboring scan lines to consolidate a layer. The different parameters regulating the energy input are shown in Figure 2.3. Laser power P and scan speed u determine the energy input to the material as well as the interaction time of this energy input. Their qualitative influence on physical process phenomena and their use in energy input models will be discussed in more detail in Section 2.2. The laser spot diameter a is defined here as the laser spot diameter in the build plane. Most LPBF systems use a laser with a Gaussian power distribution [38], although other beam shapes, such as top-hat or doughnut, have recently been tested to allow better heat input control [54, 55]. Together with the laser power P, the laser spot diameter a defines the laser intensity on the powder bed surface. The laser beam focus can be shifted out of the build plane to achieve larger beam sizes [56] The focal point can either be shifted below or above the build plane. Due to the converging or diverging nature of the beam at those two options, the melt pool shape can change significantly despite similar beam diameters at the build plane. For a focus shift above the build plane the material interacts with a divergent beam leading to shallower melt pools compared to a laser beam focused in the build plane. In contrast, for a focus shift below the build plane deeper melt pools are achieved due to the convergent nature of the beam. [51] Therefore, the focusing condition is also an important factor in LPBF.

[1] IN stands for Inconel, which is a trade name for a series of Ni-based alloys developed by Special Metals Corporation.

[2] The terms track, scan line and hatch will be used synonymous in this work.

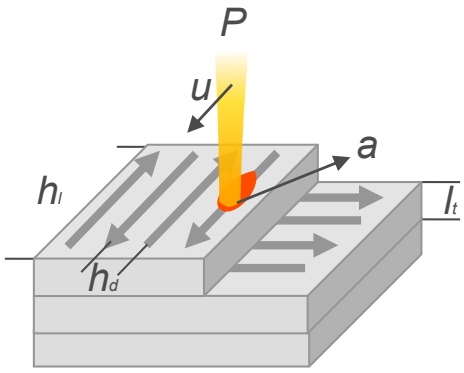

Parameter	Variable	Dimension
Laser power	P	W
Scan speed	u	mm/s
Laser spot diameter	a	mm
Hatch distance	h_d	mm
Layer thickness	l_t	mm
Hatch length	h_l	mm

Figure 2.3: Schematic of process parameters in LPBF

The hatch distance h_d describes the distance between the center points of two neighboring scan lines. To reduce the build time, h_d should be chosen as large as possible without creating lack-of-fusion porosity. This form of defect occurs when the molten tracks do not sufficiently overlap with neighboring or underlying scan lines. As a guideline, Meiners [57] recommends $h_d \approx 0.7a$ as a starting value to avoid lack-of-fusion porosity.

The nominal layer thickness l_t is defined here as the nominal value which the user determines in the pre-processing software. The build platform is lowered by this value after each processing cycle. Due to the lower density of the powder layer compared to the bulk material, the height of the consolidated layer is smaller than the height of the powder layer [57, 58]. Thus, to consolidate the material to the nominal layer thickness, a higher effective powder layer thickness (EPLT) is needed. In theory, the EPLT can be calculated as the quotient of l_t and the powder bed density ρ_{PB} [57, 59]. With typical powder bed densities around 50% this would lead to an effective powder layer thickness twice l_t. However, recent investigations by Wischeropp et al. [58], Mahmoodkhani et al. [60], and Bidare et al. [61] showed that the experimentally determined EPLT is higher than theoretically calculated. This is explained by not all powder particles contributing to the consolidated layer. In keyhole mode melting (see Section 2.2.1), some powder particles are blown away by the vapor plume or are expulsed from the melt pool as spatter [62–64]. With thicker l_t the amount of powder to be molten is increased, therefore the energy input has to be adapted to enable complete melting and connection to the underlying solid. A high l_t is beneficial in terms of built time, as the number of layers required to build a part is reduced, thus decreasing the recoating time. However, increasing l_t produces the so called stair-case effect [40], a decrease in resolution of geometrical features, such as slopes and curvatures. Additionally, surface roughness is increased [65].

The hatch length h_l, length of a scan track, influences the distribution of heat as well as the development of residual stresses. As a result of the local heating by the laser beam and corresponding steep temperature gradients, residual stresses are inherent to the LPBF process. The expansion of the heated material is constrained by the underlying colder solid, resulting in plastic deformation [66]. Upon cooling shrinkage of the material introduces tensile residual stresses. Since with increasing hatch length residual stresses increase, short hatches are preferred to avoid

part deformation [50]. Together with scan speed, the hatch length determines the time between consecutive hatches, thereby influencing the temperature distribution around consecutive tracks. Reducing the hatch length shortens the time between consecutive hatches to cool, resulting in increased heat accumulation. Which, in turn, increases melt pool dimensions [67]. Besides those direct process parameters, the scan strategy significantly influences part quality. It will therefore be discussed in the next paragraph.

2.1.2.2 Scan strategy

The scanning of a part area can be realized using different strategies with the most common ones shown in Figure 2.4. The simplest strategy, called **NoPattern**, consists just of alternating hatches as shown in Figure 2.4a. The scan lines can be scanned along the same as well as alternate directions. Although, alternate scanning is preferred to reduce jump times between hatch end points and diminish the effect of defect alignment at laser start and end points. The transition between subsequent hatches can be realized with or without Skywriting. Without Skywriting, the motion of the laser is started at the beginning and stopped at the end of each hatch including distances for acceleration and deceleration. As a result, the scan speed is nonconstant along the full length of a hatch, indicated by the color gradients in Figure 2.4a. Since the laser has already been decelerated at the end of a hatch it can directly jump to the start of a consecutive one, illustrated in the schematic by the short dotted turns. This is beneficial in terms of build time. However, since scan speed is nonconstant over the hatch length, energy input varies. When scan speed is low, the energy input increases, which can introduce keyhole porosity [68] (see Section 2.2.1). Skywriting can be applied to avoid variations of scan speed by adding a

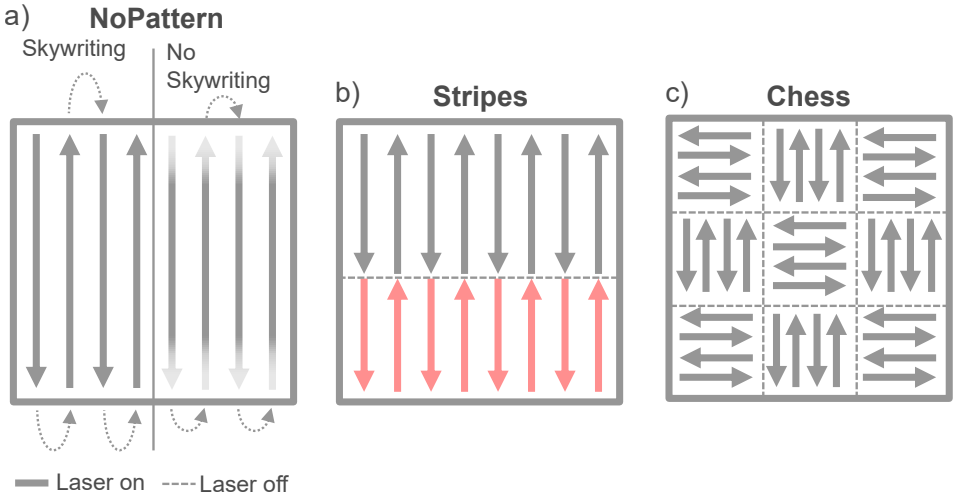

Figure 2.4: Schematic drawings of the most common scan strategies in LPBF; a) **NoPattern** with and without Skywiriting (color gradients of the hatches for the no Skywriting side indicate the reduced scan speed at those locations), b) **Stripes** with two stripes indicated by different colors, and c) **Chess** with 90° rotations between neighboring cells

distance for deceleration and acceleration before and after each hatch. During those additional scan segments, the laser is switched off, so that it is only active when scanning a hatch at set speed. The additional distance needed for deceleration and acceleration increases the turn time, but decreases the risk of keyhole porosity. As mentioned in the previous paragraph, the hatch length should be short to reduce thermal stresses. Therefore, a **Stripe** or **Chess** scan strategy is preferred for large area parts [40]. For the **Stripe** strategy (Figure 2.4b), the part is divided into stripes which are scanned sequentially. To avoid defects at the stripe borders, a stripe overlap between hatches of consecutive stripes is added (not shown in Figure 2.4b for simplicity). Instead of dividing the part into stripes, it can be divided into a checkerboard pattern (Figure 2.4c). The new parameters are then cell size, overlap between cells, rotation of hatches between cells, as well as the cell scan order. Independent of strategy, the scan pattern is commonly shifted and rotated between subsequent layers to avoid build up of defects [69], reduce anisotropy of mechanical properties due to texture [48], and decrease the build up of residual stresses [50]. With complex geometries of real components, some areas, such as corners or small walls, might get exposed with short hatches. The possibly resulting bulging and overheating of material in those areas can be avoided using either time homogenization or power reduction strategies. Time homogenization applies a certain wait time between consecutive hatches allowing them to cool down. For example, on EOS systems the applied wait time corresponds to the time required to scan a standard stripe's hatch. Since such homogenization increases the build time, power reduction can be applied if time is a critical requirement. For power reduction, the laser power of a hatch is reduced depending on its length.

2.1.2.3 Process boundary conditions

While the previous subsections considered process parameters and strategies, additional boundary conditions applied by the machine setup will be discussed in the following. A highly effective method to reduce residual stresses in parts is preheating of the base plate. Kempen et al. [70] managed to build crack free parts from M2[3] tool steel (EN 1.3343) with a preheating of $200\,^{\circ}\mathrm{C}$. Preheating the build platform does not only reduce residual stresses, but also decreases the energy input required for melting, thereby influencing part porosity [71]. The shielding gas flow distribution, speed, and type is another important parameter influencing part quality. Besides diminishing oxidation of the molten material, the shielding gas flow is necessary to transport spatter [63], ejected powder particles [64], metal vapor, and condensate from the process zone [62]. Melt spatters and powder particles could shield the laser beam and lead to unmelted regions if they travel through the process zone [69]. Anwar et al. [72] observed a decrease in UTS for AlSi10Mg when scanned in a direction oriented with the shielding gas flow in contrast to samples scanned against the shielding gas flow direction. This was attributed to the attenuation of the laser beam by spattered particles. Furthermore, if spatter particles reintegrate into the

[3] Composition in wt%: 0.86-0.94 C, 5.9-6.7 W, 4.7-5.2 Mo, 3.8-4.5 Cr, 1.7-2.1 V, $\leq$ 0.45 Si

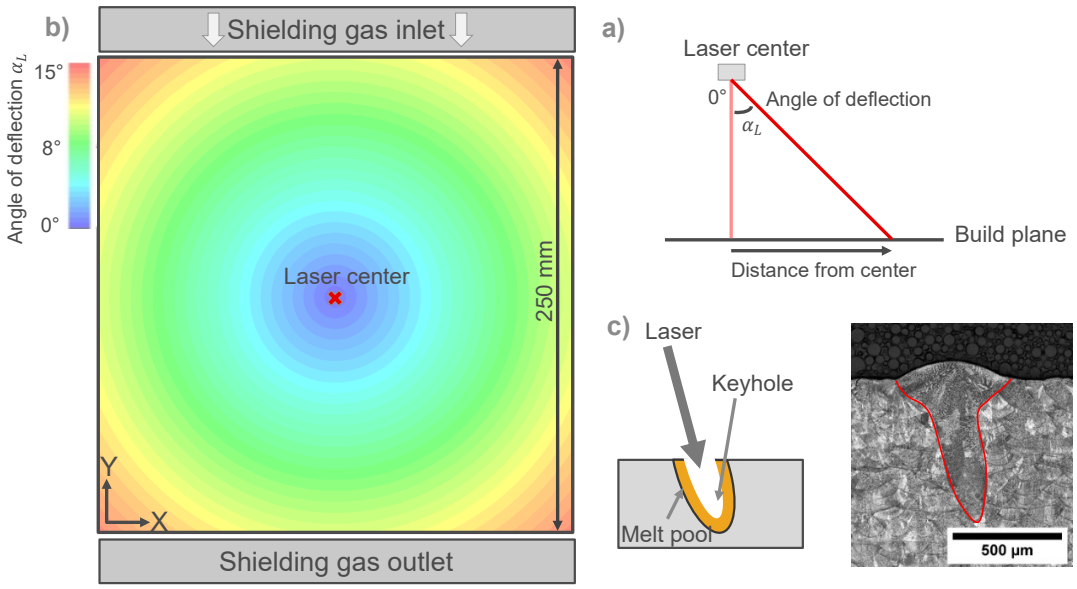

Figure 2.5: Schematic of the laser deflection over the build plane and its influence on melt pool geometry; a) definition of the angle of deflection α_L, b) angle of deflection as distribution over an EOS M290 build platform, and c) effect of inclination on melt pool geometry shown as schematic and exemplary micrograph for IN718

powder bed at areas that will be processed, the larger size of those particles prevents complete melting [69, 73]. Thus, they can lead to lack-of-fusion defects. Additionally, vaporized material from the melt pool can scatter and attenuate the laser beam, and thereby further decreases the laser beam intensity on the molten material. Reijonen et al. [74] observed a change in melting mode from keyhole to conduction with variation of shielding gas flow velocity for single line scans of 316L. They attributed their observation to the attenuation and scattering of the laser beam by the vapor and smoke from the keyhole if the shielding gas flow speed was too low to sufficiently remove the process by-products from the interaction zone. The importance of flow conditions on process quality was also shown by Ferrar et al. [75], who could reduce the location dependence of sample porosity by optimizing the gas flow inlet system. Ladewig et al. [73] proposed the following requirements for the shielding gas flow: 1. It should be homogeneously distributed in velocity and space over the whole build area; 2. It should be as high as possible without excessive redistribution of original powder particles; and 3. It should be close to the build platform. Along with the shielding gas flow distribution, the distance and orientation to the laser center are significant factors influencing homogeneity of part properties over the build plate. LPBF systems utilize an F-Theta lens[4] to enable constant focusing conditions throughout the build plane. However, with increasing distance from the laser center the laser impinges with a tilt on the powder layer. This inclination can be described by the angle of deflection α_L (Figure 2.5a). The angle of deflection over the build plate was exemplarily calculated for an

[4] An F-Theta lens is a special arrangement of lenses to correct for field curvature over a laser scan field to achieve a constant focus distance and focus diameter within the scan field.

EOS M290 in Figure 2.5b, reaching a maximum of about $15°$ in the corner locations. Since the laser impinges on the powder and substrate with an angle, the created melt pool is tilted accordingly, as shown by the micrograph in 2.5c. In addition, with increasing deflection, the laser spot deviates from its circularity and deforms to an ellipse, which influences intensity and power distribution.

As the reader is now familiar with the basic concepts and important influencing parameters of the LPBF process, a deeper discussion about process physics and its relation to process parameter selection will be given in the following section.

2.2 Process mapping

Since parts are created in LPBF by consolidating multiple neighboring scan tracks and consecutive layers, a single melt pool can be defined as the basic processing unit. A general P-u process map for single scan lines with different regions, limiting the process window, is shown in Figure 2.6. Single line scans considered inside the process window should ideally have sufficient adherence to the underlying substrate material, no surface irregularities, and no porosity. The process window is limited by the balling boundary, the humping boundary, and the keyhole porosity boundary. Each of those boundaries is attributed to a specific physical phenomenon, which will be described in more detail in the following subsections.

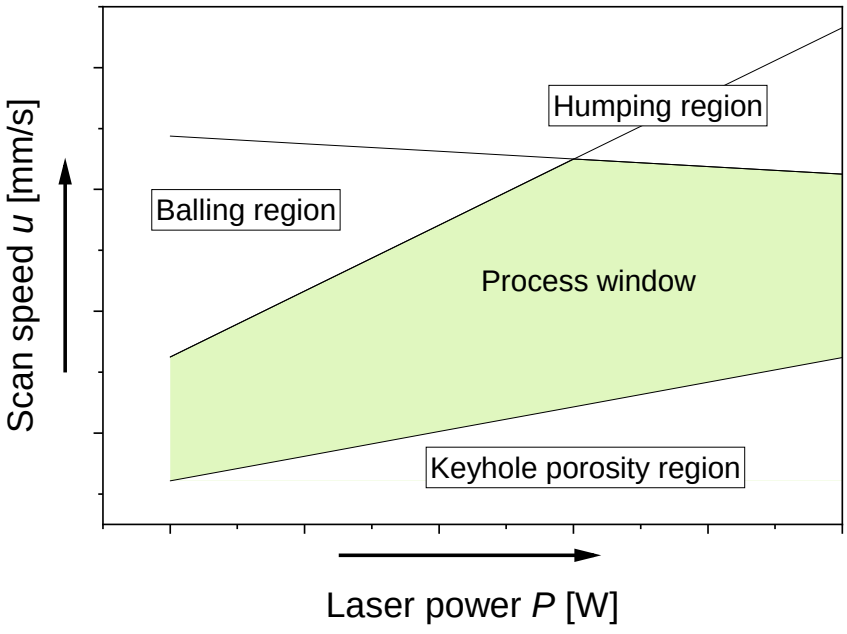

Figure 2.6: Schematic of laser power and scan speed process map with different defect regions

2.2.1 Welding modes

Laser welding conditions are commonly distinguished as conduction mode or keyhole mode welding with distinct process parameter ranges and melt pool characteristics. Figure 2.7 shows micrographs of typical melt pools together with schematic drawings for the two welding modes. In conduction mode, the laser energy is absorbed on the flat metal surface and thermal transport mainly happens by conduction, resulting in a wide and shallow melt pool (Figure 2.7a). Due to the low absorptivity of a flat molten metal surfaces, only a fraction of the laser energy contributes to melting of the material. This results in low process efficiency. In contrast, in keyhole mode welding, the incident laser energy is high enough to enable local evaporation of the material and a cavity, called keyhole, is formed in the melt pool by the resulting recoil pressure. The depression in the melt pool surface leads to a more efficient absorption of the incident laser beam by multiple reflections, which further facilitates the increase in keyhole depth. Therefore, deep and narrow welds can be achieved in keyhole mode welding (Figure 2.7b). [76]

However, keyhole welding is prone to the formation of process defects due to melt pool instabilities as will be discussed within this subsection. Since conduction mode welding can be attributed to the low laser power regime and keyhole welding to the high power regime, the transition between those two modes is typically defined in the welding community as power density threshold of $10^6\,\mathrm{W/cm^2}$ [76]. However, Assuncao et al. [77] showed that the onset of keyholing is not sharp, but that there exists a transition region with the melt pool containing characteristics of both modes. Furthermore, Fabbro et al. [78] considered melt pools with small vapor depressions, not acting as ray traps to the incidence laser beam, as conduction mode weld pools. Although criteria based on the vaporization of material and dimensions of the vapor depression would best represent the physics between the two welding modes, they are not observable post-mortem

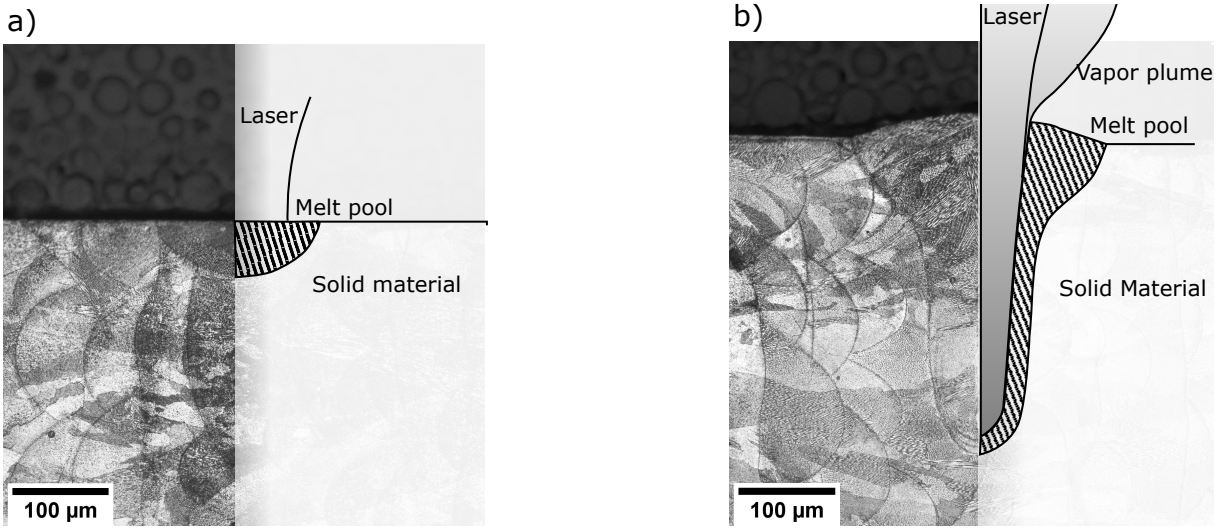

Figure 2.7: Schematics of welding modes with micrographs of corresponding melt pools; a) conduction welding and b) keyhole welding, material is IN718

and expensive experimental techniques such as X-ray or Schlieren imaging[5] have to be applied for observation. Therefore, the two welding modes are often distinguished based on the aspect ratio R of melt pool depth to melt pool width.

$$R = \frac{d}{w} \begin{cases} \leq 0.5, & \text{conduction mode} \\ > 0.5, & \text{keyhole mode} \end{cases} \tag{2.1}$$

A melt pool with depth larger as half its width will be considered to be in keyhole mode [79]. In this thesis, the definition in Equation 2.1 will be used to distinguish between the two welding modes.

While conduction welding mode was suggested to be beneficial in terms of process stability and productivity [51], with typical beam diameters in LPBF ranging from $50\,\mu\mathrm{m}$ to $100\,\mu\mathrm{m}$ and laser power up to $500\,\mathrm{W}$, it can be assumed that a large portion of the processing space is dominated by keyhole mode welding. This has been validated experimentally by Cunningham et al. [80] and Zhao et al. [81], using X-ray imaging of the melt pool. For almost all their parameter combinations, including a wide range of processing speeds, laser power, and beam diameters, a vapor depression was observed to form. Although keyhole mode welding is beneficial in terms of process efficiency, as stated previously, it is also prone to form so called keyhole porosity at certain process parameter combinations. While for modeling purposes the keyhole front wall is often depicted as perfectly smooth, in reality severe distortions can occur due to the complex melt flow and pressure conditions inside the keyhole. The formation of humps in the keyhole front wall can change the absorption condition by shielding the lower part of the keyhole from the beam or redirecting the vapor plume to the rear keyhole wall creating a disturbance [68, 82–86]. Both cases can lead to collapse of the keyhole and formation of porosity. Such a keyhole collapse, with subsequent pore formation, is shown in the X-ray image series in Figure 2.8a. Zhao et al. [81] investigated an extensive parameter space for LPBF with and without powder for keyhole instability in Ti6Al4V. They found a lower threshold power for keyhole porosity creation while with increasing power the transition from unstable to stable keyhole shifted to higher scan speeds. The addition of a $100\,\mu\mathrm{m}$ powder layer only slightly moved the boundary for keyhole porosity onset to higher speeds and a higher threshold power [81]. Similarly, for laser welding, the keyhole was observed to stabilize with increasing welding speed [76, 84]. Therefore, the keyhole porosity boundary limits the process window at low scan speeds and has a positive slope with laser power in Figure 2.6. The increase in stability with increasing speed can be attributed to a decrease of the front keyhole wall angle Θ, as shown in Figure 2.8b [78, 81, 87]. Since the majority of the laser impinges on the front keyhole wall, its tilt significantly affects the efficiency of the reflected laser radiance and the occurrence of multiple reflections. With an increase in tilt angle, corresponding to a decrease in scan speed, the laser is reflected in a downwards direction

[5] Schlieren imaging is a technique to visualize differences in refractive indexes introduced by temperature, pressure or concentration gradients and can thereby be used to observe fluid motion.

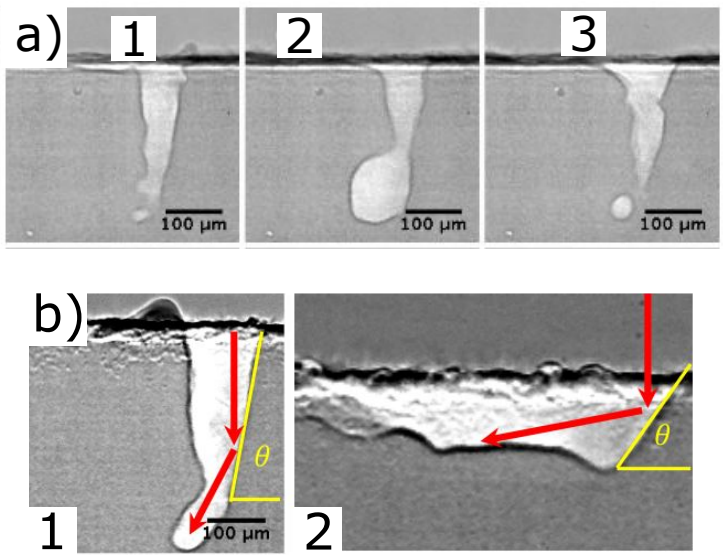

Figure 2.8: X-ray images of Ti6Al4V illustrating the collapse of a keyhole and formation of porosity [87]; a) frame-by-frame series of images (time step of 20 µs) showing collapse of keyhole front and rear wall and formation of a pore (230 W, 400 mm/s) and b) change in keyhole front wall angle with scan speed, 1: 416 W, 800 mm/s and 2: 260 W, 1200 mm/s

to the rear keyhole wall (Figure 2.8b1). This increases the probability for multiple reflections to occur [78]. However, the reflected rays as well as the vapor from the front keyhole wall impinge on the rear wall and could lead to bulging and connection of the rear keyhole wall with the front keyhole wall as depicted in the image series in Figure 2.8a. Due to the decreased tilt angle (Figure 2.8b2), the reflected rays as well as vaporized material impinge on the upper part of the keyhole rear wall and elongate it. Thereby, the probability of the keyhole to collapse is reduced. Cunningham [87] proposed a critical keyhole front wall angle for keyhole porosity formation of 77°. However, the keyhole front wall angle can only be determined with significant experimental effort. Zhao et al. [81] instead propose a threshold based on keyhole depth. However, this critical depth is supposed to vary with scan speed and laser power. A quantitative criteria for the onset of keyhole porosity does not exist up to now, although recent research contributed a lot to the understanding of the phenomenon. Even when processing with stable keyhole parameters, the scan strategy and its settings have to be taken into account to avoid keyhole porosity.

Concerning preheating, the increase of surface temperature reduces the energy input required for keyhole formation. This is of special importance at low scan speeds where the scanning beam can induce a temperature increase in front of the scan path. A transition from a shallow to a deep vapor depression along a scan line was observed by Zhao et al. [81] using X-ray imaging. Furthermore, in LPBF the scanning of neighboring scan lines and layers can cause local variation in preheating temperatures, influencing the melt pool and keyhole dimensions [67, 87]. Similarly, locations close to the start and end point of hatches or turns of the laser, where the speed is slowed down at constant power if no Skywriting is applied, can cause a steep increase in keyhole depth. The susceptibility for pore formation is thus increased at these locations as was observed

in experiments [68] and simulations [69]. In both cases, pore formation was avoided by the adaption of beam power to local scan speed. While the parameters for those power adaption strategies have to be calculated for each material and parameter setting, a less complex way to mitigate these defects is to apply Skywriting as explained in Section 2.1.2.2. Nevertheless, even with Skywriting, so called end-of-track defects can occur for keyhole mode welding. When the laser beam is abruptly turned off at the end of a hatch, the sudden lack of the vapor jet to keep the keyhole open leads to a collapse due to surface tension forces. A cavity can be formed as the top part collapses and solidifies before filling the keyhole bottom [88]. Even if no pore is created, incomplete back filling of the keyhole cavity with material leads to a depression in the solidified surface, which is prone to defect formation in the next layer. End-of-track defects can be reduced by applying a power ramp down at the end of a hatch, thus allowing the molten material to fill the keyhole cavity. [69]

2.2.2 Balling

The low power high speed corner of the process window is limited by the so called balling defect, which is shown in comparison with a stable scan track in Figure 2.9. Balling occurs when the energy of the laser beam is sufficient to melt the powder, but is insufficient to deeply remelt the underlying substrate material making the melt pool prone to the Plateau-Rayleigh instability [89–94]. In the most severe case of balling, molten powder particles cannot connect to the underlying material and instead coalesce with each other to decrease their free surface energy. In case of a moving laser beam over a loose powder bed, the melt pool can be viewed as a free cylinder of molten metal. According to the Plateau-Rayleigh instability criterion, it will break into smaller droplets if its length becomes larger than its circumference [94, 95]. In LPBF, most scan tracks are not free floating cylinders, as they are scanned upon a substrate

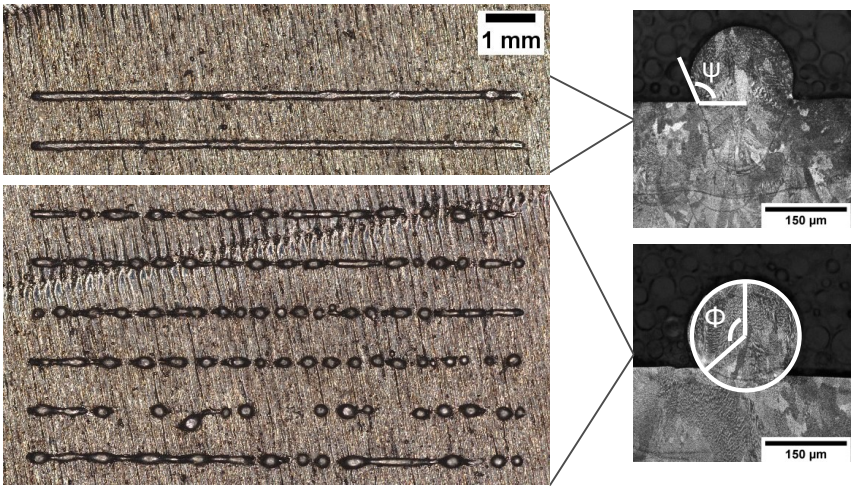

Figure 2.9: Example macrographs of stable single scan tracks (top) and scan tracks with balling defect (bottom); micrographs on the right side show corresponding melt pool cross sections; indicated are the contact width angle Φ and contact angle ψ

or already solidified material. To account for this, Yadroitsev et al. [92] proposed a stability criterion against surface perturbations in a cylindrical segment partially connected to a substrate. Besides length and circumference of the cylinder, its stability is then also related to the contact width with the substrate (defined by the contact width angle Φ indicated in Figure 2.9). For $\Phi < \pi/2$ the melt pool is always stable indicating that a sufficient connection to the substrate will avoid the balling defect. Scan track stability can also be related to the contact angle ψ between melt pool and substrate surface (Figure 2.9) as a measure of wettability between the liquid and solid material. For lower ψ the molten material prefers wetting and spreads over the surface. Wetting characteristics can change greatly in dependence of surface chemistry as experiments by Li et al. [96] had shown. Due to the formation of surface oxides, an increase in oxygen content within the process gas led to a decrease in wettability of the molten metal [96]. The probability of balling to occur can be decreased by increasing the energy input to enable sufficient connection between the newly formed scan track and the underlying layer, so that the criteria of $\Phi < \pi/2$ is met [96, 97]. Increasing scan speed, in contrast, will enhance the balling probability by increasing the melt pool length, while slightly decreasing melt pool width, thus decreasing the diameter to length ratio and the contact area to the substrate [90, 96, 97]. This explains the positive slope of the balling boundary with increasing power in Figure 2.6. Additionally, as observed by Yadroitsev et al. [92], the balling onset velocity decreases with increasing powder layer thickness since a higher layer thickness needs higher energy input to fully melt the powder and connect the material sufficiently to the underlying substrate. The balling phenomenon was only discussed in relation to single scan lines, and one should keep in mind that multiple consecutive scan tracks might be stabilized by their neighboring scan track, as they reduce the free surface area. Thereby, the balling boundary is shifted to higher scan speeds. Nevertheless, balling might still be present even for multiple neighboring scan lines under severe process conditions as observed by Rombouts et al. [98]. However, in case of process maps for three dimensional parts, one does not find a balling boundary, but a lack-of-fusion boundary. Lack-of-fusion defects occur when there is insufficient overlap between neighboring scan tracks. A rational connection can be given between the balling and lack-of-fusion boundaries: Since tracks with surface instabilities will have significant variability in width and height of a melt pool, they will be prone to lack-of-fusion defects between neighboring scan tracks [89]. Beside balling, another phenomenon in regard with melt pool instability is the so called humping, which will be discussed in the following subsection.

2.2.3 Humping

Humping is a well known phenomenon in arc, electron, as well as laser welding when welding at high speeds in keyhole mode[79, 99–104] and refers to the formation of periodic agglomerates of molten material (humps) at the melt pool surface, as shown in Figure 2.10a. Typically, undercuts are observed at the melt pool sides, while material is accumulated at the melt track

center. Although, humping without undercuts was also observed experimentally [102]. While in the laser welding literature humps are most often observed to form periodically [101, 102, 104], Seiler et al. [105] state that in microwelding humps form stochastically. Despite the enormous amount of research on this phenomenon, a physically sound and conclusive explanation is still lacking [79, 106]. Therefore, general characteristics and experimental results of the humping phenomenon will be discussed in the following. Patschger et al. [106] refer to three different view points in the explanation of humping which are fluid dynamic, surface tension driven, and geometric aspects. The fluid dynamic approach attributes humping to the formation of a high velocity stream behind the keyhole which piles up at the end of the melt pool [108, 109] (see Figure 2.10b). As the keyhole constricts the volume for molten material to pass through, high flow velocities are achieved within the melt flowing around it and a high velocity jet forms in the center region of the melt pool behind the keyhole (corresponding to the 'strip liquid jet' in Figure 2.10b). This high velocity jet can lead to the typical undercuts at the melt pool sides and a pile up of material, a hump, at the melt pool end [108]. In addition to melt pool dynamics, Fabbro et al. [109] consider the Plateau-Rayleigh instability to support hump formation in the central high velocity jet region. Its unfavorable dimensions, long and thin, make it prone to surface tension driven instabilities. Actually, the Plateau-Rayleigh instability was mainly considered responsible for humping by many research groups [100–102]. However, the description solemnly by this phenomenon, neglecting melt flow dynamics, does not agree with hump formation observed by high speed imaging, and therefore seems too simplistic [109]. Finally, Berger et al. [84] add geometrical constraints due to solidification of the molten material to the fluid dynamic and surface tension considerations. In their model, solidification, starting from the melt pool boundaries, additionally constricts the melt pool cross section, and thus increases the fluid velocity. Additionally, the solidification front creates a ramp for the central

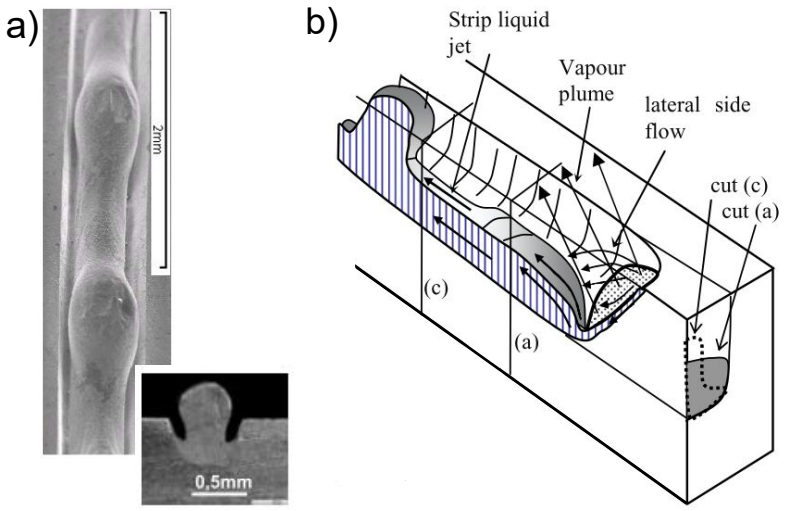

Figure 2.10: Humping phenomenon; a) example of humping defect of a laser weld with insert showing melt pool cross section and b) schematic of melt pool morphology and dynamics to explain humping; reproduced from Fabbro et al. [107], with permission of the Laser Institute of America

melt jet to accumulate and form a hump. Thus, despite its relation to the Plateau-Rayleigh instability, additional mechanisms contribute to the humping phenomenon and distinguish it from the balling phenomenon.

Since the creation of a high velocity jet within the melt pool behind the keyhole plays a crucial role in hump formation, it occurs at high scan velocities in connection with keyhole mode welding. The critical velocity for the onset of humping u_{Hump} depends on material and process parameters such as laser beam size and power [101, 106, 110]. In laser welding [101] and micro laser welding experiments [106], u_{Hump} was observed to decrease with increasing laser power. Therefore, the humping limit is plotted with a negative slope in Figure 2.6. When the laser beam diameter is increased, u_{Hump} was found to increase due to the expansion of the keyhole size and corresponding decrease in melt pool velocities [106]. Concerning material, u_{Hump} is affected by the temperature difference between evaporation and melting as well as by thermal diffusivity, influencing the size of the molten material surrounding the keyhole [106]. Furthermore, a high liquid viscosity decreases melt velocities [106, 110]. Additionally, a low surface tension seems beneficial in terms of hump formation [106], although contradicting results have been observed by Tang et al. [110]. Besides surface tension itself, its gradient with temperature can contribute to hump formation as well. A positive surface tension gradient increases the likelihood for hump formation, as it supports the build up of material at the melt pool center line [110].

2.2.4 Marangoni convection

Although the Marangoni convection is not directly linked to one of the boundaries in the process map in Figure 2.6, it influences the melt pool morphology and affects probability for defect formation. The Marangoni convection is a fluid flow induced by the temperature dependence of surface tension [35, 41, 79, 113]. Two different melt pool flow profiles can be distinguished depending on the sign of the surface tension gradient as depicted in Figure 2.11. Molten metals usually have a negative surface tension gradient [35], meaning that hot material from the molten pool near the laser center will flow to the colder boundary regions of the melt pool as shown schematically in Figure 2.11a. As the hot material is transported to the colder region, the melt pool width and length are enlarged, while melt pool depth decreases. In contrast, for a positive surface tension gradient, which applies to molten metals with surface active elements such as sulfur or oxygen [79], the melt flows from the colder boundary regions to the melt center. Thereby, melt pool width and length are narrowed, while melt depth is increased (Figure 2.11b). Since the Marangoni convection can influence the shape of the melt pool cross section, a contribution to the previously discussed balling and humping phenomena is expected. For example, a negative surface temperature gradient could have a positive effect on balling as well as humping by increasing the wettability with the substrate and increasing melt pool width, thus decreasing flow velocities in the melt pool [110, 114]. The influence of Marangoni convection on melt pool morphology is material and process parameter dependent. While disregarding melt

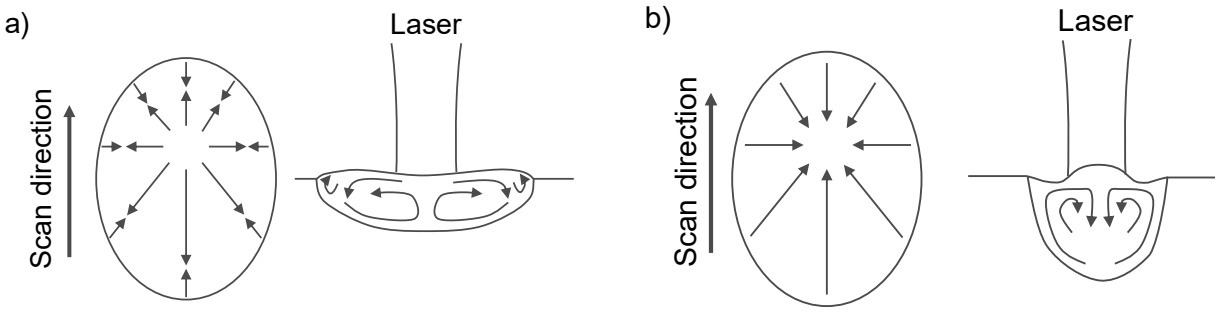

Figure 2.11: Schematic of the Marangoni convection in case of a) negative surface tension gradient with temperature and b) positive surface tension gradient with temperature, redrawn after [79]

pool convection might not lead to large errors for high thermal diffusivity materials, such as Al-alloys, as heat is mainly distributed by heat diffusion, it can introduce large errors in estimation of melt pool dimensions for alloys with lower thermal diffusivity, such as steels [79, 115]. In keyhole mode welding, additional flow contributions are introduced by the recoil pressure of the keyhole as well as vapor-melt interactions. While at low to medium welding speeds the Marangoni convection dominates melt pool dynamics [113, 115, 116], it is assumed by Fuhrich et al. [113] that keyhole flows might be more important at high speeds.

2.2.5 Energy input definitions

Since empirical testing of a wide combination of laser power and scan speed to determine process maps is time and cost intensive, various energy input formulas combining different process parameters are used in literature. Instead of single parameter ranges, the process window and melt pool morphology is then related to a specific energy input regime. The most common of such energy input formulations are linear energy density LED [117–120], areal energy density AED [121], and volume energy density VED [51, 122, 123].

$$LED = \frac{P}{u} \tag{2.2}$$

$$AED = \frac{P}{ua} \tag{2.3}$$

$$VED = \frac{P}{ual_t} \tag{2.4}$$

For multitrack experiments, energy input formulations AED and VED are often defined with hatch distance h_d instead of beam diameter a [89, 124, 125]. Zavala-Arredondo et al. [125] compared the usability of the three energy input definitions for density optimization of AlSi10Mg samples fabricated with two different layer thicknesses and a variety of laser power and speed combinations. They found LED to better represent defect formation compared to VED and AED. However, they suggest that beam diameter should also be included in the energy input

and propose their own definition of energy input by specific point energy and power factor to compare results from machines with different laser spot diameters. An extension of VED including the ratio of mean powder particle size and beam diameter was proposed by Oliveira et al. [126] to compare research results of the same alloy obtained with different powder size distributions.

As discussed in the previous paragraphs, defect formation is closely related to melt pool morphology, and therefore numerous studies investigated the relation of process parameters and melt pool dimensions [15, 51, 89, 117, 119–122, 127]. While a general trend of increasing melt pool dimensions width and depth with increasing energy input is indisputable, the validity of the introduced energy input formulations to scale melt pool dimensions for different process parameter combinations is not clear from literature. While, for example, Campanelli et al. [121] found melt pool dimensions width and depth to scale well with AED, Keshavarzkermani et al. [120] observed a dependence of melt pool dimensions on applied process parameter combinations at constant LED. This inconsistency was attributed to a greater influence of laser power compared to scan speed, resulting in the wrong scaling with the LED definition of Equation 2.2. Therefore, Bertoli et al. [122] proposed a scaling of $1/\sqrt{u}$ instead of $1/u$ for melt pool depth. However, melt pool depth and width were observed to fit equally well with $1/\sqrt{u}$ as well as $1/u$ by Metelkova et al. [51]. Although, they noticed a discontinuity in the scaling of melt pool depth with VED in dependence of the applied scan speed range. Furthermore, Guo et al. [128] showed that similar AED could lead to different melt pool dimensions and melting modes, which was attributed to the difference in absorptivity and heat loss of the compared process parameters. This shows that a deep understanding of the influence of process parameter ranges on different physical mechanisms and their interaction is necessary to evaluate experimental results derived under varying process conditions.

Besides inconsistencies in the observed scaling relations, another drawback of using energy input formulations, solemnly based on process parameters, is the lack of comparability for different materials. While for similar alloys comparable ranges of energy input might be valid as a starting point for process optimization, the range of energy input resulting in low defect formation has to be experimentally investigated anew for alloys with different thermophysical properties. To overcome this drawback, Fabbro et al. [103] introduce a scaling parameter that depends on thermal properties of the investigated alloy within their depth to energy input relation. In a similar approach, dimensionless scaling laws can be developed to relate physical phenomena independent of actual dimensional values as will be discussed in the following section.

2.3 Dimensionless numbers

The concept of dimensionless numbers is often used in the field of engineering to describe similarity between physical phenomena independent of scale [129, 130]. The most famous dimensionless number is probably the Reynolds number Re

$$Re = \frac{UL}{\gamma} \tag{2.5}$$

characterizing the flow of a liquid with velocity U and kinematic viscosity γ along a characteristic length L as laminar (low Re) or turbulent (high Re) [131]. Analyzing the fundamental dimensions of variables of a specific physical problem, one can arrange those variables to form groups of dimensionless numbers. The maximum number of such dimensionless groups that can be formed is given by the Buckingham-Pi-Theorem [132]: Any problem with n independent variables consisting of q independent fundamental units can be represented by $i \leq n - q$ dimensionless numbers. Grouping of variables to dimensionless numbers is beneficial in terms of experimental effort, as it reduces the number of experiments. Instead of each single variable, only the dimensionless number has to be varied and the experimentally most convenient variable can be chosen to do so. [129] In addition, it enables deductions from experiments on small scale models, which is especially useful in aerospace or nautical applications [130].

An overview of various dimensionless numbers that can be used to study LPBF was given by VanElsen et al. [133]. Some of those dimensionless numbers will be introduced in the following and the interested reader is referred to [133] for the complete list. The Peclet number Pe, determining the surface temperature [79], is an important dimensionless number in laser welding and is often included in estimations of melt pool dimensions for conduction [134, 135] as well as keyhole mode welding [115, 136, 137]. It defines a ratio of heat distribution by conduction to heat convection and corresponds to the inverse of the Fourier number Fo.

$$Pe = \frac{UL}{D} = \frac{ua}{D} = \frac{1}{Fo} \tag{2.6}$$

As common in this community scan speed u is used as characteristic velocity U and beam diameter a as characteristic length L. In this form, it characterizes the ratio between heat distributed by the movement of the laser to heat distributed by conduction. It can also be defined based on the velocity of the liquid metal within the melt pool u_{MP} and melt pool length l as characteristic length [138].

$$Pe_{MP} = \frac{u_{MP} l}{D} \tag{2.7}$$

In this case, it relates heat distributed by convective flows within the melt pool to heat distributed by conduction. In general, it characterizes the heat distribution mechanism, and thus the shape of the temperature field and the melt pool dimensions [26]. At high Pe numbers, heat is mainly

distributed by convection, resulting in a shallow and long melt pool. In contrast, for small Pe numbers, conduction dominates, leading to near hemispherical melt pools. Due to its influence on melt pool geometry, it in turn affects cooling rates and thermal strains [138].

Another dimensionless number often discussed in connection with melt pool dimensions in laser welding [113, 135] and LPBF [38, 138] is the Marangoni number Ma, which characterizes the strength and direction of the Marangoni convection. It is defined as

$$Ma = -\frac{\delta\sigma}{\delta T}\frac{\Delta T_{max} L}{\eta D} \tag{2.8}$$

with surface tension gradient $\delta\sigma/\delta T$, temperature difference between maximum temperature and solidus temperature ΔT_{max}, and dynamic viscosity η. Melt pool width is often used as characteristic length L. As discussed in Subsection 2.2.4, the Marangoni convection influences melt pool shape and melt pool instabilities.

Additionally, melt pool dynamics can be characterized by the Weber We and Ohnesorge Oh number, as well as the aforementioned Reynolds Re number (Equation 2.5). Corresponding definitions are given in Equation 2.9 to Equation 2.11 with density ρ and surface tension σ. For Re in this context, a is set as the characteristic length L, u as characteristic velocity U, and η/ρ is substituted for γ, resulting in the definition of Equation 2.11.

$$We = \frac{u^2 \rho a}{\sigma} = Re^2 Oh^2 \tag{2.9}$$

$$Oh = \frac{\eta}{\sqrt{\rho a \sigma}} = \frac{\sqrt{We}}{Re} \tag{2.10}$$

$$Re = \frac{u \rho a}{\eta} = \frac{\sqrt{We}}{Oh} \tag{2.11}$$

While Oh is the ratio of viscous to surface tension forces, We is the ratio of inertial forces to surface tension forces, and Re the ratio of inertial forces to viscous forces. Although their influence was acknowledged by VanElsen et al. [133], no quantitative or qualitative statements on their influence on melt pool instabilities in LPBF was given.

Concerning energy input, a variety of different dimensionless parameters were suggested in literature [26, 28, 29, 133, 138]. Mukherjee et al. [138] proposed a non-dimensional heat input Q^* as ratio of P/u to a predefined reference P_R/u_R. Although being a dimensional number, this ratio does not include thermophysical material properties and limits its applicability when quantitatively comparing results for different materials. An alternative dimensionless energy input definition including material properties was proposed by Wang and Liu [29] as the multi track efficiency η_m, relating laser energy input to energy necessary to melt the material.

$$\eta_m = \frac{AP}{u h_d l_t \rho (c_p \Delta T + h_f)} \tag{2.12}$$

With absorptivity A, temperature difference from initial to solidus temperature ΔT , and latent heat for melting h_f. The term $(c_p \Delta T + h_f)$ describes the total amount of energy needed for melting per mass of material and will be denoted h_s in the following. This non-dimensional melt efficiency is a dimensionless version of the VED in Equation 2.4. In addition, they proposed a multi track efficiency for vaporization η_v,where h_s was substituted by the energy needed for vaporization h_v to estimate the formation of keyhole porosity (Section 2.2.1). Using those two dimensionless numbers, they found a process window obtaining the lowest porosity for three different alloys with conditions $\eta_m > 5$ and $\eta_v < 0.838$. While incorporating many important process parameters, those dimensionless efficiencies neglect the influence of laser beam diameter on melt pool dimensions and defect formation. Additionally including laser beam size, Fourier number, and melt pool dimensions besides thermophysical material properties and process parameters, Mukherjee et al. [140] propose the lack-of-fusion number L_F to predict sample porosity. However, melt pool dimensions need to be known to calculate L_F. Moreover, as implicated by the name, it is only applicable to predict lack-of-fusion defects.

Since melt pool dimensions depend on energy input, as discussed in Subsection 2.2.5, a variety of investigations exist relating melt pool morphology to some non dimensional numbers. Großmann et al. [25] found a linear relationship between melt pool width represented in a form of Peclet number and dimensionless specific power for six different alloys. In a follow up work, they introduced a modified version of the specific power including a factor for the beam size effect [141]. Besides introducing η_m and η_v for process window estimations, Wang et al. [29] could correlate melt pool width and depth for two alloys with the so called track size number (a ratio of maximum surface temperature to temperature difference from initial to vaporization temperature). While this dimensionless track size parameter was developed based only on heat conduction and a laser beam impinging on a flat surface, Fabbro et al. [142] proposed a dimensionless number derived from a cylindrical keyhole model to scale with keyhole depth. Applying the Buckingham-Pi-Theorem, they could validate their proposed scaling relation - that the aspect ratio of keyhole depth to beam diameter is a function of Peclet number and a dimensionless energy input ratio [24]. Their proposed scaling holds for laser welding parameters in the kW range as well as for typical LPBF process settings. Recently, an increased amount of publications have used the dimensionless enthalpy equation, or some derived form, as energy input parameter in LPBF [26–28, 56, 68]. Similar to the melting efficiency η_m, the dimensionless enthalpy H^* is a ratio of laser energy input to energy required for melting. However, as it was originally introduced by Hann et al. [143] for laser welding, the volume for energy input is formulated in a different way to Equation 2.12 resulting in

$$H^* = \frac{h_{LEV}}{h_s} = \frac{4AP}{\pi \rho h_s \sqrt{a^3 D u}} \tag{2.13}$$

with the energy input volume defined by the laser beam area and the heat diffusion length. A graphical illustration of the derivation of the dimensionless enthalpy is shown in Figure 2.12a.

The relationship between dimensionless melt pool depth d^*, which is melt pool depth d divided by beam diameter a, and the dimensionless enthalpy H^*, observed by Hann et al. [143] for different alloys and process parameters, is shown in Figure 2.12b. Despite its origin in laser welding, the dimensionless enthalpy was found useful for determining melt pool depth and conduction to keyhole mode transition in LPBF [51, 56, 68]. A guideline on how to apply the dimensionless enthalpy to translate optimum process parameters for different materials was given by Ghasemi-Tabasi et al. [30]. Besides melt pool depth, keyhole depth was also observed to scale nicely with H^* for different alloys [28]. In addition, melt pool depth was scaled with an adapted version of H^* by Ye et al. [27], comparing single scan track dimensions for three different alloys processed under varying scan speeds, laser power, and beam diameters. In their adapted equation, they multiplied H^* with a normalized diffusion length L_d^* which is no other parameter than $1/\sqrt{Pe}$. Although a good correlation was already achieved using constant

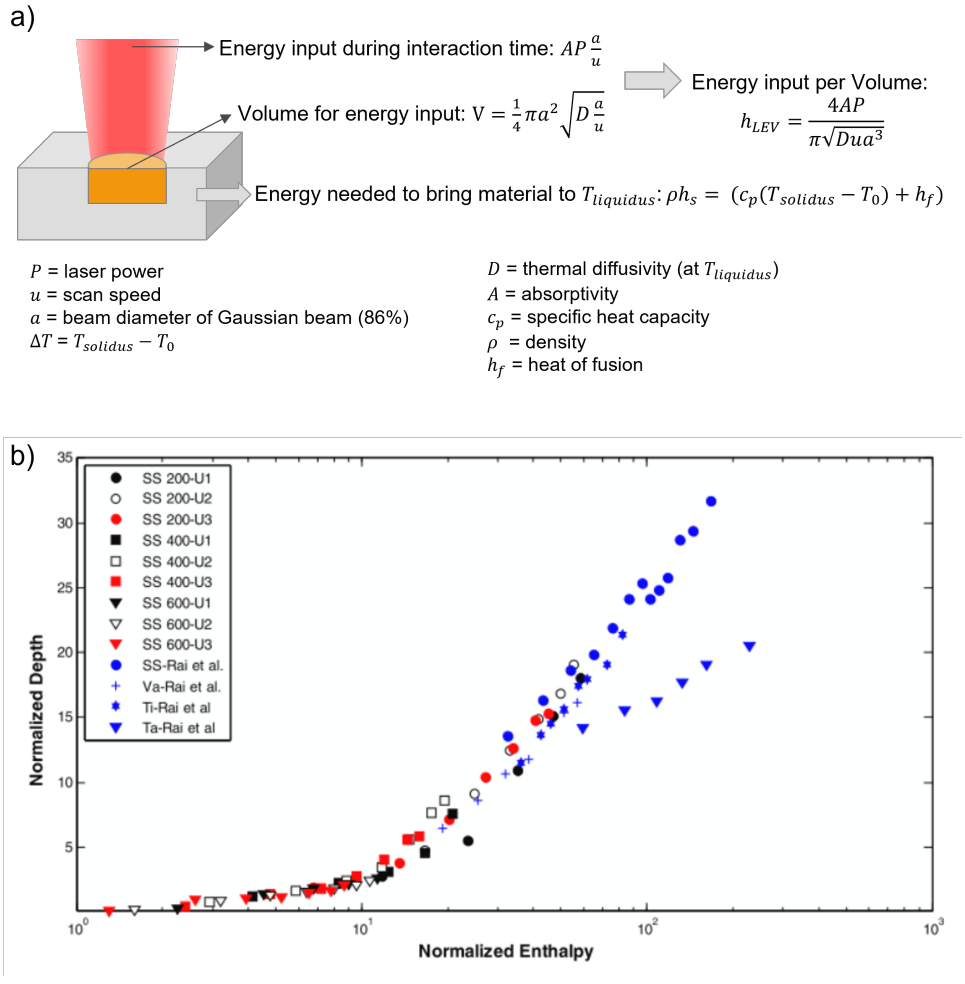

Figure 2.12: Dimensionless enthalpy; a) schematic drawing of derivation and b) results from Hann et al. [143] (©IOP Publishing. Reproduced with permission. All rights reserved.), scaling dimensionless melt pool depth with the dimensionless enthalpy for laser welding of different materials and process parameters

absorptivity for the enthalpy calculations, they could improve their fit by substituting A with an absorption function $A = f(H^* L_d^*)$ that included the variation of absorptivity depending on keyhole geometry as observed by calorimetric measurements. A similar adapted form of H^* including L_d^* was used by Gan et al. [28] in combination with η_m to predict porosity within samples. In accordance with those previous studies, Rubenchik et al. [26] derived that melt pool dimensions should scale with the dimensionless enthalpy and the Peclet number based on a purely thermal conduction model. They proposed a difference in the scaling relation with melt pool depth depending on Peclet number. However, no experimental validation of such a transition in scaling relation was given in the work of Rubenchick et al. [26] nor in any of the aforementioned investigations.

From the presented literature, it can be seen that steps are already taken to introduce dimensionless scaling laws in LPBF with increasing interest in recent years in verifying their use for process control as well as prediction of melt pool dimensions. However, constraints on their applicability in terms of process range and thermophysical material properties have not been readily discussed in literature. Therefore, in this work, the usability and limitations of the dimensionless enthalpy H^* to characterize melt pool dimensions and define a process window for different materials are investigated in a wide field of process parameters.

3 Materials and methods

3.1 Investigated materials

3.1.1 Powder feedstock

The investigated samples were built from standard commercially available gas atomized EOS powders of the alloys IN718 (EN 2.4668), MS1 (EN 1.2709), 316L (EN 1.4404), Ti64 (EN 3.7164), and AlSi10Mg (EN AC-43000). The iron-based alloys MS1 and 316L, as well as the nickel-based superalloy IN718, were selected due to their comparable thermophysical properties and good weldability (see Table 3.2). Furthermore, Ti64 was chosen since it obtains a lower density, higher solidus and liquidus temperature, as well as lower surface tension and viscosity at similar thermal conductivity compared to the aforementioned alloys. AlSi10Mg is included in the investigations, as it has significantly different thermophysical properties than the other alloys. The compositions of all alloys are shown in Table 3.1 and the particle size distributions for the powders are presented in Figure 3.1.

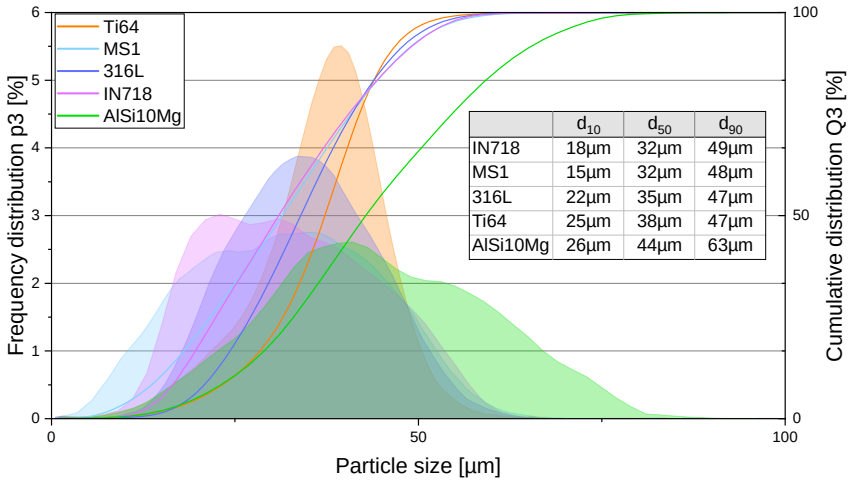

Figure 3.1: Particle size distributions of powder feedstock

Table 3.1: Composition of powders in wt%

Element	Al	Co	Cr	Cu	Fe	Mg	Mn	Mo	Nb	Ni	Si	Ti	V	Zn	C	N	O	P/S	Others
IN178	0.20 - 0.80	- 1.00	17.00 - 21.00	- 0.30	Bal		- 0.35	2.80 - 3.30	4.75 - 5.50	50.00 - 55.00	- 0.35	0.65 - 1.15			- 0.08			- 0.015	- 0.05
MS1	0.05 - 0.15	8.50 - 9.50	- 0.50	- 0.50	Bal		- 0.10	4.50 - 5.20		17.00 - 19.00	- 0.10	0.60 - 0.80			- 0.03		- 0.01	- 0.01	
316L			17.00 - 19.00		Bal			2.25 - 3.00		13.00 - 15.00					- 0.03	- 0.10			
Ti64	5.50 - 6.75				- 0.3							Bal	3.50 - 4.50		- 0.08	- 0.05	- 0.2		- 0.1
AlSi10Mg	Bal			- 0.05	- 0.55	0.25 - 0.45	- 0.45			- 0.05	9.0 - 11.0	- 0.15		- 0.1					-0.05

3.1.2 Thermophysical properties

To calculate dimensionless variables, thermophysical properties of the investigated alloys have to be known. An overview of the thermophysical properties for the investigated alloys used in this work is given in Table 3.2. Wherever available, data has been taken from the literature. Due to the lack of data for thermophysical properties up to the liquidus temperature for the alloys AlSi10Mg, 316L, and MS1, thermophysical properties were calculated with the software JMatPro v10 [144]. Calculations in JMatPro were done with the average composition of each element for the respective alloy according to Table 3.1 and a temperature range from room temperature RT up to $400\,\mathrm{K}$ above liquidus temperature in steps of $10\,\mathrm{K}$. Thermal diffusivity D is calculated based on Equation 3.1 with thermal conductivity k, density ρ, and specific heat capacity c_p.

$$D = \frac{k}{\rho c_p} \tag{3.1}$$

For surface tension and viscosity of all investigated alloys, except Ti64, the average value from liquidus temperature to $400\,\mathrm{K}$ above liquidus from the respective JMatPro calculations has been taken as reference. Surface tension and viscosity of Ti64 were taken from Mohr et al. [145]. Absorptivity was estimated as rounded values from the minimal absorptivities measured by Ye et al. [27] for IN718, 316L, MS1, and Ti64. For AlSi10Mg, absorptivities for flat surfaces proposed in literature range from 0.01 [28] and 0.05 [125] to 0.15 [146]. Therefore, an absorptivity of 0.1 is choose as an approximation.

Table 3.2: Thermophysical properties of investigated alloys used to calculate dimensionless numbers; absorptivity taken from [27] for IN718, MS1, 316L, and Ti64, and an average between [125] and [146] for absorptivity of AlSi10Mg

	Density ρ	Melting range	Enthalpy h_s	Thermal conductivity k_l	Thermal diffusivity D_l	Surface tension σ	Dynamic viscosity η	Absorptivity A
	RT [kg/m^3]	[K]	10^3 [J/kg]	[W/(m K)]	10^{-6} [m^2/s]	[mN/m]	[mPa s]	[-]
IN718 [144, 147]	8260	1528 - 1610	968	26.8	4.5445	1709	6.3	0.3
MS1 [144]	8209	1659 - 1714	1121	31.5	5.7697	1704	5.6	0.3
316L [144]	7865	1653 - 1706	1143	30.3	5.4662	1716	6.0	0.3
Ti64 [145, 148, 149]	4420	1878 - 1928	1563	29.2	7.8416	1492	4.0	0.3
AlSi10Mg [144]	2667	826 - 868	1062	80.0	29.0974	755	1.2	0.1

3.2 Sample processing via LPBF

3.2.1 Substrate preparation

To reduce post processing effort and enable a reproducible surface quality, single line scans and single layer hatch packages produced in this work were build on substrate plates. The substrate plates with print dimensions $40\,\mathrm{mm} \times 43\,\mathrm{mm} \times 6\,\mathrm{mm}$ were additively manufactured on an EOS M290 systems using the same powder feedstock as for the respective experiments. Figure 3.2a shows the arrangement of the substrate plates within the process chamber in the

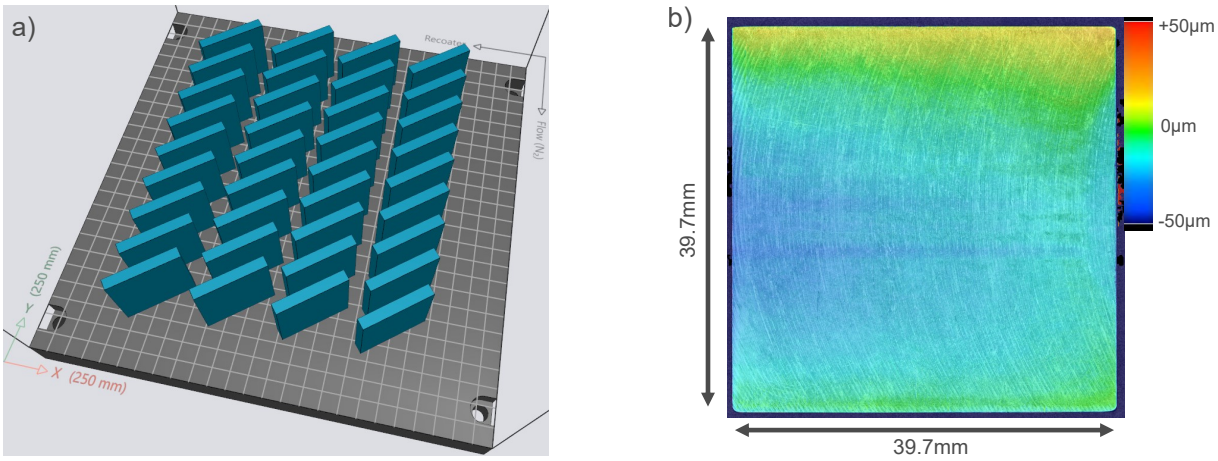

Figure 3.2: Preparation of substrate plates; a) screen shot of print job layout and b) surface topography image of cut and milled substrate plate

build preparation software. The substrates were built with standard EOS InFill parameters for each alloy without any contour scans or Up- and DownSkins. The time homogenization feature (explained in Section 2.1.2.2) was enabled to avoid overheating of short scan tracks at corners. To reduce deformation of the substrates upon cutting, a stress relief heat treatment of the whole build plate was conducted after processing for all alloys except IN718. The respective heat treatment procedures are listed in Table 3.3. In addition to reduced distortion, the heat treatment also contributed to enhanced contrast between the substrate material and the single scan tracks within metallographic cross sections. After cutting from the base plate, the substrates were milled to final dimensions of about $39.7\,\mathrm{mm} \times 39.7\,\mathrm{mm} \times 5\,\mathrm{mm}$. Despite careful milling, in-plane distortions throughout the substrate plates could not be completely avoided. To quantify the distortion, each substrate plate was measured with a Keyence VR3200 3D surface profilometer (see Section 3.3.3) with the measuring stage as reference plane. A surface topology image of a final substrate plate is shown in Figure 3.2b. The substrates for IN718, 316L, MS1, and AlSi10Mg used for this work had a maximum in-plane deviation of $77\,\mu\mathrm{m}$, meaning that, in the worst case, the powder layer applied upon the substrate would vary by this value. The Ti64 substrate plates generally showed a higher in plane variability due to difficulties in machining with a maximum deviation of $108\,\mu\mathrm{m}$. Taking into account the relation between effective and nominal powder layer thickness measured for IN718 and Equation 4.10, a change in powder layer thickness of $100\,\mu\mathrm{m}$ would correspond to a decrease in melt pool depth by $40\,\mu\mathrm{m}$. Since melt pool depths of up to $485\,\mu\mathrm{m}$ had been achieved with the investigated parameter combinations, a possible error introduced by the insecurity of applied powder layer is not expected to strongly effect the overall relation of dimensionless number and dimensionless melt pool depth. The actual error within the applied powder layer thickness is expected to be even lower as substrate plates were leveled again inside the process chamber in reference to the recoater blade.

Table 3.3: Stress relief heat treatment procedures

Material	Heat treatment temperature and time
MS1	940 °C for 2 h
316L	1065 °C for 2.5 h
Ti64	1020 °C for 2 h
AlSi10Mg	530 °C for 0.5 h

3.2.2 Single scan track experiments

Single scan tracks were built with an EOS M290 LPBF system featuring a 400 W Yb fiber laser with a wavelength of 1070 nm operated in continuous wave mode. The laser has a Gaussian beam profile with nominal diameter of $80 \pm 4\,\mu m$. Prior to experiments, actual laser beam sizes were measured using a Primes FocusMonitor FMW+ and the beam diameters were calculated based on the 86.5% power aperture method [150]. Measurements were done at 40 W and 200 W and the average of those measurements was taken as the laser beam diameter. If measurements could not be done or data was unavailable the nominal diameter was assumed as reference. All samples were built under Argon atmosphere with residual oxygen content of maximum 0.17% and a base plate temperature of 80 °C, except for AlSi10Mg experiments, where base plate heating was 35 °C. A customized built plate was manufactured with frames in specific locations to hold the substrate plates described in the previous section (Figure 3.3a). To avoid any influence of laser deflection across the build plane, all samples were built in the central location of the holder, ensuring a near orthogonal impact of the laser beam on the powder surface. Prior to inserting the substrates into the holder, they were roughened with 320 grit SiC paper to avoid powder slipping over the milled surface. The substrate was then leveled parallel to the recoater blade

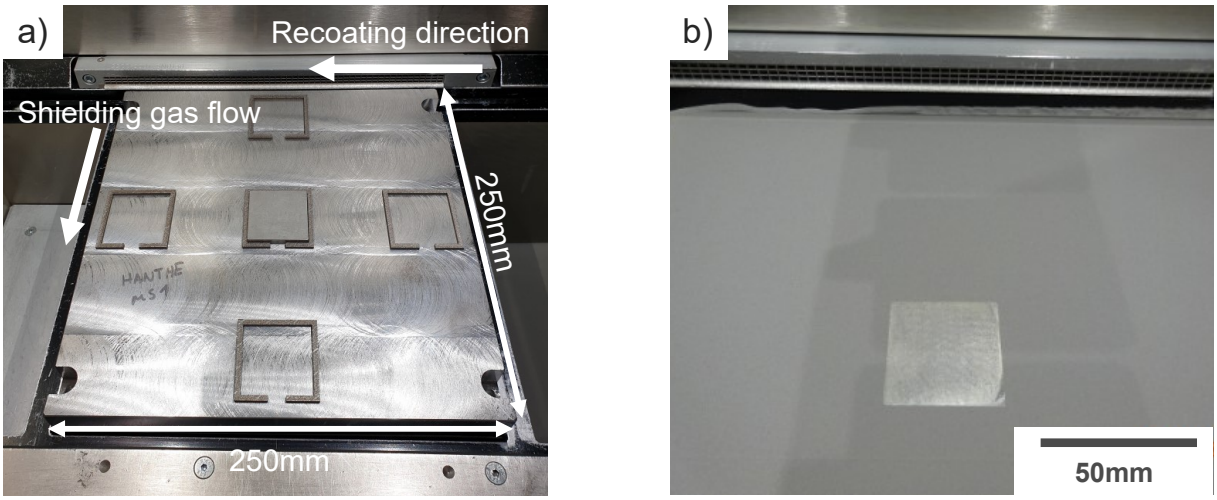

Figure 3.3: Photographs of the experimental setup for single scan tracks and single layer builds; a) substrate holder with substrate in EOS M290 prior to powder addition and b) after application of 40 µm powder layer

and the build platform height was increased until the recoater blade scratched the substrate plate surface. This height was taken as level zero and the build platform was subsequently lowered first by $40\,\mu m$ (Figure 3.3b) and then in $50\,\mu m$ steps up to $190\,\mu m$ total applied powder layer thickness. A powder layer thickness of $190\,\mu m$ was chosen as this value was found in preliminary experiments to correspond to the EPLT for the $40\,\mu m$ standard processes of IN718 and MS1 (Appendix A.1). In addition, one build job for AlSi10Mg was done with applied powder layer thickness of $100\,\mu m$, as this corresponds to the EPLT of the $30\,\mu m$ standard process (Appendix A.1). Two hatches were scanned for each set of processing parameters to ensure repeatability. Scan tracks were set $1\,mm$ apart to reduce the influence of heat input from neighboring tracks (Figure 3.4a). The scanning order was set against the shielding gas flow to avoid interactions with debris from previously scanned tracks. The scan direction was set orthogonal to the shielding gas flow.

In addition to the EOS M290 experiments, one single scan track built job for AlSi10Mg has been built on an EOS M400 system featuring a $1\,kW$ Yb fiber laser to extend the range of investigated Peclet numbers. The approach for building the single scan tracks was similar to the setup in an EOS M290: the substrate plate was placed in the center of the base plate, scratched with the recoater to locate height zero, and then a powder layer of $190\,\mu m$ was applied. However, the EOS M400 does not provide a leveling option for the base plate, and therefore the zero level height had to be taken as the highest point on the substrate, introducing a higher uncertainty in powder layer thickness compared to EOS M290 experiments. Furthermore, Nitrogen was applied as shielding gas, as Argon was not available on this specific machine. Instead of using a substrate holder the sample was glued to the center of a standard build plate with Al tape. Orientation of scan tracks and the scanning order in respect to the shielding gas flow were set

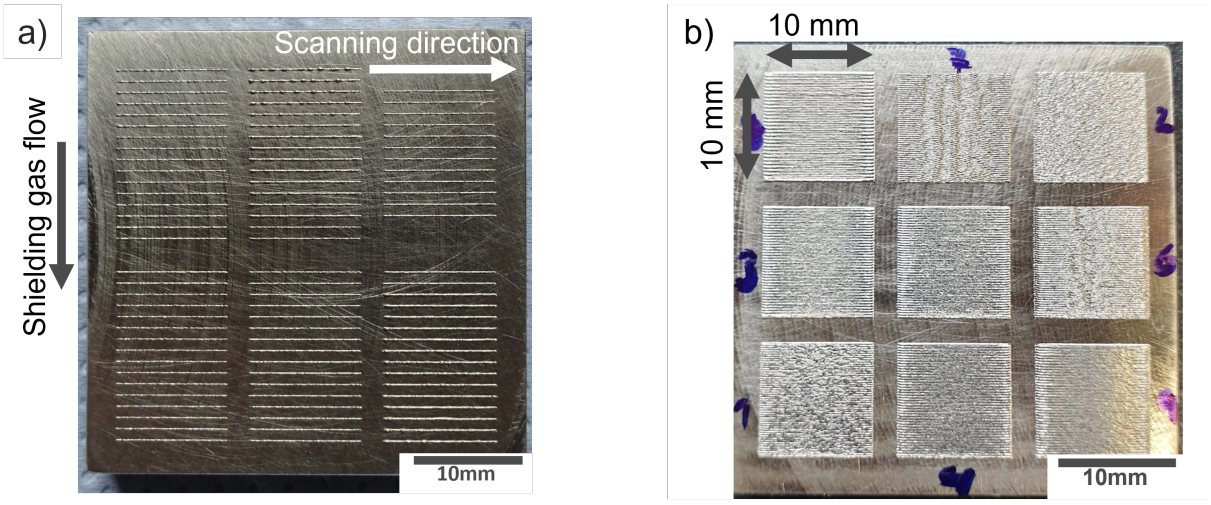

Figure 3.4: Photographs of a) single scan track and b) single layer hatch package samples; both built with $190\,\mu m$ applied powder layer thickness

similar to the EOS M290 experiments. The 86.5% laser beam diameter was measured using a Primes ScanFieldMonitor.

3.2.3 Hatch package experiments

To investigate the effect of applied powder layer thickness on melt pool dimensions, hatch packages with dimensions $10\,\mathrm{mm} \times 10\,\mathrm{mm}$ were built for IN718 at applied powder layer thicknesses of $190\,\mu\mathrm{m}$, $290\,\mu\mathrm{m}$, and $390\,\mu\mathrm{m}$. Hatch packages were used in this setup to additionally get a first outlook on the change of processing space from single scan tracks to hatches within a layer. The hatch package samples were built on an EOS M290 with similar setup as for the single scan tracks and hatches were scanned orthogonal to the shielding gas flow direction. To avoid short hatches and stripe boundaries within the hatch packages, a NoPattern scan strategy with alternating directions was applied (explained in Section 2.1.2.2 and Figure 2.4a). Nine process parameter sets (Table 3.4) were selected for this investigation. Five parameter sets were chosen to be within the process window predicted in Section 4.2.1 and two parameter combinations were selected outside the lower and upper process window boundary, respectively. Scan speeds were calculated from the set laser power P and the dimensionless enthalpy H^* by Equation 2.13. Prior to the hatch package experiments, single line scans were built at the same applied powder layer thickness variations and track widths were measured from topographic images recorded with the Keyence VR3200 3D surface profilometer. Those single line scan experiments were necessary to calculate the hatch distance for hatch packages, so that the ratio of scan track width to hatch distance would stay constant and similar to the standard ratio of 1.22. From the selected process parameter combinations, three sets were found to be outside the humping speed limit (Section 4.2.3) marked in light red in Table 3.4, and were therefore excluded from further analysis. A photograph of a fabricated hatch package sample is shown in Figure 3.4b.

Table 3.4: Parameter sets (PS) for IN718 hatch packages relative to standard values; scan speed for parameter sets marked in red is above the humping limit

PS	Laser power P	Dimensionless enthalpy H^*	Process window condition
1	-30%	-30%	outside lower boundary
2	+15%	-30%	outside lower boundary
3	-30%	Standard	inside process window
4	-15%	Standard	inside process window
5	Standard	Standard	inside process window
6	+15%	Standard	inside process window
7	+30%	Standard	inside process window
8	-30%	+30%	outside upper boundary
9	+15%	+30%	outside upper boundary

3.2.4 Three dimensional parts

To investigated the applicability of the proposed dimensionless process window to three dimensional parts, density cubes were built from PS 1, 4, 5, and 9 of the hatch package experiments (Table 3.4). Density cubes had dimensions $15\,\mathrm{mm} \times 15\,\mathrm{mm} \times 15\,\mathrm{mm}$ and were scanned on an EOS M290 with standard EOS parameters except for the adapted laser power, scan speed, and hatch distance. Neither contour nor Up- or DownSkins were applied. The sample cubes were built with a nominal layer thickness of $40\,\mu\mathrm{m}$, $60\,\mu\mathrm{m}$, and $80\,\mu\mathrm{m}$, respectively, to investigate the influence of layer thickness on the process window. Furthermore, ten parameter combinations selected based on previous single scan track experiments and an estimated process window for IN718 were applied to build additional density cubes with dimensions $10\,\mathrm{mm} \times 10\,\mathrm{mm} \times 13\,\mathrm{mm}$. Due to their small length scale, those cubes were built with NoPattern scan strategy and the Time Homogenization feature (see Section 2.1.2.2) to avoid overheating. Process parameter combinations were selected to result in $Pe > 4$ and H^*_{cd} between 2.2 and 4.3 (a complete list of parameter sets is given in Appendix A.4).

3.3 Characterization

3.3.1 Preparation

After processing, the substrate plates were cut with an ATM Brillant 240 cut-off saw. Parameters and cut-off wheel type were chosen in accordance with the substrate material. The cuts were conducted orthogonal to the single scan tracks or hatches within a hatch package, respectively, and both sides of each sample pair were embedded in one sample mount. The samples were cold mounted in acrylic resin (ClaroCit by Struers) and semi-automatically ground and polished with a final step of colloidal silica suspension (OPS by Struers, pH =9.8). For each material the corresponding in-house developed preparation procedure was used. To enable a visual contrast between the substrate and scan tracks, the samples were etched prior to microscopy, except for AlSi10Mg, for which good contrast was already achieved after the OPS polishing. Samples of IN718 and 316L were etched in Aqua Regia (1 part 65%-HNO_3 : 3 parts 37%-HCl) for $30\,\mathrm{s}$. MS1 was etched with Nital (3%-HNO_3 in ethanol) for $2\,\mathrm{min}$. Due to health and safety restrictions, the Ti64 samples could not be etched in-house and an external specialist, IABG, was commissioned. Density cubes for IN718 were sectioned parallel to the build direction, cold mounted, and semi-automatically ground and polished to OPS-finish. Only one cross section per density cube was embedded.

3.3.2 Cross section analysis

The etched cross sections were analyzed using an Olympus DP27 light optical microscope with Olympus Stream Software (Version 2.2). For each scan track, a separate micrograph was recorded. Besides the image file, a corresponding configuration file with the microscope settings, such as image resolution, was exported. Those two files were imported in an in-house developed software, called WeldSeamAnalyzer (WSA), to analyze the melt pool dimensions. The WSA was programmed by Dr. Peter Holfelder in Python code. It contains a database storing experimental information, micrographs, and analysis results, as well as a graphical user interface (GUI) enabling the user to draw Bezier curves around the melt pool borders. The dimensions melt pool depth, melt pool height, and melt pool width, measured at the interface between melt pool and substrate surface, were calculated from those Bezier curves. The definition of the different melt pool dimensions are visualized in Figure 3.5a. For each parameter set, melt pool dimensions were calculated from the average of four cross sectional micrographs.

Hatch packages were documented by stitching of multiple micrographs. Since only single scan tracks can be analyzed with the WSA, dimensions of hatches within a hatch package were measured with ImageJ [151]. For the first scan track, melt pool depth and height are taken as average from the two cross sectional micrographs. Stable hatch dimensions were measured from three hatches in the center region of the hatch package plus the last hatch on each cross section giving a total of eight measurements per parameter set. The last hatch was included, as it was the only hatch for which melt pool width could be measured due to the overlap between the other tracks.

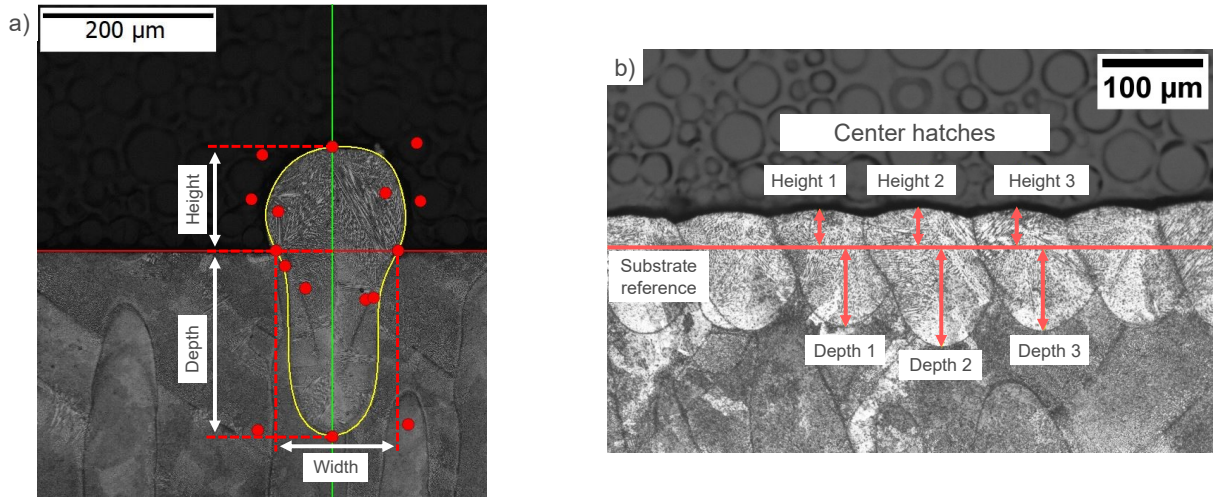

Figure 3.5: Micrographs illustrating measurements of melt pool dimensions for a) single scan tracks using WSA and b) hatch packages by ImageJ [151]

3.3.3 Analysis of topography

Prior to sample sectioning, the surface profile for single scan tracks as well as hatch packages was recorded using a Keyence VR3200 3D profilometer. It is a contactless profilometer based on multiple triangulation to calculate the height profile of a surface. Samples were measured in micro-mode with 40x magnification (measurement uncertainty of $\pm 3\,\mu m$ in height direction and $\pm 2\,\mu m$ in lateral direction). The surface profiles were processed in the VR-3000 G2 Series Analysissoftware (Version 2.5.0.332). The corresponding substrate surface was set as reference plane for each recording and the single scan track stability was then evaluated by drawing a profile line over the center of each single scan track. If the profile dropped to a height of $20\,\mu m$ or less from the reference surface, it was rated as instable, otherwise it was defined as stable. A topographic image and respective line profile measurements for a stable and an instable line are shown in Figure 3.6. Similarly, stability for hatch packages was defined based on line profiles along the first and last scan track. Since average height of the scan tracks changes with applied powder layer thickness, the limit for the maximum allowable drop of a stable line was adjusted for evaluation of the first scan tracks at powder layer thicknesses of $100\,\mu m$, $290\,\mu m$, and $390\,\mu m$ to $15\,\mu m$, $30\,\mu m$, and $40\,\mu m$, respectively. For the last scan tracks, those limits were halved to account for the lower average height for stable scan tracks within a hatch package compared to the first scan track.

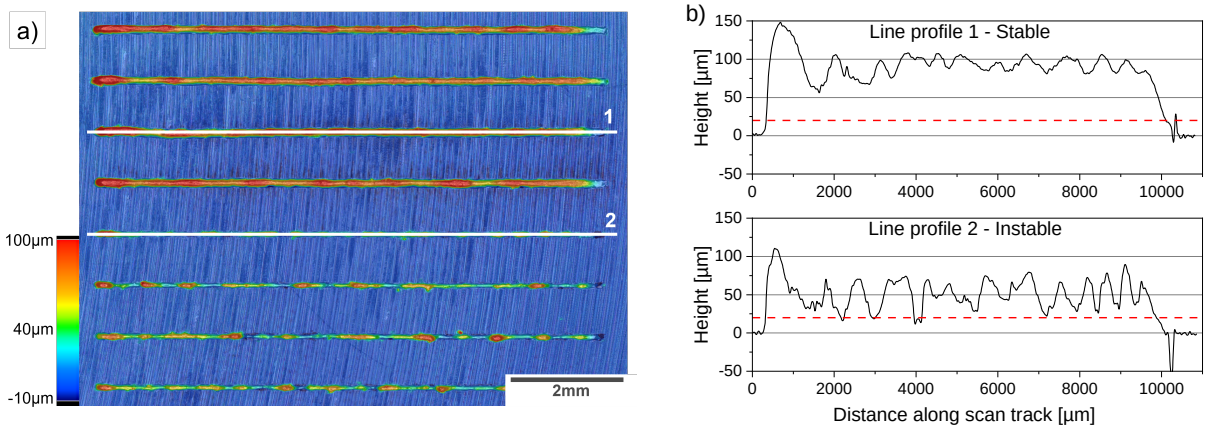

Figure 3.6: Characterization of surface stability for single scan tracks; a) topographic image of IN718 single scan tracks with line profiles for stability evaluation and b) line profiles for a stable single scan track (line profile 1) and an instable single scan track (line profile 2), red dotted lines indicate $20\,\mu m$ height

3.3.4 Density measurements

The density of the three dimensional samples was measured with two different methods. First, the density was determined by the Archimedes' principle according to DIN ISO 3369 [152]. The sample cube's mass in air m_{air} and destilled water m_{H_2O} was measured with a Kern 770-660 precision scale equipped with a Sartorius YDK 01 density measurement kit. To determine the water density ρ_{H_2O}, its temperature was measured with a Pt100 temperature sensor and the corresponding density taken from the table provided in the Sartorius handbook. Absolute density ρ_s of the sample cubes is then calculated based on Equation 3.2, including a correction factor for the sample holder given by Sartorius.

$$\rho_s = \frac{(\rho_{H_2O} - 0.0012)m_{air}}{(m_{air} - m_{H_2O})0.99983 + 0.0012} \tag{3.2}$$

To calculate the relative density ρ_r, a bulk density of $8.26\,\mathrm{g/cm^3}$ is taken as reference for IN718 (see Table 3.2). In addition, cross sections were prepared for each density cube to measure area fraction of porosity within the sample. The whole surface area of the cross section was recorded by stitching micrographs with 5x magnification using an Olympus DP27 light optical microscope with Olympus Stream Software (Version 2.2). Pores were then marked by automatic thresholding and any falsely indicated scratch or particle on the surface was manually removed from the selection. The area fraction of porosity, defect number, mean defect diameter, and maximum defect diameter were calculated and documented.

3.3.5 High speed video recordings

To analyze the observed change in Peclet number dependence of melt pool depth for single scan tracks (Section 4.1.2), high speed (HS) videos were recorded for IN718 at two process parameter sets selected from previous experiments. Parameter sets were chosen to result in Pe = 1.4 and Pe = 7.3 at constant H^* = 9.4. However, due to wrong laser linearization of the used machine, actual laser power output was higher than calculated giving the following output parameters: $99\,\mathrm{W}$ and $80\,\mathrm{mm/s}$ for Pe = 1.4 with H^* = 10.7 and $202\,\mathrm{W}$ and $410\,\mathrm{mm/s}$ for Pe = 7.3 with H^* = 9.7. For each parameter combination, three single scan tracks with length $7\,\mathrm{mm}$ were scanned on a substrate plate. The setup was similar to the standard single scan track experiments with applied layer thickness of $190\,\mu\mathrm{m}$. Due to the small field of view for the HS camera, the distance between consecutive tracks had to be reduced to $0.7\,\mathrm{mm}$. To record the HS videos, an EOS M290 was equipped with a Photron FASTCAM NOVA S12 HS camera and a CAVITAR CAVILUX®HF640 illumination laser. The illumination laser was fixed inside the process chamber, while the HS camera was mounted at a modified M290 front door, enabling close up viewing of the process zone. The setup is shown in Figure 3.7. For HS video recordings,

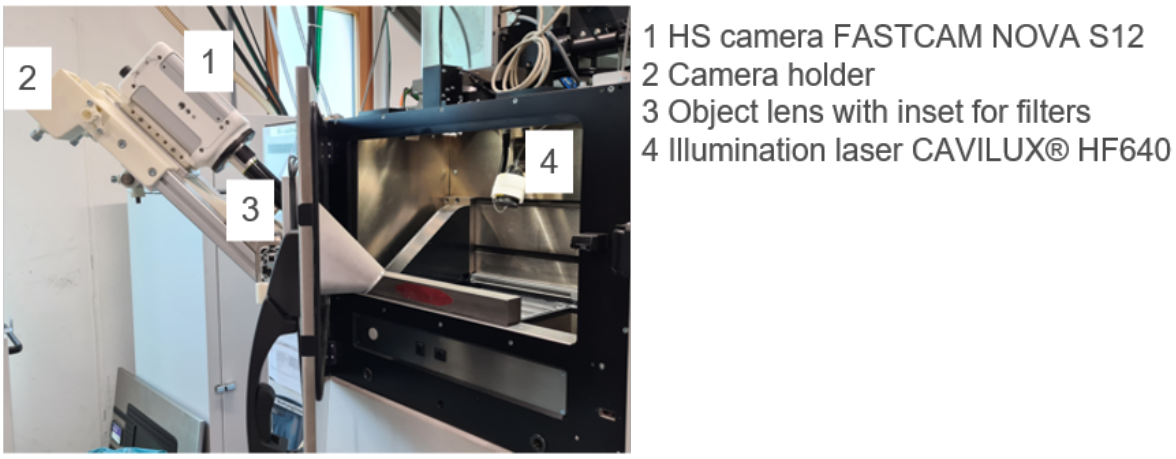

Figure 3.7: Setup of HS camera on EOS M290

the camera is set to 20000 fps resulting in $250\,\mathrm{frames/mm}$ and $49\,\mathrm{frames/mm}$ for each scan track with the lower and higher scan speed parameter, respectively.

4 Results and discussion

4.1 Characterization of melt pool dimensions

As the formation of stable and defect free single scan tracks is related to melt pool dimensions and morphology, the characterization of melt pool depth and width using dimensionless numbers is one of the major goals of this thesis. Furthermore, the knowledge of melt pool dimensions can enable the process developer to select geometry or application specific process parameters. For example, shallower melt pools might be favorable for overhang areas to reduce adhesion of the underlying powder particles. Additionally, based on the relation of dimensionless number and melt pool width of a single scan track, an appropriate hatch distance for hatch packages can be chosen. While a vast number of investigations exist on the dependence of melt pool dimensions and single processing parameters for specific materials [15, 51, 89, 117, 119–122, 127], dimensionless numbers are used in this work to correlate melt pool dimensions and process parameters in a more material and machine agnostic way. In the first subsection, the applicability of the dimensionless enthalpy, introduced in Section 2.3, to predict melt pool dimensions will be discussed. The results indicate that the dimensionless enthalpy alone is not a valid representation of the energy balance. Therefore, the influence of the Peclet number on melt pool dimensions is discussed in the second subsection. New dimensionless numbers, combining the dimensionless enthalpy and the Peclet number, are proposed in the last subsection together with their validation and an evaluation of the quality of prediction.

4.1.1 Influence of dimensionless enthalpy

The dimensionless enthalpy H^*, originally developed for estimation of melt pool dimensions in laser welding [143], has experienced increasing interest in the LPBF community [26, 28, 30, 56]. To validate the applicability of the dimensionless enthalpy H^* to predict melt pool dimensions, single scan tracks were fabricated and analyzed in accordance with the methods described in Section 3.2.2 and Section 3.3. In a first set of experiments, two alloys, IN718 and MS1, with a comparable range of thermophysical properties of the bulk materials (Table 3.2) and similar powder particle size distributions (Figure 3.1), were investigated. Those two alloys were chosen, as similar results in dependence of the dimensionless enthalpy H^* were expected. Additionally, experiments for MS1 were done on two different machines of the same type, EOS M290, to ensure machine comparability. Based on the EOS standard parameter set for the two materials, four levels of the dimensionless enthalpy were selected, standard, -30%, +30%, and 90% from standard, and corresponding process parameters were calculated based on Equation 2.13. To check that similar dimensionless enthalpy values will result in similar dimensionless melt pool dimensions for each enthalpy level, power was varied from the standard value to -30% and +30% of the standard and scan speed was adjusted accordingly.

Results for dimensionless melt pool depth and width are shown in Figure 4.1a and Figure 4.1b, respectively. Melt pool dimensions were normalized by the laser beam diameter a. As expected, melt pool dimensions increase with increasing H^* for both materials. The insets in Figure 4.1a examplarily illustrate the development of melt pool morphology with the dimensionless enthalpy. At low energy input, the melt pool has a shallow connection with the underlying substrate, making the scan track prone to instability due to the balling phenomenon (see Section 2.2.2). Therefore, instable lines are observed at those low values of H^* marked in the graphs by transparent symbols. For the lowest values of H^*, melt pool depth is less than half of the melt pool width, indicating conduction mode welding for those tracks (see Section 2.2.1 Equation 2.1). With increasing energy input, the melt pool depth is amplified due to keyhole formation, which increases the risk of keyhole instability (see Section 2.2.1) at the highest energy input. It can be noticed that melt pool depth shows a higher sensitivity to H^* compared to melt pool width, indicated by the steeper slope. This is in accordance with observations by Trapp et al. [146] and Keshavarzkermani et al. [120], who both observed a more pronounced increase in depth compared to width with increasing energy input. The higher sensitivity of melt pool depth compared to melt pool width can be explained by the Gaussian distribution of the laser beam in combination with the formation of a melt pool depression. As the highest intensity of the Gaussian beam is in the center, the melt pool center will experience the highest temperature, which might lead to material evaporation and the formation of a depression. Due to multi-scattering within the depression, even more energy will be distributed in the center of the melt pool which drives the increase of the melt pool depth and the formation of a deep keyhole. In contrast, melt pool width is mainly influenced by heat conduction. While this general trend is visible for both investigated alloys, the data of dimensionless melt pool depth separates for MS1 and IN718. Deeper melt pools are obtained for MS1 compared to IN718 at

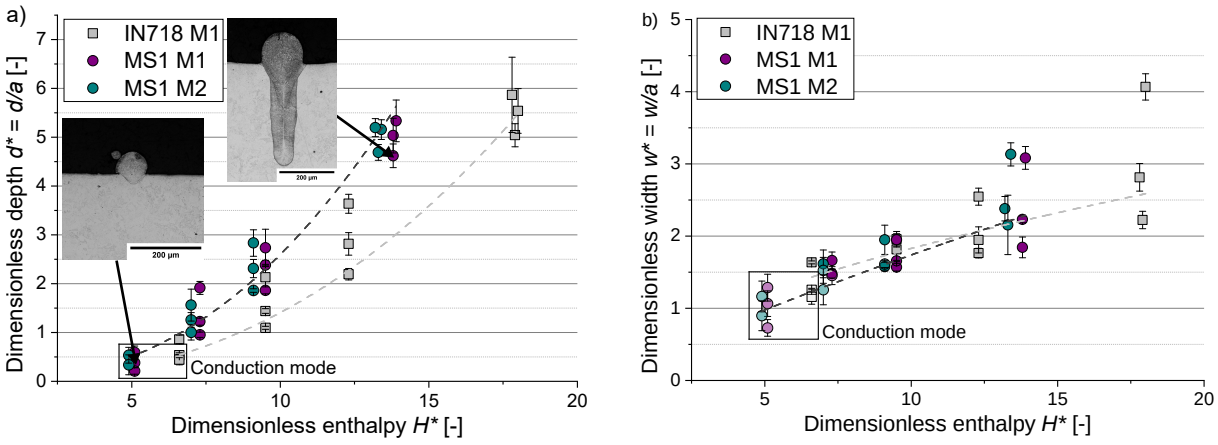

Figure 4.1: Dependence of melt pool dimensions on the dimensionless enthalpy H^* for a) dimensionless melt pool depth d^* with insets showing micrographs of melt pool cross sections and for b) dimensionless melt pool width w^*; experiments were done on machine M1 and machine M2; symbols with transparency indicate instable lines

similar dimensionless enthalpy. The two MS1 data sets fall close irrespective of which machine is used, and thus machine independence can be assumed for this experimental setup.

Besides the difference in data for IN718 and MS1, large scatter is observed within data sets from the same material obtained with different laser power and scan speed combinations at similar dimensionless enthalpy. Especially, one notes the large scatter for the IN718 samples at $H^* = 12.3$. Micrographs of cross sections for IN718 scan tracks built with varying process parameter combinations at $H^* = 12.3$ are shown in Figure 4.2a. Despite having similar H^*, melt pool dimensions, especially melt pool depth, decrease with increasing scan speed. A similar trend is depicted for MS1 in Figure 4.2b, showing micrographs of cross sections for single scan tracks built with $H^* = 9.5$. In accordance with the IN718 data, melt pool dimensions for MS1 decrease with increasing scan speed at constant H^*. Thus, it can be supposed that the dimensionless enthalpy cannot sufficiently characterize melt pool dimensions independent of actual process parameter settings and material. This finding is in contrast to Hann et al. [143] who observed a common trendline for dimensionless melt pool depth of stainless steel, vanadium, and titanium welds produced at different processing parameters. That a good fit of those data points was observed might be explained by comparing the range of investigated scan speeds, which was between $16\,\mathrm{mm/s}$ and $48\,\mathrm{mm/s}$ for the laser welding experiments compared to $130\,\mathrm{mm/s}$ to $3310\,\mathrm{mm/s}$ used for the present investigation. Due to the smaller range of scan speeds, its influence on melt pool dimensions might not have been as pronounced, and therefore

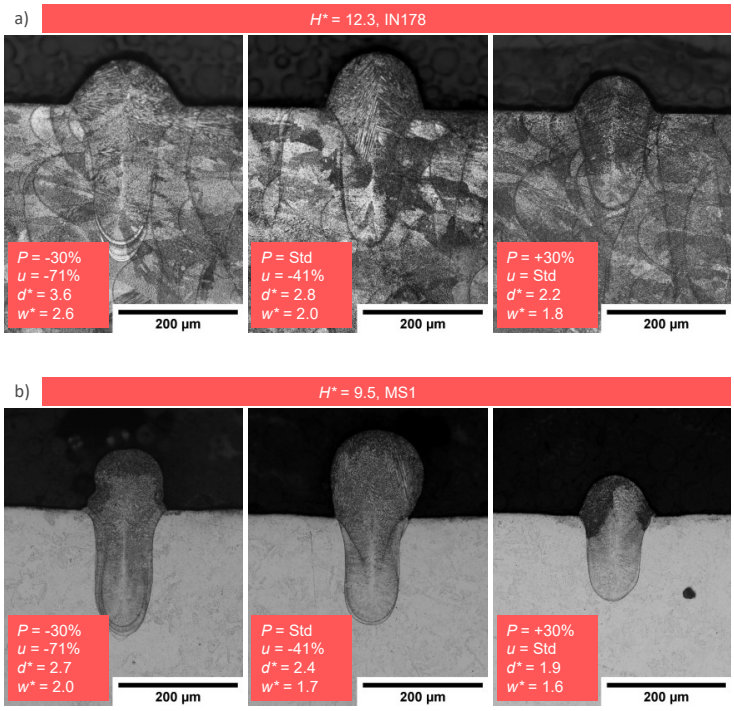

Figure 4.2: Micrographs of melt pool cross sections with similar dimensionless enthalpy H^* built by different process parameter combinations; a) $H^* = 12.3$, IN718 and b) $H^* = 9.5$, MS1

did not create as much deviation between the data points. Similarly, Gan et al. [28] found a linear relation between keyhole aspect ratio and the dimensionless enthalpy for Ti6Al4V, Al6061, and SS316 single scan tracks built under LPBF conditions, but without powder layer. However, they directly measured the keyhole dimensions via x-ray imaging and stated that their relation does not apply to melt pool depth analyzed by cross sectional investigations. While King et al. [56] did not investigate different alloys, they compared the relation of dimensionless melt pool depth and the dimensionless enthalpy for different processing parameters for LPBF of stainless steel and found a good correlation. Nevertheless, data scattered strongly above the keyhole threshold. Even in conduction mode the range of scatter was comparable to the one observed in Figure 4.1a. An in depth investigation whether this scatter was related to certain process parameter combinations was not given. However, comparison of the cross sections in Figure 4.2a and Figure 4.2b indicate that scan speed influences melt pool dimensions at constant H^*.

The influence of scan speed on the development of melt pool dimensions can be rationalized by taking into account the heat loss during the laser material interaction time. The definition of the dimensionless enthalpy in Equation 2.13 only relates the energy input by the laser to the energy required to melt the interacting material. However, some of the energy is lost to the surrounding substrate by heat conduction during the interaction of the laser with the material. Since the Peclet number characterizes heat loss, its influence melt pool dimensions for different materials is discussed in the next subsection.

4.1.2 Influence of Peclet number

4.1.2.1 Dependence on Peclet number

Since it was recognized from results of the previous section that melt pool dimensions vary with changing processing parameters at constant dimensionless enthalpy H^*, the dependence of melt pool dimensions on the Peclet number was investigated in more detail. The Peclet number was calculated based on Equation 2.6 with characteristic length a, characteristic velocity u, and thermal diffusivity D_l at $T_{liquidus}$. In this sense, it is a ratio of heat distribution by conduction through the material to heat distribution by the movement of the laser beam as convectional part. Results for single scan tracks built at varying Pe and constant H^* (with a small variation of 0.2, due to round-off error between calculated and applied P and u) for IN718 are shown in Figure 4.3. In accordance to the observations from Figure 4.2a, melt pool dimensions decrease with increasing scan speed, corresponding to increasing Pe. While this trend is valid for the full range of investigated Peclet numbers for melt pool width (see Figure 4.3b), a change in its dependence on Pe for $Pe < 4$ is observed for melt pool depth (see Figure 4.3a). At such low Peclet numbers, melt pool depth decreases with decreasing Pe, while the opposite trend is observed at higher Peclet numbers.

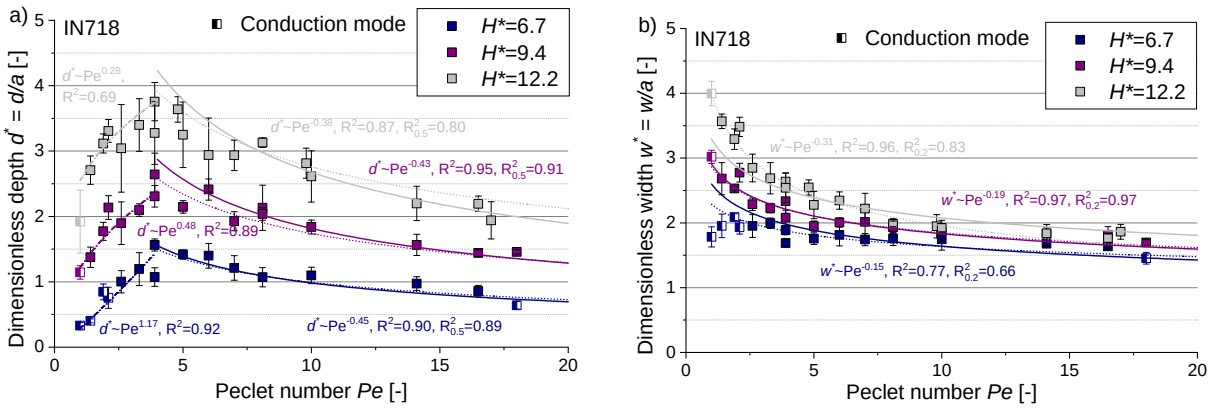

Figure 4.3: Dependence of melt pool dimensions on Peclet number Pe at constant dimensionless enthalpies H^* for a) dimensionless melt pool depth d^* and for b) dimensionless melt pool width w^*; solid lines are fit with a constant exponent, while dotted lines are best fits; R_x^2 values are R^2 values for an allometric fit with $d^* \propto Pe^{-x}$

To quantify the relation between dimensionless melt pool dimensions and the Peclet number, best fit lines were calculated using an allometric function of the form $c_1 Pe^{c_2}$. For melt pool depth, the two regions, $Pe \leq 4$ and $Pe \geq 4$, were fit separately. Despite a qualitatively similar trend for all three fits within the left region of Figure 4.3a and acceptable fit quality, with lowest R^2 of 0.69, exponents c_2 for the allometric fits decrease strongly with increasing H^*. Therefore, a quantitative description of the low Pe region for melt pool depth will not be given at this point. In contrast, the right hand region exponents for the allometric fit are closer together, indicating a common trend independent of H^*. This quantitative trend is taken as dimensionless melt pool depth being proportional to the inverse square root of the Peclet number. Therefore, additional to the dotted best fit lines, solid lines in Figure 4.3a represent allometric fits with a constant exponent of -0.5. Although the best fit exponents do not result exactly in a square root dependence, this constant exponent is chosen, as $1/\sqrt{Pe}$ represents the thermal diffusion length $L_d = \sqrt{Da/u}$ normalized by the beam diameter a. The importance of Pe on melt pool dimensions has also been recognized in laser welding literature as it influences the temperature distribution [79, 134, 137]. A decreasing trend of melt pool width and depth has, for example, been observed for laser welding by Lankalapalli et al. [137]. Additionally, a combination of the normalized thermal diffusion length and the dimensionless enthalpy has been successfully used in LPBF to relate melt pool depth for varying alloys and process conditions [26, 27, 142]. However, a transition in Pe dependence at constant dimensionless enthalpy, as observed in this work, has not been reported experimentally in those investigations. This might be because only scan speeds higher or equal to $500\,\mathrm{mm/s}$ were applied by Ye et al. [27], resulting in $Pe > 5$ for 316L and IN625 and $Pe > 3$ for Ti64. In fact, a theoretical discussion about the change in Pe number dependence is given in Rubenchik et al. [26] and will be referred to in Section 4.1.2.3. However, no experimental evidence was presented there.

In contrast to dimensionless melt pool depth, a change in Pe dependence cannot be observed for melt pool width (see Figure 4.3b). Except for the lowest H^* data set for which a decrease in width can be observed for data points with the lowest Pe values. In this case, the decrease in width can be attributed to a change from keyhole to conduction welding. As for melt pool depth, best fit lines and allometric fits with constant exponent of -0.2 are shown. To describe the relation of melt pool width with Pe, the exponent of -0.2 is chosen as average between the observed best fit exponents. This is in the range of results for micro laser welding by Patschger et al. [136], who calculated a proportionality of dimensionless melt pool width to $Pe^{-0.363}$ and $Pe^{-0.207}$ depending on the welding mode. One has to note that those investigations were done on full penetration welds which might explain the slight deviation from the observed exponent.

Since the variation of Pe was achieved by an adjustment of the scan speed u, laser power had to be decreased at low Pe to enable constant H^*. Therefore, at the lowest Pe numbers, the melting mode was observed to transition from keyhole to conduction mode. This is indicated in Figure 4.3 by the half-open square symbols. For simplification, absorptivity was set as constant in the dimensionless enthalpy equation, although effective absorptivity will change when transitioning to keyhole mode welding and varies with keyhole depth and shape [146, 153]. Absorptivity is low in conduction mode due to the relatively flat metal surface. It then sharply increases when changing to keyhole mode welding, finally saturating at a considerably higher value compared to the absorptivity measured for a flat metal surface. For example, absorptivity of 316L was observed to increase from about 0.3 for conduction to 0.78 at the saturated keyhole regime [146]. Thus, a drop in melt pool depth and width is expected when changing from keyhole to conduction mode at constant H^*. However, the change in Pe dependence is not only observed for conduction mode samples, but also occurs for samples in keyhole mode welding. A comparison of a melt cross section in conduction and keyhole mode welding at similar Pe is shown in Figure 4.4. From the typical elongated wine cup shaped cross section on the right side, it is clear that this sample is in a deep keyhole state. It is, therefore, assumed that the Pe dependence of melt

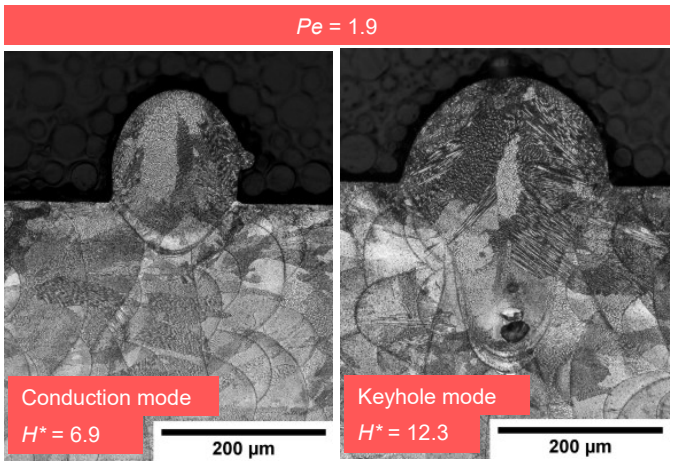

Figure 4.4: Micrographs of melt pool cross sections at similar Peclet number Pe at different dimensionless enthalpies H^* for IN718

pool dimensions and its change in behavior for melt pool depth is not solemnly due to a change in welding mode.

4.1.2.2 Influence of material feed

Since three dimensional parts are created in LPBF by consolidating multiple powder layers upon each other, the application of powder adds additional physical phenomena and complexity to the LPBF process compared to laser welding. Besides melting the substrate, energy has to be spent to consolidate the powder layer. In this work, a constant powder layer thickness was applied on top of the substrate plates, and therefore the part of energy spent on melting the powder should be constant for all tested parameter sets and not influence the results relative to each other. However, in reality, the powder layer is not a fixed solid and material redistribution can change material feed considerably. Powder particles were observed to be dragged towards the laser-powder interaction zone by the Bernoulli effect of the vapor plume in keyhole mode welding [62–64]. This creates the denudation zone, a region around the melt pool depleted of powder. The attracted powder particles can either get entrained in the melt pool area or get ejected with the vapor plume and redeposit at other locations on the powder bed. Thus, the amount of powder actually interacting with the laser can vary in dependence of process parameter settings. To depict a possible effect of material feed on melt pool depth, data from Figure 4.3a is re-plotted in terms of dimensionless total depth d_t^* (the sum of depth d and height h, normalized by a) in Figure 4.5. In accordance with Figure 4.3a, the relation between dimensionless total depth d_t^* and Pe changes around $Pe \approx 4$. The high Pe region is still showing a good agreement with the previously observed inverse square root dependence. At $Pe < 4$ dimensionless total depth d_t^* seems to saturate for $H^* = 6.6$ and slightly decreases for the two higher dimensionless enthalpies. However, the decrease is not as severe as for dimensionless depth alone, dropping by about 0.5 for d_t^* compared to around 1 for d^*.

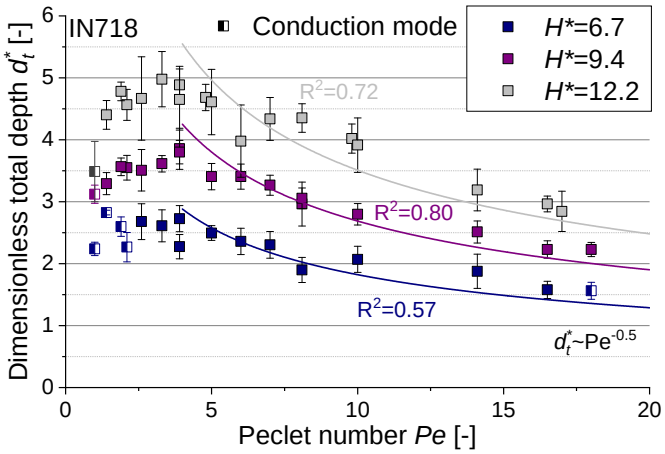

Figure 4.5: Dimensionless total depth d_t^* over Peclet number Pe at constant dimensionless enthalpies H^* for IN718; $d_t^* = (d + h)/a$

To further understand the influence of powder feed, HS video recordings were done according to the experimental setup in Section 3.3.5 for parameter sets with $Pe = 1.4$ and $Pe = 7.3$. Due to some issues with the machine calibration, process parameters do not exactly match parameter sets for the data presented in Figure 4.5. However, as the Pe number dependence is similar for different H^*, a comparison is assumed to be valid. Snapshots from those HS video recordings are shown in Figure 4.6. Since the powder flow is difficult to see from the snapshot images, the powder flow direction observed on the video recordings is indicated by red arrows. A wide denudation zone can be seen for the scan track built with Pe = 1.4 in Figure 4.6a. In this case, powder is dragged towards the single scan track over a large area around the laser-powder interaction zone, leaving a wide region adjacent to the single scan track depleted of powder particles. In contrast, no clear denudation zone can be detected from Figure 4.6b for Pe = 7.3 and the powder flow is more chaotic. For this sample, powder is sucked towards the scan track, but also expulsed from the laser-powder interaction region. As discussed in Section 2.2.1, the keyhole front wall angle increases with increasing scan speed, resulting in a tilt of the expulsed vapor plume. Despite attracting powder particles from the surrounding area, the tilted plume can also interact directly with the powder bed pushing particles away from the interaction zone [62]. This can explain that powder is also blown away from the interaction zone at high scan speed in Figure 4.6b.

Thus, while experimentally material addition was kept constant, the dependence of powder entrainment on process parameters can lead to a difference in powder material volume contributing to the consolidated melt track. This could lead to a decrease in melt pool depth with an increase in material addition, as a higher fraction of energy is spent to melt powder instead of substrate material. While the difference in material feed certainly has an influence on melt pool depth and stability, especially at low energies where a small change in melt pool depth easily creates instability, it is not assumed to be the only contributing mechanism to the decrease of melt pool

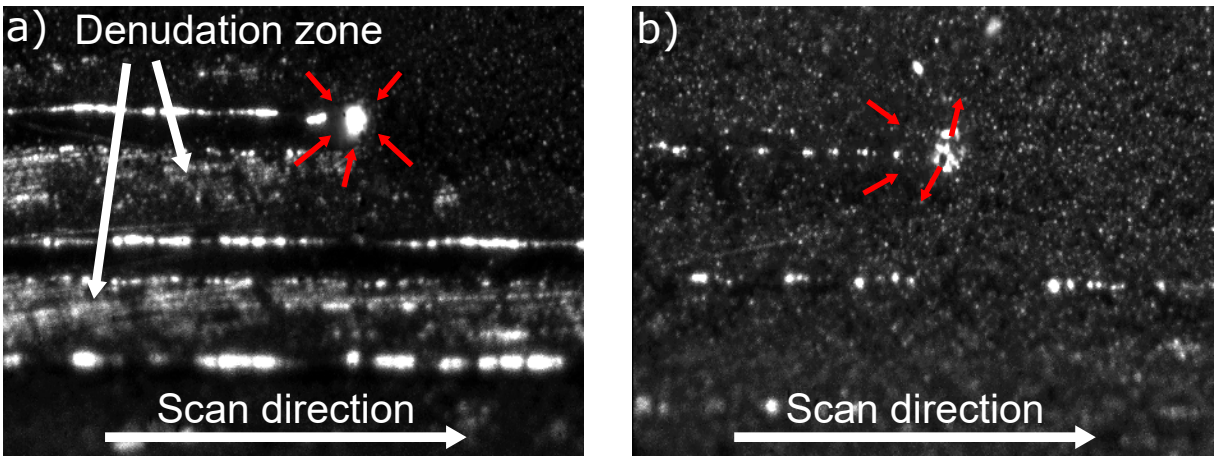

Figure 4.6: Snapshots from HS video recordings for a) $Pe = 1.4$ at $H^* = 10.8$ and b) $Pe = 7.3$ at $H^* = 9.7$; red arrows indicate the direction of powder movement as observed from the video recordings

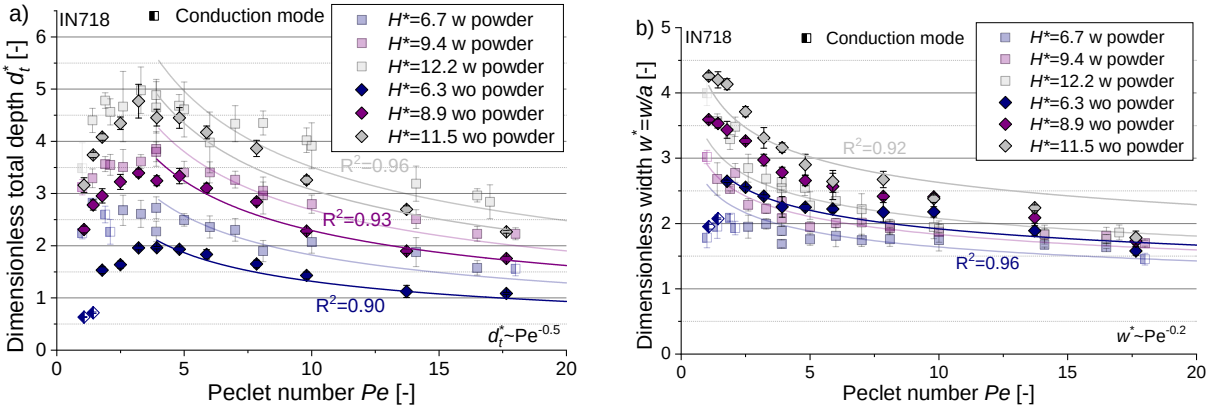

Figure 4.7: Dependence of melt pool dimensions on Peclet number Pe at constant dimensionless enthalpies H^* for bare plate experiments; a) dimensionless melt pool depth d^* over H^* and b) dimensionless melt pool width w^* over H^*

depth below a certain Pe number. This assumption is rationalized as first, not all of the attracted powder is contributing to the molten material and second, even total depth decreases for small Pe (Figure 4.5). To substantiate this assumption, the influence of Pe on melt pool dimensions was additionally investigated for single scan tracks made on bare plates without powder. Results are shown in Figure 4.7 in comparison with data for $190\,\mu m$ powder layer thickness. Qualitatively, the data is in good agreement with previous results from samples with powder addition. Good fits are achieved for allometric functions with exponents of -0.5 for melt pool depth and -0.2 for melt pool width. While melt pool width increases for all investigated Pe values, the relation to melt pool depth changes at Pe of around 4 as observed for samples built with powder. Furthermore, a clear separation of the data points for samples in conduction mode is visible for both melt pool dimensions. This reassures that the decrease of melt pool depth at $Pe < 4$ is most likely not caused by a transition in welding mode. Thus, in addition to material feed, another physical phenomenon has to be responsible for the change in Pe dependence at low and high Peclet numbers and will be discussed in the following section.

4.1.2.3 Change in heat distribution mechanism

By its definition in Equation 2.13, the dimensionless enthalpy gives a ratio between energy input by the laser and energy required to melt the interacting volume of material. A ratio greater than one is needed to melt the material, as energy is lost during the interaction, e.g., by vaporization of material or conduction of heat to the surroundings. The Peclet number describes the ratio of heat conduction to heat convection, and thus is a measure of heat loss during the laser material interaction. At high $Pe >> 1$, meaning high scan speed, low thermal diffusivity, and/or large beam size, heat is concentrated within a small area around the interaction zone and heat loss to the sides of the interaction zone is negligible. However, in case of $Pe << 1$, heat diffusion during the interaction time is larger than the beam size and heat flow to the surrounding is

non negligible. This can be illustrated from the different terms of Equation 4.1, calculating the maximum surface temperature T_c for a moving Gaussian beam for $Pe < 10^1$ [79].

$$T_c = T_0 + \frac{2AP}{\sqrt{2\pi}\rho c_p D a} \exp\left(\frac{a^2u^2}{128D}\right) erfc\left(\frac{au}{\sqrt{128}D}\right) \tag{4.1}$$

This equation can be converted to Equation 4.2 only containing H^* and Pe as variables.

$$T_c = T_0 + \Delta T\sqrt{\frac{\pi}{8}} H^* \sqrt{Pe} \exp\left(\frac{Pe^2 D}{128}\right) erfc\left(\frac{Pe}{\sqrt{128}}\right) \tag{4.2}$$

The functional terms containing Pe, except the exponential part, are plotted separately in Figure 4.8. The exponential term is always close to one because of the small values of D and is therefore not plotted. At $Pe << 1$ the inverse error function term approaches a value of 1, and thus the moving Gaussian beam equation converges to the stationary Gaussian beam solution. The maximum surface temperature is then mainly determined by the square root term, meaning that T_c increases with increasing Pe, which is in qualitative agreement with the experimentally observed behavior. With increasing Pe, the error function term approaches zero, thereby decreasing the overall surface temperature with increasing Pe. Using a similar rationalization, Rubenchik et al. [26] suggest that melt pool depth mainly depends on H^* at $Pe > 1$, while it is suggested to additional dependent on $\sqrt{Pe}$ for $Pe << 1$. In addition to the two Pe terms of Equation 4.2, an inverse square root function is plotted in Figure 4.8 to indicate the experimentally observed relation. For Pe between 1 to 10, the error between the inverse square root function and inverse error function is small, indicating a comparable scaling for those

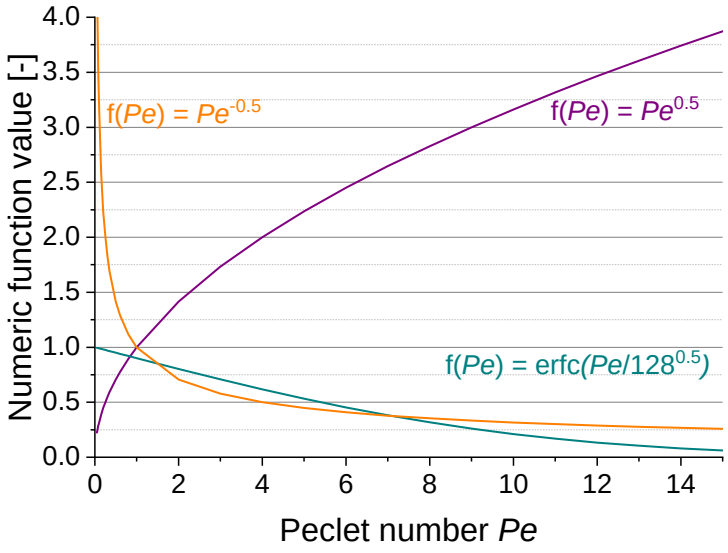

Figure 4.8: Functional relationship of the terms within the moving Gaussian beam solution with Pe; the inverse square root of Pe is additionally plotted for comparison

[1] The Pe range was adapted to account for a different definition of Pe in [79] compared to this work.

two terms. The inverse square root trend of melt pool depth with Pe can be further rationalized for $Pe >> 1$, using the one-dimensional heat flow equation, as heat loss in transverse direction of the melt pool can be neglected at such high speeds. For simplicity a Dirichlet boundary condition is chosen, resulting in the following solution:

$$\frac{T(z,t) - T_s}{T_0 - T_s} = erf\left(\frac{z}{2\sqrt{Dt}}\right) \tag{4.3}$$

with constant surface temperature $T_s = T_b$, initial temperature T_0, and interaction time t. In case of a moving laser beam, the interaction time is taken as $t = a/u$. Since the coordinate is searched where the temperature has reached the solidus temperature, Equation 4.3 can be converted to

$$d^* = \frac{z_{solidus}}{a} = erfc\left(\frac{T_{solidus} - T_b}{T_0 - T_b}\right)\frac{2}{\sqrt{Pe}} \tag{4.4}$$

resulting in an inverse square root scaling of d^* with Pe. Thus, qualitatively, the different trend lines observed experimentally at low and high Pe can be explained based on heat distribution. The decrease of melt pool depth at small Pe can be attributed to an increase in heat loss. Since heat distribution mechanisms should be similar at comparable Pe, material dependence is not expected and the transition point value should stay constant for all investigated alloys.

To check the material dependence of the transition point, additional experiments were done on a bare substrate for AlSi10Mg and with a $190\,\mu m$ powder layer for AlSi10Mg, 316L, MS1, and Ti64. In all experiments, H^* was kept constant while Pe was varied. The results are shown in Figure 4.9. Comparing the results for IN718 and AlSi10Mg for bare plate substrates without powder, a similar Pe dependence is observed. At high Pe, dimensionless total depth d_t^* scales with the inverse square root of Pe, while at low Pe an increase in d_t^* with Pe is observed. However, the transition is shifted to a lower value for AlSi10Mg, between $Pe = 1$ to 1.8, compared to observations for IN718. In contrast to IN718, a tendency for a change in Pe dependence is also visible for melt pool width for AlSi10Mg. For samples in keyhole mode, melt pool width seems to slightly decrease at the smallest Pe numbers (data point at $Pe = 1.4$ for $H^* = 3.8$, $Pe = 1.0$ for $H^* = 4.2$, and $Pe = 0.7$ for $H^* = 5.0$). Similar results are observed for the experiments with $190\,\mu m$ powder layer in Figure 4.9c and Figure 4.9d. For all investigated alloys, the data sets for dimensionless melt pool depth show a good match with the $\sqrt{Pe}$-fits. While the transition happens around $Pe = 4$ for IN718 and the steels, 316L and MS1, it shifts to lower values for Ti64 and AlSi10Mg. The ranges for the transition values are marked by shaded areas of different color in Figure 4.9c. Melt pool width increases monotonically with decreasing Pe for all alloys, except AlSi10Mg for which a decrease in width is observed at the smallest Pe numbers in conduction as well as keyhole mode. Furthermore, it is interesting to note that despite having the second lowest H^*, AlSi10Mg obtains the highest dimensionless melt pool widths. A deeper discussion on this observation is given in Section 4.1.3.2. Both experimental setups indicate that the transition value for the Pe dependence is material dependent, which

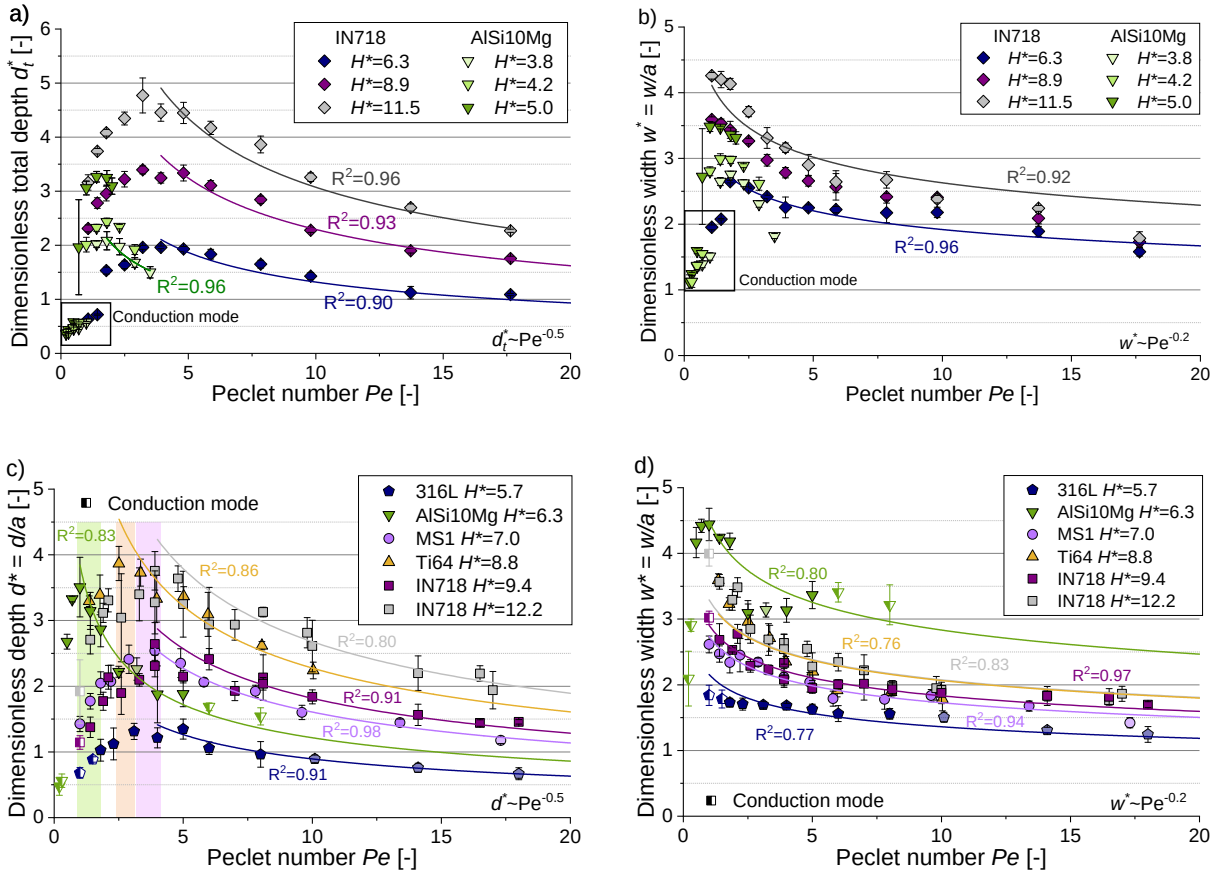

Figure 4.9: Dependence of melt pool dimensions on Peclet number Pe at constant dimensionless enthalpies H^* for different alloys; a) dimensionless total depth d_t^* and b) dimensionless melt pool width w^* over Pe for bare substrate experiments, and c) dimensionless melt pool depth d^* and d) dimensionless melt pool width w^* over Pe with 190 µm powder layer; transparent symbols indicate instable lines; colored areas in c) indicate range for transition values

was not expected from the arguments based solemnly on the heat loss by heat conduction to the surrounding material.

Besides on energy input itself, melt pool dimensions also depend on the distribution of heat. Since the Marangoni convection influences heat distribution inside the melt and the melt pool shape [113, 116], in this work, it is suggested that melt convection additionally contributes to the observed change in Pe dependence. While at high scan speeds melt flow is mainly to the back of the melt pool, due to the pressure of the vapor cavity, at low scan speeds the Marangoni convection around the keyhole might play an important role. The influence of heat transfer due to convection of the molten material to heat conduction can be characterized by the Peclet number Pe_{MP} (Equation 2.7). Instead of scan speed u, the velocity of the molten metal inside the melt pool is used to calculate Pe_{MP}. Since actual melt velocities could not be measured within this work, the absolute contribution of convectional flows inside the melt pool to the distribution of heat is not quantified. However, studies by Mukherjee et al. [138] and Rai et al. [116] showed the importance of convectional flow in heat distribution for alloys with low

thermal diffusivity. Furthermore, Mukherjee et al. [138] found a positive relation of Pe_{MP} and the Marangoni number Ma, which is a measure for the strength of the Marangoni convection. The observed decrease of melt pool depth at low Pe and constant H^* is, therefore, suggested to result from the redistribution of heat due to the Marangoni convection inside the melt pool. Since the investigated steels obtain a negative surface tension gradient with temperature, melt will flow from the keyhole rim to the boundary. Thereby, heat is distributed from the hot to the cold area, increasing melt pool width but decreasing melt pool depth. This matches with the observed decrease in melt pool depth and increase in melt pool width at low Pe. Examining the melt pool shapes of IN718 samples from the bare substrate experiments at Pe below and above the transition point in Figure 4.10a, both melt pool cross sections show a wide spread at the top and a slender penetration part at the center resulting in a wine cup shape. The increase in melt pool width near the surface can be attributed to the Marangoni convection. In contrast, a wine cup shape is not observed for the AlSi10Mg cross sections in Figure 4.10b. For high thermal diffusivity alloys, such as AlSi10Mg, heat is mainly distributed by conduction and the shape of the melt pool is not strongly influenced by the melt pool convection [79].

To further characterize the influence of the Marangoni convection, its strength is estimated by the Marangoni number Ma, defined in Equation 2.8. The characteristic length is set to 1 to enable a comparison solemnly based on the thermophysical properties of the investigated alloys. The thermophysical properties used for calculation are listed in Table 4.1. A transition from

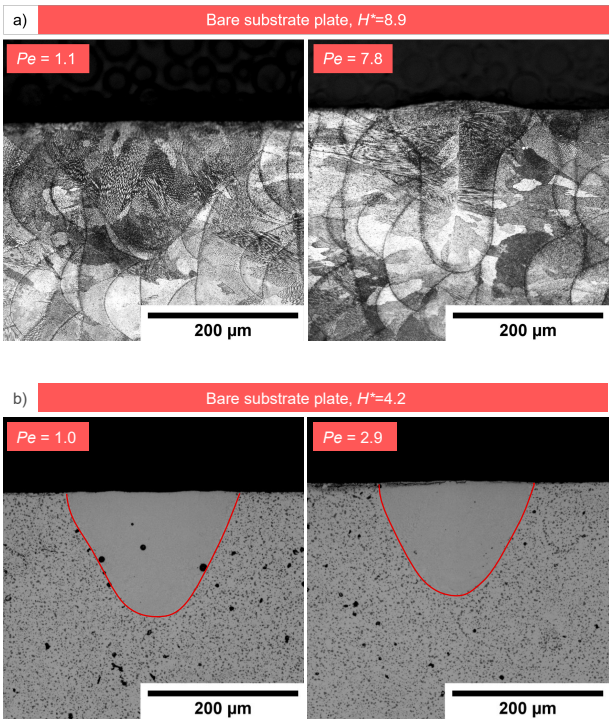

Figure 4.10: Micrographs of melt pool cross sections below and above the Pe transition for bare plate experiments of a) IN718 and b) AlSi10Mg

Table 4.1: Thermophysical properties to calculate Ma; T_b is taken from Fe for steels [154], Al for AlSi10Mg [148], and Cu for CuCrZr [155]; η and $\delta\sigma/\delta T$ for CuCrZr are taken from Cu [156, 157]

	Thermal diffusivity D_l	Boiling temperature T_b	T_b-$T_{solidus}$	Dynamic viscosity η	Surface tension gradient $\frac{\delta\sigma}{\delta T}$
	10^{-6} [m^2/s]	[K]	[K]	[mPa s]	[mN/(m K)]
IN718 [144, 147]	4.5445	3133	1605	6.3	-0.2952
MS1 [144]	5.7697	3133	1474	5.6	-0.3212
316L [144]	5.4662	3133	1480	6.0	-0.3207
Ti64 [144, 145, 148]	7.8416	3533	1655	4.0	-0.24
AlSi10Mg [144]	29.0974	2743	1917	1.2	-0.2122
CuCrZr [158]	32.5886	2840	1519	3.1	-0.2
W [159–161]	12.9757	6101	2414	8.5	-0.31

positive to negative surface tension gradient was calculated by JMatPro [144] for AlSi10Mg at temperatures above 1000 K and only the slope of the negative gradient is taken into account here.

The resulting Marangoni numbers for the investigated alloys are shown in Figure 4.11. It can be seen that a decrease in Ma correlates with a shift in the Pe transition to lower values (closer to 1). This would be expected, considering only the change in heat distribution mechanism from heat conduction to the laser beam movement. This correlation gives another hint that the Marangoni convection might be responsible for the change in Pe dependence for the melt pool depth of low thermal diffusivity alloys. Additionally, Ma has been calculated for CuCrZr and W which both should behave similar to AlSi10Mg in terms of Pe dependence and could be investigated in further studies to validate the proposed hypothesis.

To conclude, the observed dependence of melt pool dimensions on Pe as well as the transition in Pe dependence for melt pool depth is not solemnly related to one physical phenomenon, but an interplay of material feed as well as different heat distribution mechanisms, conduction,

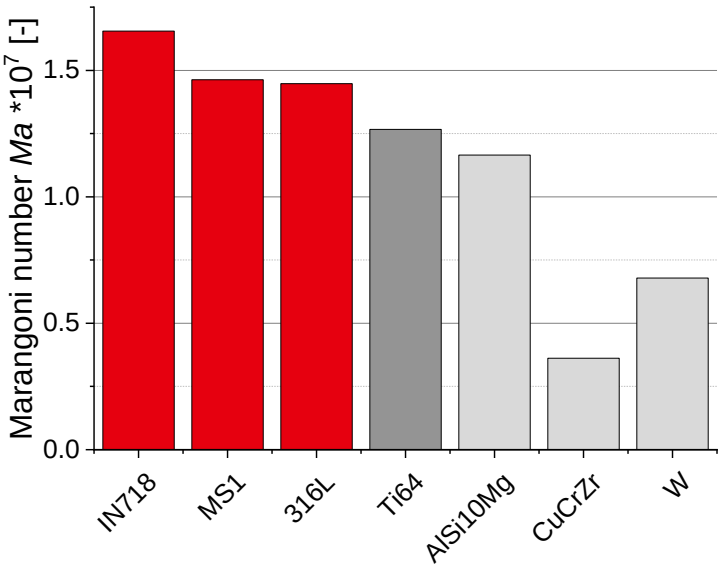

Figure 4.11: Comparison of Marangoni number Ma for different alloys based on thermal properties in Table 4.1

melt pool convection, and the moving beam. In cases where conduction is more significant to heat distribution than the moving beam, melt pool depth will qualitatively follow the unmoving beam solution, positively correlating to Pe. In contrast, at high speeds, when heating is mainly due to the movement of the laser beam, melt pool depth and width decrease with increasing Pe. In addition, heat distribution by convection inside the melt pool leads to a transition of Pe dependence already at $Pe > 1$. With increasing importance of this convective part, decreasing thermal diffusivity and increasing Ma, the transition shifts to higher values. Since laser beam size was not changed within this work, it would be of interest for supplemental research activities to investigate how a change in laser beam size affects the Pe dependence.

4.1.3 Combination of dimensionless enthalpy and Peclet number

Within the previous sections, it has been shown that the dimensionless enthalpy H^* cannot be used to characterize the effect of process parameters on melt pool dimensions on its own. The Peclet number Pe has to be taken into account to consider the effect of heat distribution. Therefore, two dimensionless numbers combining Pe and H^* are suggested to separately scale melt pool width and melt pool depth. The proposed dimensionless numbers will be compared to experimental investigations and their usability discussed within the following two subsections.

4.1.3.1 Dimensionless melt pool depth

For dimensionless melt pool depth, the depth corrected dimensionless enthalpy H^*_{cd} is introduced:

$$H^*_{cd} = \frac{H^*}{\sqrt{Pe}} \tag{4.5}$$

Since a common exponent for the allometric fits could not be found at low Pe, H^*_{cd} is defined such that it will only apply to combinations of process parameters and materials were the inverse square root scaling of Pe is valid. Results of dimensionless melt pool depth for IN718, 316L, MS1, and Ti64 are plotted over H^*_{cd} in Figure 4.12. Only data with $Pe > 4$ is used for those plots to ensure validity of the inverse square root scaling. Furthermore, data from parameter sets with speeds greater than $1260\,\mathrm{mm/s}$ for IN718, $1240\,\mathrm{mm/s}$ for MS1, $1200\,\mathrm{mm/s}$ for 316L, and $1550\,\mathrm{mm/s}$ for Ti64 have been excluded. Those speeds denote the humping limit, which will be discussed in more detail in Section 4.2.3. Fulfilling the aforementioned conditions, all data sets fall within a common curve for dimensionless melt pool depth d^* despite different thermophysical properties of the investigated alloys. To find the relation between d^* and H^*_{cd}, data was fit with an allometric equation resulting in a best fit expression of $d^* = 0.559 H^{*1.17}_{cd}$. The 95% prediction band, the area where 95% of data falls in, is indicated as gray region. It can be seen that data for Ti64 falls mostly on the upper side of the fit, while data for IN718 falls on the lower side, indicating that there is still some material dependence. However, it has to

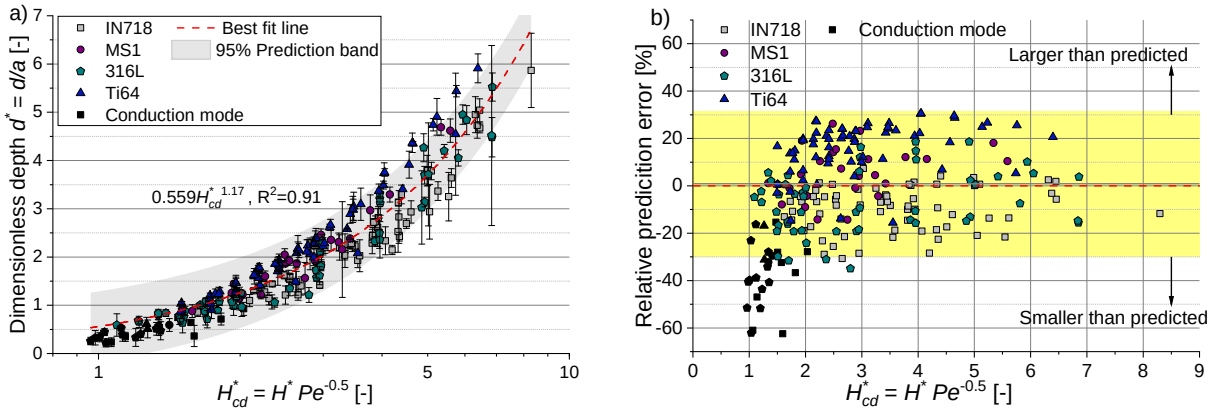

Figure 4.12: Prediction of dimensionless melt pool depth d^* by depth corrected dimensionless enthalpy H^*_{cd}; a) dimensionless melt pool depth d^* over depth corrected dimensionless enthalpy H^*_{cd} and b) corresponding error of measured means to predicted values; yellow band indicates error for 95% of data

be taken into account that the calculation of dimensionless numbers was based on temperature independent thermophysical properties and estimated absorptivities of the respective alloys which might rationalize the observed discrepancies. To check the prediction's quality, relative errors of measured to predicted melt pool depths were calculated for all data points and are plotted in Figure 4.12b. Figure 4.12a shows that melt pool depths for conduction mode samples are over-predicted by the fit, resulting in large errors up to -62%. Nevertheless, by taking only data for samples in keyhole mode into account, the prediction's accuracy is increased. As indicated by the yellow area, 95% of all data points in this mode fall within a -30% to 32% relative prediction error. Data for IN718 is mostly over-predicted, while data for Ti64 is mainly under-predicted. For 316L and MS1, data scatters around zero, indicating a more equal spread of the prediction error on both sides. Furthermore, no trend in the prediction error with H^*_{cd} is visible for IN718, while for Ti64, 316L, and MS1 over-prediction is slightly increased at very low H^*_{cd} ($H^*_{cd} < 2$).

To validate the fit, data from AlSi10Mg experiments, which have not been previously included in the fitting, are plotted in Figure 4.13. Using AlSi10Mg as validation material is especially interesting due to its contrasting thermophysical properties compared to the previously investigated alloys (see Table 3.2). In comparison to the investigated steels, thermal diffusivity for AlSi10Mg is nearly one order of magnitude higher, while volumetric enthalpy of melting is only about one third of the volumetric enthalpy of melting for the steels. For AlSi10Mg, additional experiments were conducted on an EOS M400, equipped with a $1\,\mathrm{kW}$ laser, to extend the range of Pe numbers that can be investigated (setup described in Section 3.2.2). Since it was observed that AlSi10Mg was following the same Pe dependence, with the transition range shifted to lower Pe numbers, data sets with $Pe \geq 1.8$ were included for evaluation. Figure 4.13 shows that especially the EOS M290 data set falls close to the prediction, with a maximum error for keyhole mode samples of -18% to 15%. Those values are within the previously proposed 95% prediction error of -30% to 32%. For conduction mode samples, the maximum error is -45%.

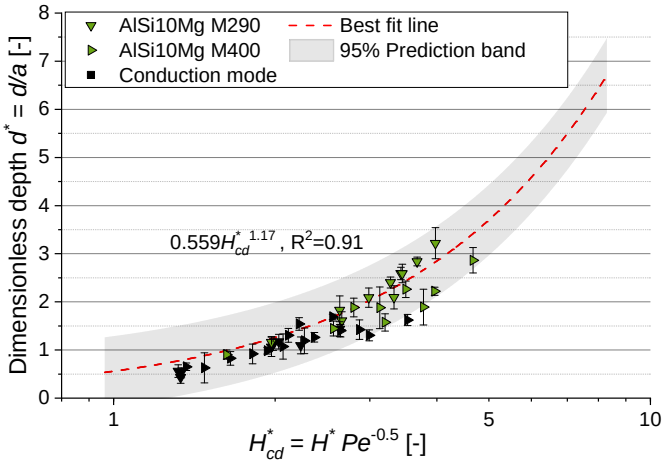

Figure 4.13: Comparison of AlSi10Mg data sets with best fit for dimensionless melt pool depth d^* of Figure 4.12

Data for melt pool depth of EOS M400 experiments falls on the lower part of the prediction band, and thus is mostly over-predicted. In keyhole mode, errors range from -28% to 1% and in conduction mode from -35% to 9%. Overall, a good fit for dimensionless melt pool depth is also obtained for AlSi10Mg, with an error for keyhole mode samples in a similar range to the previously investigated low thermal diffusivity alloys.

Thus, it can be stated that melt pool depth can be predicted for different alloys to within $\pm 32\%$ by the proposed allometric fit, which seems acceptable for such a simple scaling and considering that errors of more complex simulations range from 5% to 15% [22, 33, 34, 162]. Additionally, it has to be taken into account that, due to the stochastic nature of the process, variability of melt pool dimensions can also occur along a single scan track or between multiple scan tracks with the same process parameters. Scime and Beuth [163] observed a relative scatter in melt pool depth of 4.5% to 37% for IN718 by measuring 10 cross sections with the same processing parameters over a wide range of process space. A comparable range of scatter for melt pool depth across measurements of different cross sections of the same scan track has been observed for this work. The standard deviation varied from 0.6% to 46% for the investigated alloys. Thus, the observed prediction error seems acceptable.

The herein proposed depth corrected dimensionless enthalpy H^*_{cd} is similar to the scaling used by Ye et al. [27] and Rubenchik et al. [26] for melt pool depth of low thermal diffusivity alloys. In contrast to their work, latent heat was included in calculating the necessary energy for melting in this work. In accordance with these previous studies, the current work shows the usability of H^*_{cd} to scale melt pool depth for different alloys. In addition, it was shown that the scaling can also be applied to high thermal diffusivity alloys, such as AlSi10Mg. The dimensionless enthalpy H^* has also been applied without inclusion of Pe, giving acceptable fits in previous investigations [28, 30, 56] despite wide ranges of investigated scan speeds [28], including speeds leading to $Pe < 1$ [30]. Within a small range of scan speed variation or in the case of very high scan speeds, neglecting the Pe dependence might be valid. However, it is not clear why data

within those observations did not scatter strongly despite the significant speed ranges tested. A large scatter of data for single tracks in keyhole mode welding is indeed acknowledged by King et al. [56]. Nevertheless, a further discussion in relation to scan speed has not been made. An alternate scaling for melt pool depth is given by Fabbro et al. [142] as

$$d^* = \frac{B_1 P}{u a^2 \rho c_p \Delta T} \frac{1}{1 + \frac{u_0}{u}} \quad \text{with} \quad u_0 = B_2 \frac{D}{a} \tag{4.6}$$

and constants B_1 and B_2 depending on the range of Pe. Within a Peclet number range[2] of $0.4 < Pe < 12$, they propose $B_1 = 0.4$ and $B_2 = 1.2$. At scan speeds much higher than the critical speed u_0, the term $1/(1 + u_0/u)$ reduces to 1 and Equation 4.6 results in a scaling of d^* similar to H^*_{cd}. For speeds smaller than u_0, dimensionless melt pool depth d^* decreases with decreasing scan speed which qualitatively agrees with the observed Pe dependence at small Pe numbers (see Section 4.1.2.1). However, the term u_0/u can be rearranged to

$$\frac{u_0}{u} = \frac{B_2 D}{a u} = \frac{B_2}{Pe} \tag{4.7}$$

showing that the ratio is dependent on Pe. Since B_2 is proposed to be constant within the aforementioned Pe range, the transition of Pe dependence should occur at similar Pe independent of material. However, material dependence was observed in this work which is not taken into account with the proposed scaling of Equation 4.6. In general, the presented results validate existing scaling laws and extend the applicability of H^*_{cd} to high thermal diffusivity alloys.

4.1.3.2 Dimensionless melt pool width

The proposed relation for dimensionless melt pool width is introduced as the width corrected dimensionless enthalpy H^*_{cw} and is defined by Equation 4.8.

$$H^*_{cw} = H^* Pe^{-0.2} \tag{4.8}$$

From the previous results on the relation of melt pool width and Pe, the proposed definition of H^*_{cw} is expected to be applicable for $Pe > 1$. The same data sets as for the evaluation of melt pool depth is used to plot dimensionless melt pool width w^* over H^*_{cw} (see Figure 4.14a). The data is fitted with a power law relation, resulting in $w^* = 3.154(1 - H^{*-0.54}_{cw})$, and the 95% prediction band is indicated as gray area. The corresponding relative prediction error is plotted in Figure 4.14b. As for dimensionless melt pool depth, a tendency for over-prediction of conduction mode samples is visible, however the maximum deviation is only -19% which is considerably lower compared to the melt pool depth prediction error. For keyhole mode samples there is a tendency for over-prediction of melt pool width for 316L and MS1, while IN718 and Ti64 show a tendency

[2] The Pe range was adapted to account for the different definition of Pe in [142] compared to this work.

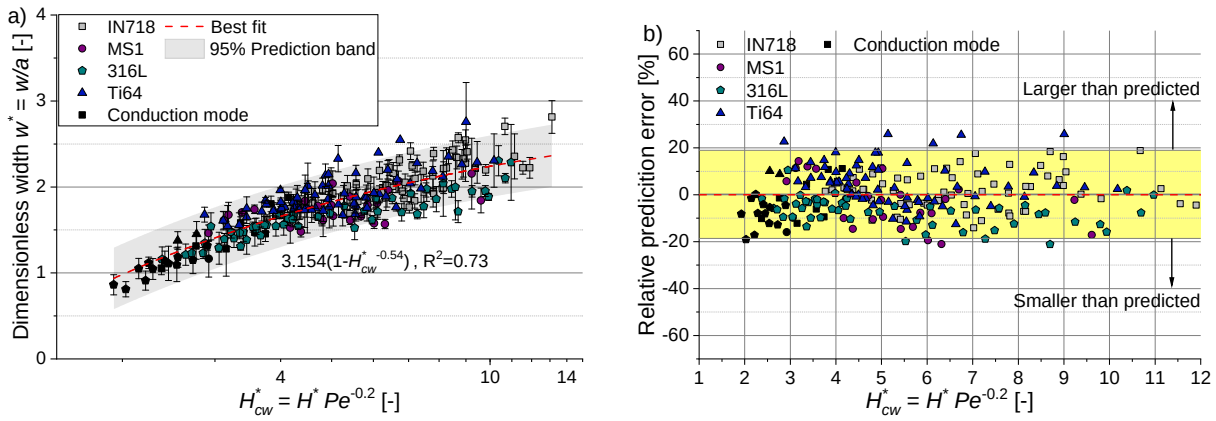

Figure 4.14: Prediction of dimensionless melt pool width w^* by width corrected dimensionless enthalpy H^*_{cw}; a) dimensionless width w^* over width corrected dimensionless enthalpy H^*_{cw} and b) corresponding error of measured means to predicted values; the yellow band indicates the error range for 95% of data

to be under-predicted. However, the overall scatter of 95% of the data is within $\pm$ 19%, which is almost a third lower than the 95%-error for melt pool depth. In accordance with results for melt pool depth, the prediction error is within an acceptable range in comparison to melt pool width deviations for more complex simulations of 2% to 18% [22, 33, 34]. Variation within scan tracks is also smaller as for melt pool depth for stable scan tracks, as width is less influenced directly by keyhole geometry and laser power absorption. Scime and Beuth [163] observed a relative scatter in melt pool width of 2.9% to 14% which is in good agreement with scatter observed in this work in the range of 0.8% to 29.9%.

To check the validity of the proposed scaling for another alloy not included in the fit, as for melt pool depth, AlSi10Mg data is used and is shown in Figure 4.15. In contrast to melt pool depth, AlSi10Mg data for both experimental setups, M290 and M400, clearly separates from the previous best fit result. Wider melt pools as expected are obtained for almost all process parameter combinations for AlSi10Mg. Thus, even with correction for Pe dependence, the dimensionless enthalpy H^* does not give a material independent scaling relation for melt pool width for materials with significantly different thermal properties. This can also be seen from Figure 4.9b and Figure 4.9d with AlSi10Mg obtaining higher dimensionless melt pool widths w^*, despite smaller H^* compared to the investigated steels, IN718, and Ti64. Furthermore, this observation is in accordance with results from Hann et al. [143] who found a deviation from scaling with H^* for different alloys. A consolidation of data was achieved by additional scaling dimensionless width w^* with thermal diffusivity for the respective alloy to take into account the effect of heat loss on melt pool width. However, with the definition of H^*_{cw}, conduction heat losses should already be included. While, within the keyhole welding regime, melt pool depth is mainly determined by keyhole depth, melt pool width depends on heat distribution around the keyhole, and thus is influenced by thermal diffusivity as well as phase transition temperatures. Since the keyhole diameter w_{KH} is defined by the boiling isotherm of the material and melt pool

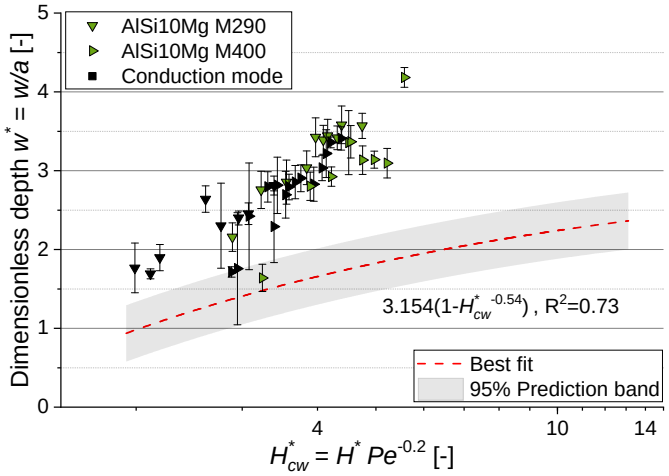

Figure 4.15: Comparison of AlSi10Mg data sets with best fit for dimensionless melt pool width w^* of Figure 4.14

width by the solidus isotherm, the ratio of w/w_{KH} should scale with $T_b/T_{solidus}$ as proposed by Dausinger [154] for high Pe. In case of AlSi10Mg, $T_b/T_{solidus}$ is 3.3, while for the investigated steels and Ti64 the ratio is 1.9. This explains that data falls close for those alloys in contrast to the higher melt pool widths (at similar H^*_{cw}) for AlSi10Mg observed in Figure 4.14a. The values of $T_b/T_{solidus}$ for all investigated alloys are given in Table 4.2. Since the keyhole diameter w_{KH} is related to the laser beam diameter a, the T_b/T_m scaling is expected to hold true also for dimensionless melt pool width w^*. Therefore, data for dimensionless melt pool width w^* was normalized by $T_b/T_{solidus}$ and replotted in Figure 4.16a. It can be seen that the replotted data falls close for all investigated alloys including AlSi10Mg and a new best fit is calculated as $1.439(1 - H^{*-0.65}_{cw})$. The corresponding relative prediction error is shown in Figure 4.16b. Compared to the previously proposed scaling for w^* in Figure 4.14, general trend and fit quality does not change significantly for IN718, MS1, 316L, and Ti64. There is still a tendency of over-prediction for 316L and under-prediction for Ti64, while IN718 and MS1 data is more scattered around zero.

The 95% data scatter for the new fit lies within $\pm$20%, with some outliers in conduction mode on the lower side and Ti64 in keyhole mode on the upper side (maximum error of 33%). Most of the AlSi10Mg data falls within the 95% prediction band with the majority of the data points accumulating within the positive error side, indicating a tendency for under-prediction. There is no significant difference observable between the M290 and M400 experiments. Thus, it can be concluded that with the normalization of $w^*T_{solidus}/T_b$, melt pool widths can be predicted for different materials within an acceptable error range.

Table 4.2: Ratio of $T_b/T_{solidus}$ for investigated alloys; T_b and $T_{solidus}$ were taken from Table 4.1 and Table 3.2

	IN718	MS1	316L	Ti64	AlSi10Mg
$T_b/T_{solidus}$	2.1	1.9	1.9	1.9	3.3

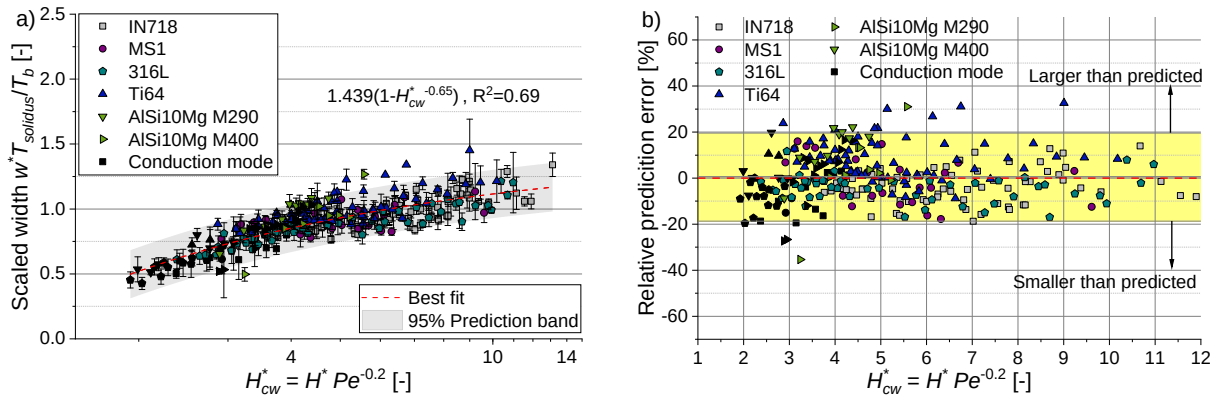

Figure 4.16: Width corrected dimensionless enthalpy H^*_{cw} versus scaled width $w^*T_{solidus}/T_b$; a) prediction of melt pool width and b) corresponding error of mean values from predicted mean; the yellow band indicates the error interval for 95% of data

Compared to melt pool depth, not much attention has been spent on investigating dimensionless scaling laws for melt pool width prediction in LPBF. Nevertheless, the knowledge of melt pool width is important concerning geometrical accuracy of parts, especially for thin walled geometries and lattice structures. Furthermore, melt pool width determines the range of applicable hatch distances to ensure sufficient connection between consecutive scan tracks and to avoid overheating. A dimensionless scaling relation for melt pool width has also been developed and validated for six different alloys by Großmann et al. [25] using a Peclet number based on melt pool width and specific power. Although their proposed scaling proofed high fit quality and applicability, the proposed model within this work has some benefit when comparing different machine systems, as it includes the laser beam diameter as another important process variable beside P and u.

4.2 Characterization of process window

4.2.1 Prediction of process window

In Section 4.1.3, a model was proposed which scales dimensionless melt pool depth d^* by the depth corrected dimensionless enthalpy H^*_{cd} . Since parts are built in LPBF track by track and layer by layer, single scan lines must have sufficient overlap with their neighboring and underlying material. With decreasing melt pool depth, single scan tracks become prone to balling instability due to the reduced contact area with the underlying substrate (see Section 2.2.2). However, very deep and narrow melt pools are susceptible to formation of keyhole porosity (see Section 2.2.1). Thus, it can be expected that process window boundaries can be related to specific melt pool depth limits which in turn are scaled by H^*_{cd} as shown previously. Therefore, it is proposed that a common range of values for H^*_{cd} resulting in stable and pore free single scan tracks can be found.

To illustrate the combinations of process parameters resulting in stable and defect free single scan tracks, data of the investigated parameter combinations and corresponding track quality labels for IN718 are exemplarily plotted in a typical scan speed versus laser power process map in Figure 4.17a. Process maps for the other investigated alloys are given in Appendix A.2. To indicate line quality, single scan tracks are labeled as either stable, meaning that no keyhole porosity was visible in the metallographic cross sections and surface profile measurements did not show any dips down to $20\,\mu\mathrm{m}$ from the substrate plane, or instable if the aforementioned criteria were not met. To have a conservative estimate for the process window, the label instable was given if any of the four cross sections contained a keyhole pore or any of the two surface line profiles contained a respective drop. Additionally, lines of constant H^*_{cd} at 1.5 and 4 are indicated in the graph to illustrate the P/u scaling for H^*_{cd}. Since it was shown in Section 4.1.3.1 that melt pool depth can be related to H^*_{cd}, these lines indicate process parameter combinations of similar melt pool depths. The lines would shift depending on beam diameter as a third process parameter. However, all of the presented experiments were done on an EOS M290 systems, which has a nominal beam diameter of $80\,\mu\mathrm{m}$. Since laser beam size variation between and within machines should fall within $\pm 5\%$, the respective slopes for H^*_{cd} were additionally calculated for those minimum and maximum values. This is indicated by the yellow areas around the dashed lines. Figure 4.17a shows a clear separation for most data points into regions with stable lines (Figure 4.17c) surrounded by unstable lines (Figure 4.17b and d), which define the process window.

The upper scan speed boundary is determined by melting depth decreasing to a point were single scan lines become prone to balling instabilities and start to form neckings along the scan length as a preform to balling (see Figure 4.17b). The boundary between stable and instable lines seems to follow a positive linear correlation between laser power and scan speed such that with increasing laser power, a higher scan speed can be applied before the single scan track becomes instable. The trend of the balling limit does not continue above a certain scan speed value, marked with a

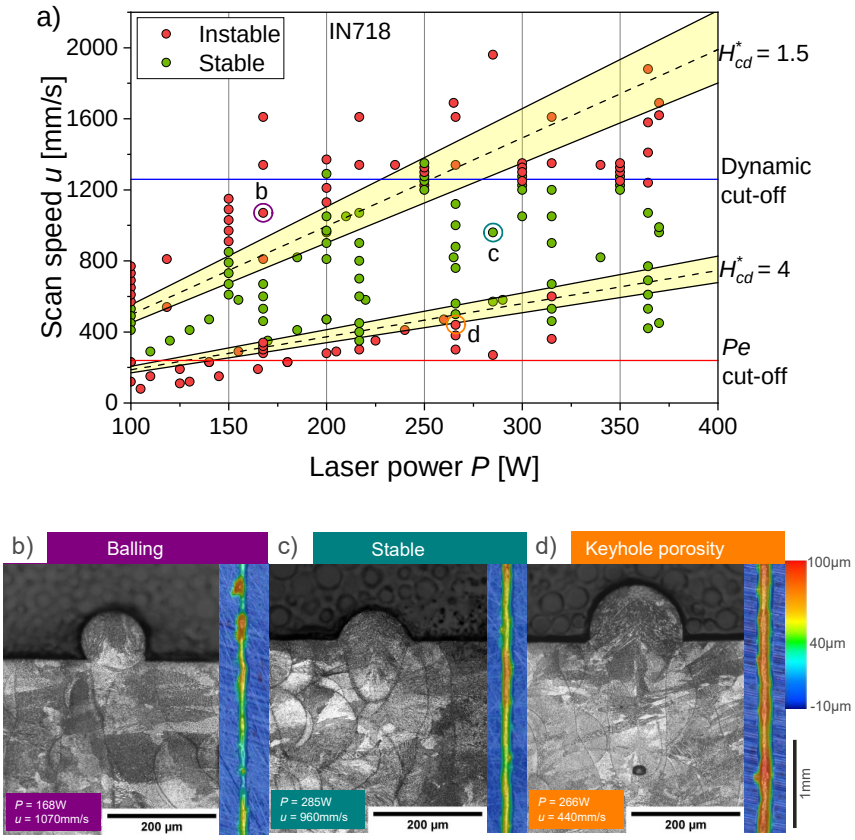

Figure 4.17: a) Experimental single scan track process map u over P for IN718 with examples of scan track b) with balling defect, c) without any defects, and d) deep keyhole melt pool with keyhole porosity

blue horizontal line that is denoted as dynamic cut-off. Despite an increase in laser power, stable scan lines were not achieved in this region due to increased melt pool dynamics resulting in the so called humping phenomenon. A deeper discussion of this dynamic cut-off will be given in Section 4.2.3. Here it should only be noted that a formulation of the balling limit in terms of H^*_{cd} is only valid below the dynamic cut-off.

The lower scan speed limit is determined by formation of keyhole porosity at high energy input as illustrated in Figure 4.17d. As introduced in Section 2.2.1, keyhole porosity is known to form due to the collapse of the front and back keyhole wall, pinching off a part of the vapor cavity. Thus, keyholes with a high aspect ratio, meaning narrow and deep keyholes, are especially susceptible to formation of keyhole pores [87]. A critical keyhole front wall angle of 77° is proposed by Cunningham [87] to characterize keyholes prone to pore formation. The front wall angle can be calculated from the ratio of beam diameter and keyhole penetration depth by a simple geometric relation $\tan\Theta = d/a = d^*$, schematically drawn in Figure 4.18. This relation assumes that the laser beam fully impinges on the front wall and neglects angular dependence of absorption [78]. Thus, a constant critical front wall angle for onset of keyhole porosity, as proposed by Cunningham [87], would mean that there exists a constant critical dimensionless melt pool depth. Based on this, a critical H^*_{cd} should exist as well. In contrast, observations from

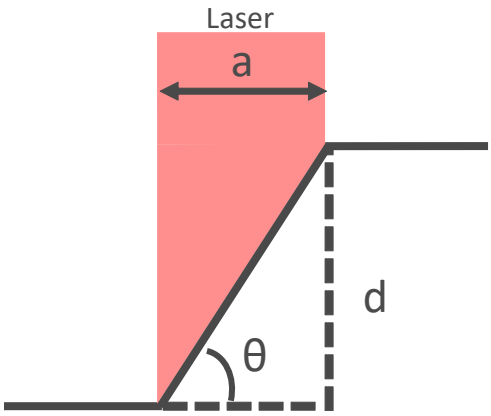

Figure 4.18: Schematic showing relation of keyhole front wall angle Θ with keyhole depth d and laser beam diameter a, based on [78]

Zhao et al. [81] indicate that critical melt pool depth varies with process parameters such that critical depth increases with increasing scan speed and power. Such a relation would result in a curved boundary in the P-u process map. In terms of the process map in Figure 4.17, this would mean that in the high power region (lower right corner) the slope of the keyhole boundary should be more flat compared to the lower power region (lower left corner). Indeed, keyhole porosity was less likely observed for samples in the high power and low scan speed region ($P > 300\,\mathrm{W}$), which indicates that a linearly increasing boundary might not be a correct representation of the keyhole porosity limit. However, only four cross sections were evaluated for each data point and an existing keyhole porosity might not have been captured within those cuts. Therefore, a linear boundary, respectively constant melt pool depth and H^*_{cd}, is proposed within this work. This approach also gives a more conservative estimate of the process window, as it would predict keyhole porosity to already occur at higher speeds in the high power region. Additionally, the Pe cut-off is indicated as horizontal red line, which is calculated with a minimum beam diameter of $76\,\mu\mathrm{m}$. This value for the beam diameter represents the smallest beam diameter within the $\pm 5\%$ measurement uncertainty from the nominal value, giving the highest scan speed for a specific Pe value. Thus, it represents a conservative estimate of the Pe cut-off speed. Although process parameter combinations with scan speeds below this limit can result in stable scan tracks, it has been shown in Section 4.1.2 that the scaling of H^*_{cd} with melt pool depth is not valid for those low scan speeds, and therefore a prediction of the process window based on H^*_{cd} cannot be given.

To evaluate if H^*_{cd} can be used to characterize the upper and lower process boundaries, data from the process maps is fit with binary logistic regressions for each process boundary. Since the scaling with H^*_{cd} is only valid within the Pe and dynamic cut-off, data with scan speeds higher as the respective dynamic cut-off velocities (see Section 4.2.3) and $Pe < 4$ is excluded. For AlSi10Mg, the Pe limit is set to $Pe = 1.8$ and no dynamic cut-off limit is applied since a critical humping velocity could not conclusively be determined. The corresponding characterization of single scan tracks as stable or instable over H^*_{cd} and respective binary logistic regression fits for the investigated alloys are shown in Figure 4.19 (a summary of the resulting equations

from the binary logistic regression fits is given in Appendix A.3). To obtain the lower process boundary for energy input, the data sets were divided into instable scan tracks due to balling, and stable scan tracks including parameter combinations with keyhole porosity resulting in the left side regression fits. The opposite was done for the upper process boundary estimations, where balling samples were grouped together with stable scan lines against samples containing keyhole porosity (right side regression fits). For AlSi10Mg, only the left side regression line corresponding to the balling boundary was fit since the investigated data set contained only one sample with a possible keyhole porosity. Due to the stochastic nature of the process and since only two single scan lines with four cross sectional cuts were investigated for each parameter combination, the process window for the investigated alloys is defined with a probability of 90% for a stable line result. A lower probability might as well be suitable to result in defect free parts since defects in single scan tracks might be healed within three dimensional parts by remelting of neighboring and underlying scan lines [164]. In this regard, it would be interesting to correlate the single track probability for line stability to quality attributes of a final part, such as porosity or surface roughness, in future work. However, as a conservative estimate, the 90% probability is chosen to define the process windows within this work. In addition, the 50% probability range for stable and defect free lines is indicated to illustrate the spread in H^*_{cd} between the 50% and 90% probability for each boundary.

For the investigated steels, IN718, and Ti64, the fit process boundary values are quite similar with no specific trend between the investigated alloys. The lower process boundary ranges from H^*_{cd} of 1.8 for IN718 to 2.3 for 316L with a corresponding lower critical dimensionless melt pool depth d^*_l of 1.1 to 1.5, which would correspond to $32\,\mu\mathrm{m}$ difference in dimensional form for $a = 80\,\mu\mathrm{m}$. Due to the steep slopes for the binary regression fits of the lower process boundary, the difference in H^*_{cd} for 50% to 90% probability is quiet small with a maximum of 0.7 for 316L and Ti64. This indicates that there exists a defined and sharp transition between stable and instable lines for the lower energy input for those alloys. For the upper boundary of the process window, the values of H^*_{cd} at 90% probability are more scattered, ranging from 3.1 to 5.0. Additionally, the slopes of logistic regression fits are shallower compared to the fits for the lower process boundary. The maximum difference between 50% and 90% probability is 1.9 for 316L and Ti64. The shallow slopes can be explained, as only a minor fraction of the total samples were observed to obtain keyhole porosity (only 2 samples in MS1 and 316L). Additionally, there is no clear separation between regions of H^*_{cd} containing only samples with keyhole porosity and without porosity (especially for Ti64), thereby smoothing the upper transition boundary. The observed occurrence of stable single scan tracks even at higher H^*_{cd} might be a result of the sampling strategy and not correctly represent the actual defect structure within the single scan tracks. Since only four cross sections had been investigated for each parameter set, it might be that keyhole porosity existing along the scan track length has not been captured within those cuts. To capture the defect structure within the whole length of the scan tracks, volumetric analysis methods like computer tomography would be necessary. However, those methods are time and

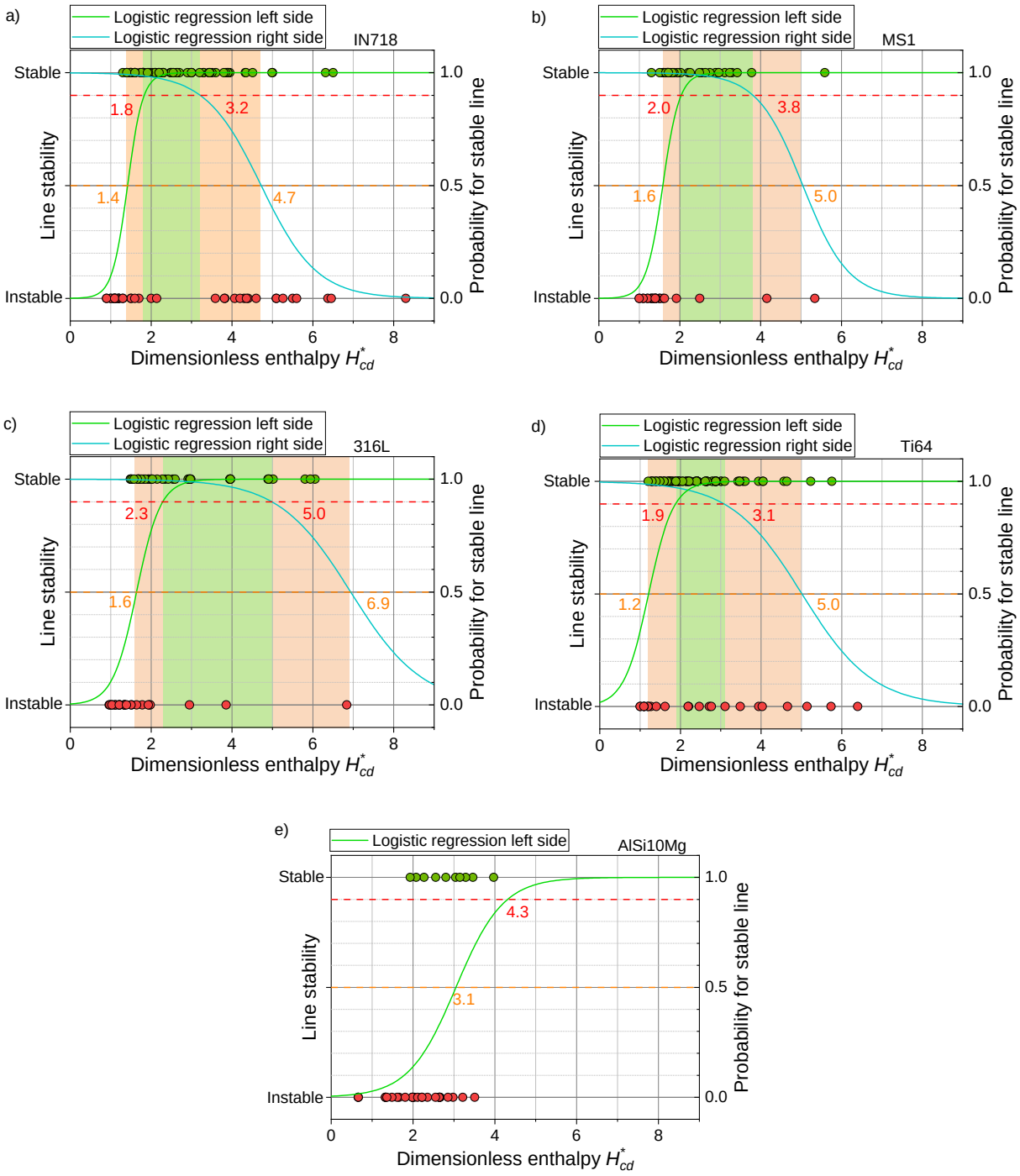

Figure 4.19: Process boundary characterization of single scan tracks over H^*_{cd} by binary logistic regression fits for a) IN718, b) MS1, c) 316L, d) Ti64, and e) AlSi10Mg; the red and orange lines indicate 90% and 50% probability for producing a stable and defect free single scan track

cost intensive and have specific requirements for sample preparation. Therefore, they cannot be effectively employed for a large sample set. To give an indication for the validity of the upper process boundary to prevent keyhole porosity, the critical front wall angle with the boundary condition of this work is compared with the one proposed by Cunningham et al. [87]. With H^*_{cd} between 3.1 to 5.0, the critical upper melt pool depth is calculated to lie within $d^*_u = 2.1$ to 3.7, which would correspond to front keyhole wall angles of $65°$ to $75°$ according to Figure 4.18. Those values are slightly lower than the $77°$ proposed by Cunningham et al. [87] and can be seen as conservative estimates. Some surface instability and keyhole porosity is also observed to occur within the proposed process windows which could result from the stochastic nature of the process. For example powder or spatter particles blown out during the process could interact and shield the laser beam while passing through it, thus changing the local energy input [69, 73]. Furthermore, although the samples were built to achieve the least impact on following scan tracks, spatter particles and blown powder could also agglomerate at certain locations on the powder bed and influence the amount of molten material locally [69, 73]. Despite those local effects, overall a common process window of $2.1 < H^*_{cd} < 3.4$ is proposed for the investigated steels and Ti64. The corresponding equations for the binary logistic regression fits of the lower and upper boundary over all data sets (except AlSi10Mg) is also given within the summary in Appendix A.3. This process window range is only valid for scan speeds within both the dynamic as well as the Pe cut-off.

Contrasting results are observed for AlSi10Mg as shown in Figure 4.19e. An upper process boundary could not be determined with the investigated process parameter combinations as only one single scan track contained a visible keyhole pore at $Pe > 1.8$ and this process parameter combination resulted in $H^*_{cd} = 3.3$. As this would mean that the boundary for keyhole porosity would lie below the boundary for balling, the observed keyhole pore formation for this parameter combination is expected to be an outlier. The lack of keyhole porosity observations within the AlSi10Mg samples, in comparison to IN718 and Ti64, might be explained by the lower range of investigated H_{cd} values. In fact, due to the low absorptivity and high thermal diffusivity, a laser power of $P > 466\,\mathrm{W}$ is necessary to achieve $H^*_{cd} = 5.0$ at $Pe > 1.8$, which is only capable with the M400 system with a $1\,\mathrm{kW}$ laser. As machine availability with this system was limited, no experiments explicitly investigating the high energy input region for AlSi10Mg were done in this work. The lower process boundary is considerably higher than for the other investigated alloys, with even the 50% probability limit exceeding the highest proposed balling boundary value of $H^*_{cd} = 2.3$ for 316L. In addition, the slope of the regression fit is shallower compared to the other alloys meaning that the transition to line instability is less defined for AlSi10Mg. The observed difference in process window boundaries for AlSi10Mg and the other investigated alloys was not expected, as a similar dependence of dimensionless melt pool depth on H^*_{cd} was observed in Section 4.1.3.1. To explain the deviation in behavior for AlSi10Mg, melt pool morphologies and track topographies were evaluated for single scan tracks processed at different parameter combinations. An excerpt showing part of the process map for AlSi10Mg

with corresponding micrographs and topographic images for selected instable single scan tracks is given in Figure 4.20a (the full process map is shown in Figure A.3d). Only M290 experiments are included in the process map. For the standard investigated powder layer thickness of $190\,\mu m$, it can be seen that only a few single scan tracks formed stable lines while most of the parameter combinations showed surface instabilities. Parameter combinations at low H^*_{cd}, corresponding to high scan speeds and low laser power, show typical balling behavior with discontinuities and agglomerates along the scan track and low melting depths within the cross sectional micrographs, as exemplarily shown in Figure 4.20b. With a decrease of scan speed, deeper melt pools with a good connection to the underlying substrate are achieved (Figure 4.20c and d). However, those single scan tracks still contain neckings with highs and troughs along the length of the scan track. Even a large hole is observed along the scan track in Figure 4.20c, as indicated by the red square. Instability would not have been expected from the micrographs of those single scan tracks since melt pools are quite deep and show a low contact angle ψ. There is a slight tendency for material agglomeration at the center of the melt pool for those two scan tracks which could indicate instability related to the humping phenomenon. Furthermore, undercuts are visible within the topographic images as indicated by red arrows. At those locations, the melt pool

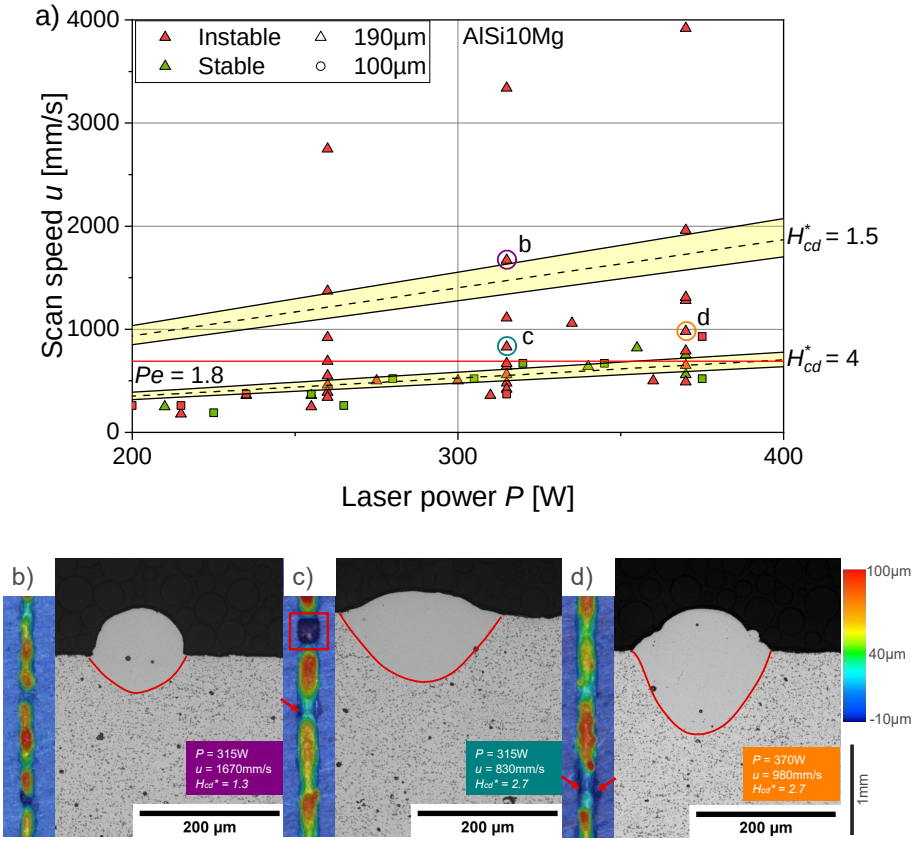

Figure 4.20: a) Excerpt of the AlSi10Mg process map for $190\,\mu m$ and $100\,\mu m$ layer thickness experiments with cross sectional micrographs and topographic images of selected instable single scan tracks in b), c), and d)

surface is lower as the substrate surface and the melt pool forms a thin metal strip in the scan track center. Thus, the occurrence of humping within the selected process speed range could be a possible explanation for single scan track instability of AlSi10Mg. A deeper discussion about the humping phenomenon observed for the investigated alloys will be given in Section 4.2.3. To exclude a powder layer thickness related effect, experiments were repeated with a reduced layer thickness of $100\,\mu\mathrm{m}$ This value was chosen since it corresponds to the effective powder layer thickness of the AlSi10Mg M290 standard process with $30\,\mu\mathrm{m}$ nominal thickness (Appendix A.1). Similarly to previous results, stable single scan tracks could not be achieved with the chosen parameter combinations. Thus, instability due to the high powder layer thickness used for the initial experiments can be excluded as an explanation. To fully understand the deviation of AlSi10Mg from the proposed process window, further investigations should focus on the use of high power systems to enable extension of the experiments to the high H_{cd} region as well as on HS imaging of the melt pool dynamics at different process parameter combinations. The exceptional behavior of AlSi10Mg additionally depicts the importance in understanding the interaction between different physical phenomena in LPBF, and therefrom resulting limitations for the applicability of specific scaling laws.

4.2.2 Peclet limit

The influence of Pe on melt pool dimensions has already been discussed and possible physical explanations have been proposed in Section 4.1.2.1. Therefore, within this section, the Pe limit will be viewed in context of process efficiency and industrial relevance. The previously suggested process window range for H^*_{cd} is only valid for process parameter combinations with scan speeds higher than the Pe cut-off. Below this limit a conclusive correlation for melt pool depth and H^* could not be found over the investigated alloys. Stable and defect free single scan tracks can still be achieved below this scan speed limit, and thus the Pe cut-off reduces the process parameter space that might actually be available. However, taking into account that the Pe limit is attributed to low scan speeds for common laser beam sizes (see Table 4.3) its introduction does not severely intersect the industrial relevant process space with scan speeds around $1\,\mathrm{m/s}$. Exempt from this are the high thermal diffusivity alloys, such as AlSi10Mg, for which the Pe cut-off speeds are in a relevant range.

From the perspective of process efficiency, scan speeds resulting in Pe close to the transition value should be preferred, as the maximum melt pool depth for constant H^* is reached at this point. At lower scan speeds the process efficiency decreases since energy is lost to heat

Table 4.3: Pe cut-off velocities for the investigated alloys calculated with beam diameter $a = 76\,\mu\mathrm{m}$

	IN718	MS1	316L	Ti64	AlSi10Mg
Scan speed $[\mathrm{mm/s}]$	239	304	288	413	689

the surrounding material during the long interaction time of the laser beam with the material. However, process efficiency also decreases with increase in Pe above the Pe limit, as melt pool dimensions decrease. For $Pe > 15$ this decrease saturates and melt pool dimensions do not strongly vary anymore with Pe number (see Figure 4.9). Thus, process efficiency does no longer decrease. From an industrial perspective this region should be preferred due to the high scan speeds reducing build time at saturated efficiency. In fact, for the low thermal diffusivity alloys, the standard InFill speeds on an EOS M290 result in Pe ranging from 12 to 17. Of course, it has to be taken into account that melt pool depth should be sufficient to connect to the underlying substrate and prevent balling defects. Processing at slower scan speeds, meaning at lower Peclet number, could thus be required when enhancing built rate by increasing layer thickness or hatch distance.

4.2.3 Humping limit

From the IN718 process map in Figure 4.17, it was observed that there exists a specific scan velocity above which stable lines could not be achieved independent of laser power. This specific velocity was called dynamic cut-off limit since the observed instability can be related to humping caused by the movement of the melt pool. Humping is a well known phenomenon not only in laser, but also arc and electron beam welding at high velocities. In the following, only a brief review of hump formation will be given and the reader is referred to Section 2.2.3 for an in depth description. In keyhole mode welding at high velocity, the molten material is forced to flow around the keyhole rim, resulting in a high velocity inside the central part of the melt behind the keyhole [107, 108, 110]. This high velocity band of molten material is prone to the Plateau-Rayleigh instability, creating neckings and corresponding swellings along the melt band to decrease free surface energy. In addition, the solidification front at the back of the melt pool acts as a ramp for the incoming high velocity melt which is pushed against it and bulges upwards [84, 110]. Those two mechanisms in combination are supposed to form the periodic agglomerates of material which are referred to as humps. Another characteristic of humping phenomenon besides the humps themselves is the formation of undercuts within the necked regions, which are created by the high velocity central melt jet behind the keyhole [107]. Within this subsection, it will first be shown that the humping phenomenon presents a reasonable explanation for the observed dynamic cut-off limit. Secondly, the influence of material properties on the value for the cut-off speed will be discussed.

Examples of topographic images and cross section micrographs for single scan tracks built at speeds above the humping limit for the respective alloys are shown in Figure 4.21. It is visible from the topographic images that scan lines consist of hills and valleys with some of those valleys even obtaining negative height values, meaning that the scan line surface at those locations is below the substrate surface. Thus, it can clearly be seen that those scan lines are instable. The scan tracks for MS1 show the least humps which can be attributed to the applied scan speed,

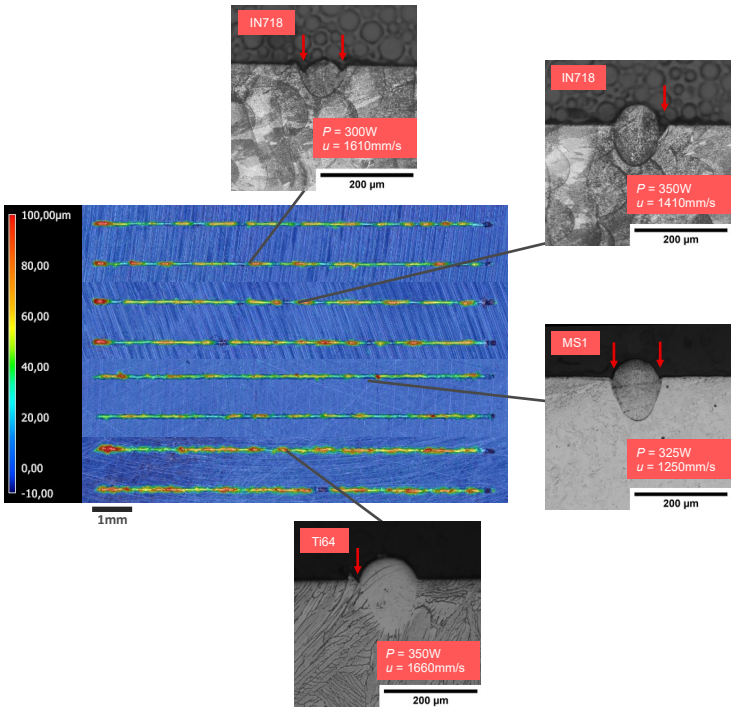

Figure 4.21: Topographic images and corresponding cross section micrographs for different investigated materials with parameter combinations above the humping limit; red arrows mark undercuts

which was close to the estimated critical scan speed as will be discussed in the next paragraph. In contrast to welding investigations [101, 102, 104], there is no periodicity observed for humping of single scan tracks in this work. Nevertheless, this does not exclude humping as the underlying mechanism, since also stochastic appearance of humping was observed in microwelding [105], which is closer to the presented experimental conditions than welding experiments. Additionally, the powder layer might contribute to the irregular appearance of humps for LPBF single scan tracks. With results only from the topographic images, it is difficult to distinguish between the humping and the balling phenomenon (see Figure 4.17b for balling topography), as both result in necking of the scan lines at certain locations. In the extreme case of balling, such that single unconnected agglomerates are formed on top of the substrate, it might be possible to distinguish between balling and humping by topography only. However, taking into account the cross sections of the respective single scan tracks, it is clear that the observed instability is not related to balling, as there exists sufficient melt pool penetration within the substrate. Furthermore, undercuts are visible within the cross sections marked by red arrows. The observed single scan track instabilities above the dynamic cut-off are attributed to humping since they show all characteristics: 1. samples are in kehyole mode welding, 2. hump formation, which only appears at high scan speeds, and 3. undercuts at melt pool boundaries.

The critical scan speed for the onset of humping u_{hump} varies with laser power and beam diameter [106]. However, as laser beam diameter was nominally constant and no steep slope of humping boundary is expected from the data within the process maps, the critical scan speed is taken as constant for the following investigations. To estimate the critical scan speed u_{hump},

selected subsets of data from IN718, MS1, and Ti64 were fit by binary logistic regressions. Subset selection was made so that only data relevant to humping was included, which meant $u >$ $700\,\mathrm{mm/s}$ and $P \geq 225\,\mathrm{W}$ for IN718 (total of 51 data points), $u > 500\,\mathrm{mm/s}$ and $P \geq 275\,\mathrm{W}$ for MS1 (total of 45 data points), and $u > 1100\,\mathrm{mm/s}$ and $P \geq 225\,\mathrm{W}$ for Ti64 (total of 54 data points). Those three alloys were chosen to illustrate the influence of material properties since thermophysical data for IN718 and MS1 are close, while distinctly different from Ti64 (see Table 3.2). A comparison of the corresponding logistic regression curves is shown in Figure 4.22. The dynamic cut-off velocity is calculated at a probability of line instability of 50%, which is marked by the red horizontal line. As expected, for IN718 and MS1 u_{hump} is quite close, while a higher limiting scan speed is calculated for Ti64. Compared to IN718 and Ti64, the logistic regression fit for MS1 has a shallow slope leading to a wide scan speed range were neither humping nor line stability can be predicted with certainty. This is a result of the low amount of data points in the very high and very low scan speed regions, far away from the humping limit, compared to Ti64 and IN718. Therefore, the uncertainty is increased in those regions. However, investigation of further process combinations with scan speeds in the missing regions is only expected to influence the slope of the binary logistic regression, but should not significantly shift the 50% probability value. It is stated that humping onset is determined mainly by melt viscosity η, surface tension σ, and the size of the melt pool around the keyhole [106, 110]. A high temperature difference between boiling and solidus temperature increases the rim width between the melt pool boundary and keyhole, thus reducing the melt flow velocity. Furthermore, a high melt viscosity enhances the force needed for movement and also reduces melt flow velocity. Therefore, the slightly lower humping onset velocity calculated for MS1 compared to IN718 can be explained by lower $T_b/T_{solidus}$ ratio and η (Table 3.2 and Table 4.2). Despite comparable (or in case of IN718, slightly lower) $T_b/T_{solidus}$ and lower viscosity, Ti64 has the lowest σ compared to IN718 and MS1. This possibly explains the increased humping onset speed. For the other two investigated alloys within this work, 316L and AlSi10Mg, separate data sets to investigate

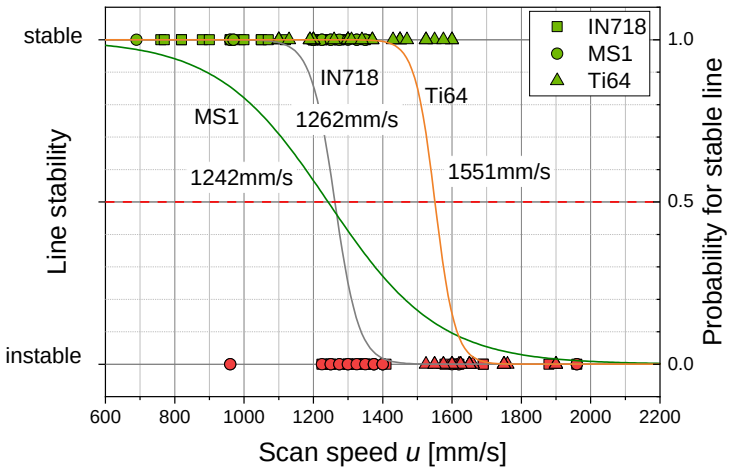

Figure 4.22: Line stability over scan speed u with binary logistic regression fits to compare u_{hump} for IN718, MS1, and Ti64

the humping limit have not been collected. However, from the existing data for 316L, 23 data points ($u > 600\,\mathrm{mm/s}$ and $P \geq 250\,\mathrm{W}$) can be selected for evaluation of the humping onset, resulting in a calculated u_{hump} of $1227\,\mathrm{mm/s}$. This critical velocity is comparable to IN718 and MS1 which was expected due to the similarity in material properties. Furthermore, it is in accordance with the observation of humping for $u \geq 1.2\,\mathrm{m/s}$ by Tang et al. [110] for 316L at comparable power range and beam diameter. Since only few data points were evaluated for 316L, the humping limit was set to $1200\,\mathrm{mm/s}$ to give a conservative estimate in the selection of data for Section 4.1.3.

Concerning AlSi10Mg, low melt viscosity is counterbalanced by its significantly lower surface tension, half of that for Ti64, and high $T_b/T_{solidus}$, creating wide melt pools. Therefore, AlSi10Mg is expected to result in the highest onset speed for humping compared to Ti64 and the steels as proposed also by Patschger et al. [106]. However, u_{hump} could not be determined with data from AlSi10Mg experiments, since no clear boundary between stable and instable single scan tracks was observed within the P-u map (Figure 4.23a). As discussed in Section 4.2.1, a process window was not found and even at low speed ($u < 1000\,\mathrm{mm/s}$) instable scan tracks showed characteristics of humping (Figure 4.20). A cross sectional micrograph and corresponding topographic image for this low speed region I is shown in Figure 4.23b. With further increase

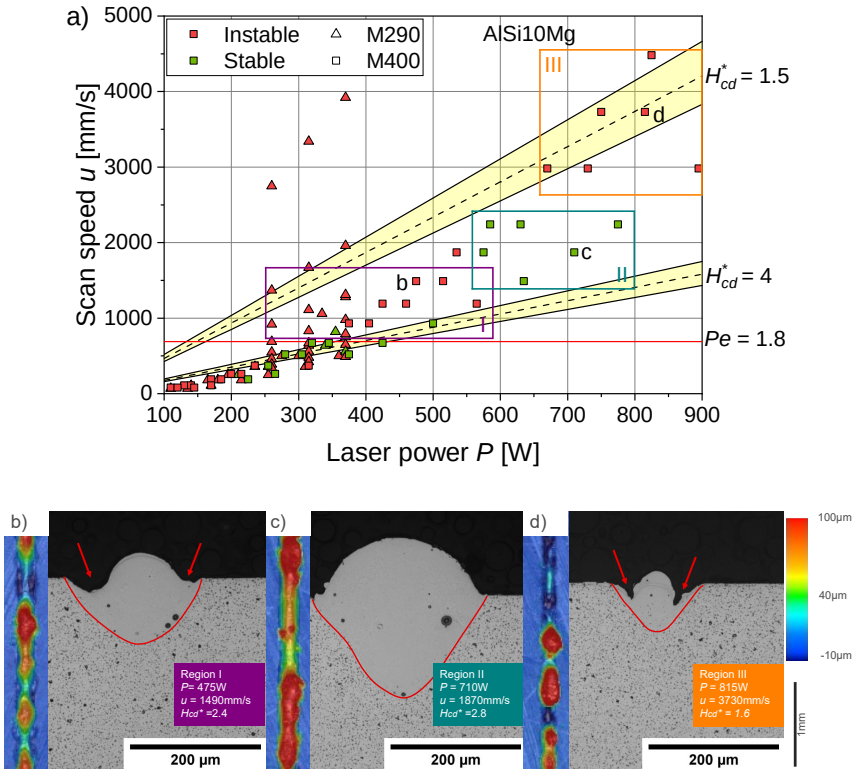

Figure 4.23: a) Process map for AlSi10Mg with processing regions I-III corresponding to first humping, stable scan track, and second humping region; corresponding micrographs and topographic images for scan tracks within the three regions given in b), c), and d); red arrows indicate undercuts

in laser power and scan speed, a region of stable lines is observed (region II and Figure 4.23c). Although, one has to note that those lines still show highs and troughs, despite being rates as stable with the applied stability criterion (see Section 3.3.3). Humping sets in again with increased scan velocity in region III as shown by the strong undercut formation within the sample cross section in Figure 4.23d. Thus, there seems to be a lower and upper humping region within the process map, with upper humping velocity between $2240\,\mathrm{mm/s}$ to $2980\,\mathrm{mm/s}$. It is not clear why there are two humping limits and process parameter combinations in the transition regions should be investigated in more detail.

Knowledge of the onset scan velocity for humping u_{hump} is of great importance in an industrial context, as it defines the upper process velocity and limits achievable build rates. An estimate of u_{hump} based on material properties, such as η, σ, and $T_b/T_{solidus}$, as well as processing conditions, would therefore be of great interest. Although the trend in u_{hump} for Ti64 and the investigated steels could be related with their respective thermophysical properties, alloys with a wider range of the mentioned influential properties should be investigated to develop dimensionless numbers, which characterize the humping behavior. Furthermore, process parameters influencing the melt pool dynamics, such as beam diameter and shape, should be taken into account. Indeed, for a given material, u_{hump} was observed to increase with increasing beam diameter at constant power [106] and an elongated beam source was recommended by Beck et al. [108] to reduce hump formation. Moreover, defocusing of the laser beam above the material plane and wobbling the laser along its scan path gave considerable reduction in hump formation for bead-on-plate laser welds [166]. Such techniques from laser welding might also be applied in LPBF to increase critical humping speed and productivity. Additionally, the influence of parameters unique to LPBF, such as powder layer thickness and the attachment of neighboring scan tracks to each other, has to be evaluated to understand hump formation in LPBF and prevent its occurrence.

4.2.4 Influence of powder layer thickness

In LPBF, three dimensional parts are built via consolidating powder layer upon powder layer. Thus, the selection of powder layer thickness significantly influences build time, energy input, powder waste, and geometrical accuracy of the part. A high powder layer thickness is preferred in terms of built time as less layers are needed to build a part of similar height, and thus recoating time is reduced [167, 168]. However, geometrical accuracy of the part might be diminished due to the staircase effect especially on curved surfaces, such as domes or rounded edges. While the two aforementioned criteria are readily taken into account when selecting nominal layer thickness, the influence on powder waste is often overlooked. However, a change in nominal powder layer thickness can significantly influence the amount of powder used for consolidation versus the amount of powder lost during the process [169]. Furthermore, with an increase in powder layer thickness, an increasing amount of energy is spent to melt the powder layer, resulting in a decrease in melt pool depth. Since the two characteristic process window

boundaries, balling and keyhole boundary, were attributed to specific melt pool depths, a change in melt pool depth by variation of layer thickness should influence the process window as well. In consequence, the proposed dimensionless process window of $2.1 < H^*_{cd} < 3.4$ only applies to a powder layer thickness of $190\,\mu\mathrm{m}$ that was used in the experiments. Therefore, in this section, a method is proposed to approximate the shift in process window with layer thickness variation. Experimental results will be given for IN718.

As a rough approximation, the melt pool will be viewed as a rectangle of width w and total depth d_t, which is composed of depth d and height h (Figure 4.24a). Although width and shape of the melt pool will vary with layer thickness, both will be approximated as constant here, so that $w_1 = w_2$ and $d_{t1} = d_{t2}$ at constant process parameters. Thus, variation of the layer thickness changes the fraction of height and depth of d_t but not d_t itself. Therefore, with Equation 4.9, dimensionless melt pool depth for layer thickness 2 can be calculated from the knowledge of the dimensionless depth and height from layer thickness 1 and dimensionless height of a single track built with layer thickness 2.

$$d^*_2 = d^*_1 + (h^*_1 - h^*_2) \tag{4.9}$$

When building parts in the saturated state, meaning that the effective layer thickness has stabilized, the consolidated material for each layer should obtain a height equal to the nominal layer thickness l_t. Thus, for a scan line within a group of hatches the track height should correspond

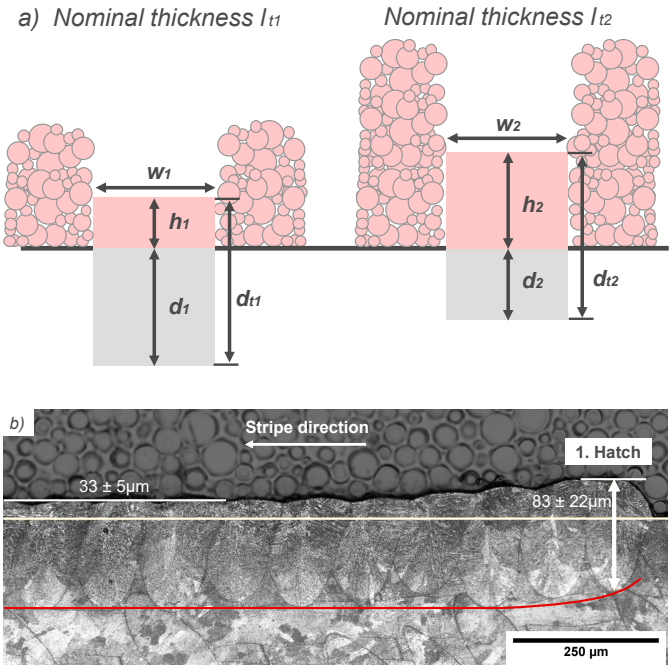

Figure 4.24: Influence of powder supply on melt pool depth and height; a) schematic of single scan tracks built with different nominal layer thicknesses $l_{t1} < l_{t2}$ and b) micrograph of first 10 hatches from IN718 hatch package built with $190\,\mu\mathrm{m}$ applied powder layer

on average to the nominal layer thickness and $h_1 = l_{t1}$ as well as $h_2 = l_{t2}$. However, single scan tracks behave differently from tracks within a hatch package since powder is supplied from both sides of the scan track. Scan track height is therefore higher for the first scan track and decreases until it reaches a stable height with increasing number of consecutive hatches. This trend is shown in Figure 4.24b for the first 10 hatches within a hatch package. The measured average height for the first hatch as well as for stable hatches from two cross sections are given. It can be seen that the average height for the stable hatches is only slightly lower than the corresponding nominal layer thickness of $40\,\mu\mathrm{m}$ and that the height for the first scan track is about two times this nominal height. Thus, melt height for the first hatch can be approximated as $h_i = 2l_{ti}$. Dimensionless melt pool depth d_1^* can also be substituted since dimensionless melt pool depth was estimated in dependence of H_{cd}^* (see Section 4.1.3.1), resulting in Equation 4.10 for single scan tracks.

$$d_2^* = 0.559 H_{cd}^{*1.17} + 2(l_{t1}^* - l_{t2}^*) \tag{4.10}$$

Furthermore, assuming that critical melt pool depths for upper and lower process boundaries d_l^* and d_u^* will stay constant, the values for the lower and upper boundaries H_{cdl}^* and H_{cdu}^* can be calculated by Equation 4.11 and Equation 4.12, respectively.

$$H_{cdl2}^* = \left(H_{cdl1}^{*1.17} - \frac{2(l_{t1}^* - l_{t2}^*)}{0.559} \right)^{\frac{1}{1.17}} \tag{4.11}$$

$$H_{cdu2}^* = \left(H_{cdl1}^{*1.17} - \frac{2(l_{t1}^* - l_{t2}^*)}{0.559} \right)^{\frac{1}{1.17}} \tag{4.12}$$

To evaluate the influence of layer thickness on melt pool dimensions and process boundaries, hatch packages of $10\,\mathrm{mm} \times 10\,\mathrm{mm}$ were built on substrate plates varying the applied powder layer thicknesses from $190\,\mu\mathrm{m}$ to $390\,\mu\mathrm{m}$ for six different parameter combinations. Predicted dimensionless melt pool depth d_p^* is plotted against measured dimensionless melt pool depth d^* in Figure 4.25a for the first hatches of each hatch package, corresponding to single scan tracks. The predicted melt pool depths for the different applied layer thicknesses were calculated based on Equation 4.10. The applied powder layer thicknesses of $190\,\mu\mathrm{m}$ to $390\,\mu\mathrm{m}$ correspond to nominal layer thicknesses of about $40\,\mu\mathrm{m}$, $60\,\mu\mathrm{m}$, and $80\,\mu\mathrm{m}$, respectively, for IN718 (Appendix A.1). It can be seen that data for nominal $60\,\mu\mathrm{m}$ and $80\,\mu\mathrm{m}$ fit well with calculated depths, while for $40\,\mu\mathrm{m}$ measured melt pool depths are all lower than predicted except one data point. However, most of the data points fall within the prediction error band of 32%, and thereby lie within the prediction error of the original allometric fit without powder layer thickness correction. It is interesting to note that a negative depth is predicted for the $390\,\mu\mathrm{m}$ data point with the lowest measured melt pool depth. Actually, one of the cross sections showed a complete disconnection from the substrate for this data point, qualitatively matching the predicted negative depth. Thus, it has been shown that the presented approach can be used to predict melt pool depths with variation of layer thickness for single scan tracks. A change in melt pool depth with

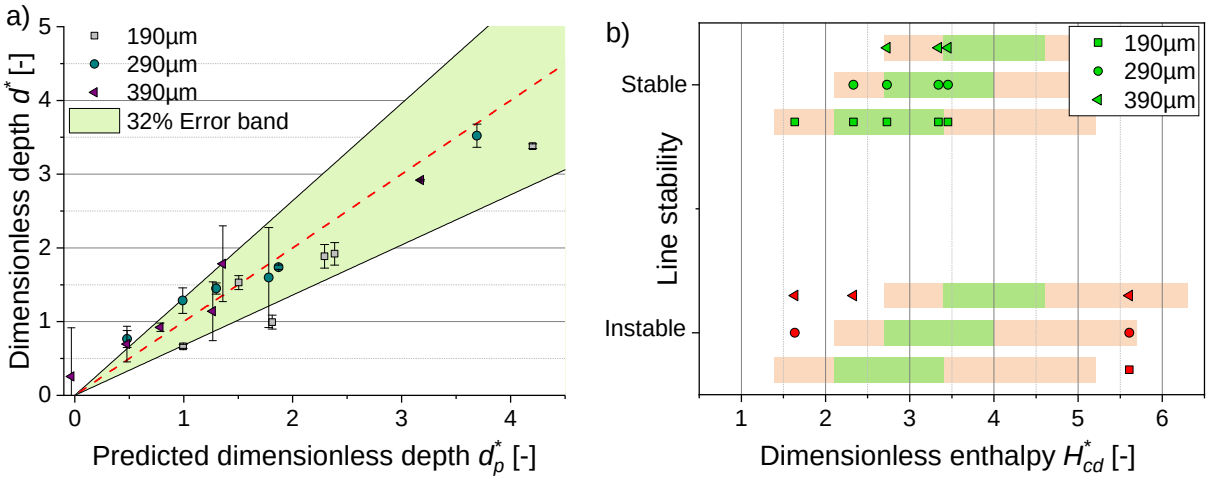

Figure 4.25: Influence of powder layer thickness variation on single scan tracks of IN718; a) predicted dimensionless melt pool depth d_p^* (after Equation 4.10) versus dimensionless melt pool depth d^* and b) shift in process window calculated from Equation 4.11 and 4.12

variation of layer thickness will introduce a shift in process window boundaries for H_{cd}^*. The first hatches of the investigated hatch packages were grouped into stable and instable lines using the same criteria as for single scan tracks such that all lines with either instability due to balling or keyhole porosity count as instable and all other lines as stable. The grouping is shown in Figure 4.25b over H_{cd}^*. Additionally, process window ranges were calculated based on Equation 4.11 and 4.12. The process windows for the various layer thicknesses are indicated by the green areas. Similarly, the H_{cd}^* ranges for 50% probability of a stable line were calculated and are indicated as orange areas. Since only six parameter combinations had been investigated, exact locations for the process boundaries at increasing layer thickness cannot be validated with this data set. However, a clear trend is still visible with a shift of process windows to higher H_{cd}^* with increasing layer thickness indicated by the increased number of instable low energy data points. For the lower H_{cd}^* side, one stable data point for each layer thickness is observed to lie outside the predicted process window. Nevertheless, those data points are still within the 50% range, while all instable single scan tracks obtain H_{cd}^* even below the 50% boundary. This indicates the conservative nature of the process window range based on 90% probability for stable lines. In contrast, keyhole porosity is found in samples within the 50% upper limit for $290\,\mu m$ and $390\,\mu m$ samples. However, single scan tracks with keyhole porosity all lie outside the upper process window boundary.

To investigate if the proposed approach would also be valuable when estimating the influence of powder layer thickness variation on scan tracks within a hatch package, the same calculations as previously done for single scan tracks were applied for hatches in the stable state. The results are shown in Figure 4.26. The predicted dimensionless melt pool depths d_p^* in Figure 4.26a match the measured depths even more closely than for the single scan tracks and all data points fall within the prediction error band of 32% from the original allometric fit. The categorized

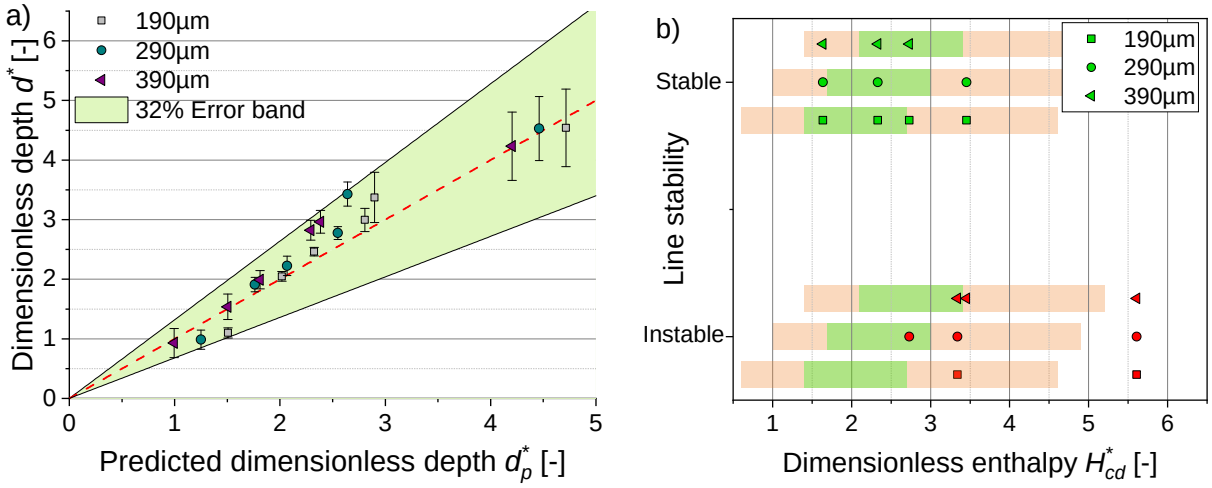

Figure 4.26: Influence of powder layer thickness variation on scan tracks within hatch packages of IN718; a) predicted dimensionless melt pool depth d_p^* versus dimensionless melt pool depth d^* and b) shift in process window

data points for the process window comparison are shown in Figure 4.26b together with the calculated 90% and 50% stable line probability ranges shaded in green and orange, respectively. In comparison with the single scan tracks, the process windows are shifted to lower H_{cd}^*. The shift between process windows with increasing layer thickness is smaller compared to the one for single scan tracks. The first observation can be explained since hatches within a hatch package obtain a higher melt pool depth compared to the first hatch at the same layer thickness. Therefore, a lower energy input is needed to reach similar melt pool depths. As was shown in the snapshots from HS video recordings in Figure 4.6, the laser does not only melt the powder within the interaction zone but additional powder is drawn towards the scan track from surrounding locations, increasing the amount of interacting material and creating a denudation zone around the scan tracks. For the first hatch, a denudation zone is created on both sides of the hatch, while for consecutive hatches, powder can only be drawn from one side, and thus a lower amount of powder from the surrounding is added to the interaction zone. Furthermore, this change in powder feed diminishes the influence of layer thickness variation for scan tracks within a hatch package and explains the smaller shift of the process window. The experimental results show no instability due to balling for all parameter combinations and all samples lie within the 50% lower process boundary. Samples denoted as instable show keyhole porosity and lie outside the corresponding upper process window boundaries, except two data points observed to contain keyhole pores which are within the predicted process window. For the process parameter combination at $290\,\mu m$, only one keyhole pore was observed within each cross section, and thus keyhole pore occurrence in this samples seems to have a low probability. Multiple keyhole pores were observed in cross sections for the $390\,\mu m$ parameter set lying within the process window. However, with $H_{cd}^* = 3.3$ it is close to the process window boundary of $H_{cd}^* = 3.4$, and therefore might be more susceptible to keyhole porosity formation. In contrast to single scan

tracks, stability of hatches within hatch packages can be further influenced by the connection between consecutive lines and local temperature fields from previous scans. Nevertheless, as a first estimate, the calculated process window ranges seem to fit the observations.

Despite the rough approximations made to take into account a variation of powder layer thickness, experimental results for single scan tracks as well as scan tracks within hatch packages match the calculated predictions. Thus, the presented method is suggested to get a first estimation of suitable process parameter combinations when changing layer thickness. Since the proposed method was only tested with a limited data set for IN718, it should be validated with a larger sample size including other alloys.

4.3 Application to three dimensional parts

To give an outlook on the applicability of the proposed process window based on H^*_{cd} for different process parameter combinations, density cubes were built in IN718 with selected process parameter combinations (Section 3.2.4). The relative density of those samples, evaluated by cross sectional microscopy as well as with Archimedes' principle, is shown in Figure 4.27a. From considerations of the previous section, the process window range for scan tracks within a hatch package at $l_t = 40\,\mu\mathrm{m}$ is calculated as $1.4 < H^*_{cd} < 2.7$ and is indicated in the figure as green area. The trend in relative density is similar for both measurement methods, although the Archimedes' method shows a higher deviation between samples and generally lower values. This might be a result of the volumetric measurement of the Archimedes' density, while for the cross sectional analysis only one cross section was evaluated, which might not contain a full representation of defects within the sample. It can be seen that all values within the process window obtain high densities and only a minor amount of defects are visible within the cross sections even at the lowest examined H^*_{cd} (see Figure 4.27b). A high density is further achieved for samples at $H^*_{cd} > 2.7$, but drops sharply for $H^*_{cd} > 3.2$. A high amount of keyhole porosity is noticeable within this high H^*_{cd} region (see Figure 4.27c). The results are in accordance with the hatch package observations for applied powder layer thickness of $190\,\mu\mathrm{m}$ such that keyhole porosity is observed within the scan tracks for $H^*_{cd} > 3.3$. Furthermore, the parameter combination obtaining no keyhole porosity within the hatch packages despite an H^*_{cd} value of 3.5 is the same that achieves very high density for the density cube sample. It can be assumed that this parameter combination is quite stable against keyhole porosity despite its high energy input. As proposed by Zhao et al. [81], critical melt pool depth for keyhole instability might vary with process parameter combinations, and thus the proposed constant critical depth for keyhole porosity onset gives a conservative estimate.

As for the hatch packages, density cubes with corresponding parameter combinations were additionally built at $60\,\mu\mathrm{m}$ and $80\,\mu\mathrm{m}$ nominal layer thickness. Relative density results for those samples are shown in Figure 4.28. Additionally, the calculated process window and 50%

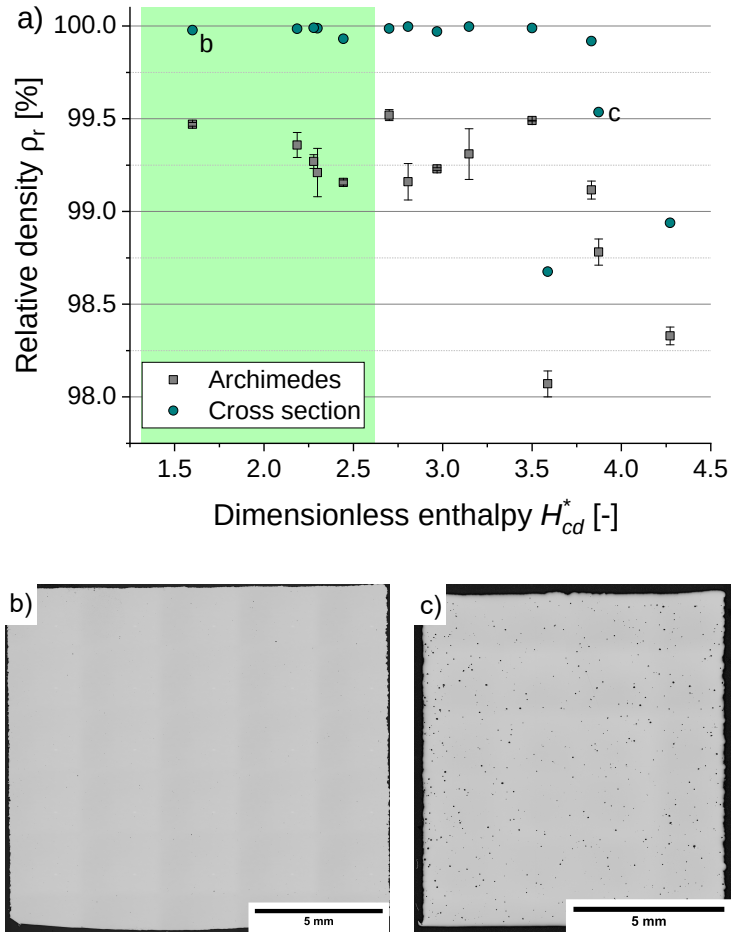

Figure 4.27: a) Relative density of sample cubes built at l_t = 40 µm with different process parameter combinations; b) and c) showing micrographs of samples indicated in a); the calculated process window is marked in green

probability range to achieve stable and defect free tracks are indicated as green and orange areas, respectively. For parameter combinations resulting in H^*_{cd} of 2.3 and 2.7, a high density (> 99.0%) is obtained at all investigated layer thicknesses. Since those H^*_{cd} values lie within the process windows for all layer thicknesses, a high relative density was expected. Despite the parameter set with $H^*_{cd} = 3.5$ being outside the process window for all investigated layer thicknesses, especially at $40\,\mu m$ and $60\,\mu m$, keyhole porosity was not observed. This parameter combination was also quite stable against keyhole porosity formation in the hatch package and single scan track experiments. The samples with the lowest H^*_{cd} of 1.6 for this investigation lie within the process window for $40\,\mu m$, matching the observed high density at this layer thickness. However, for $60\,\mu m$, the sample is only within the 50% probability limit, although it is close to the process window boundary of $H^*_{cd} = 1.7$. This might explain that a high density is still observed at $60\,\mu m$ nominal layer thickness. In contrast, a high amount of porosity is observed for the $80\,\mu m$ sample, which lies close to the 50% stability boundary of $H^*_{cd} = 1.4$. A large amount of lack-of-fusion pores were found to have formed within this sample as shown by the micrograph

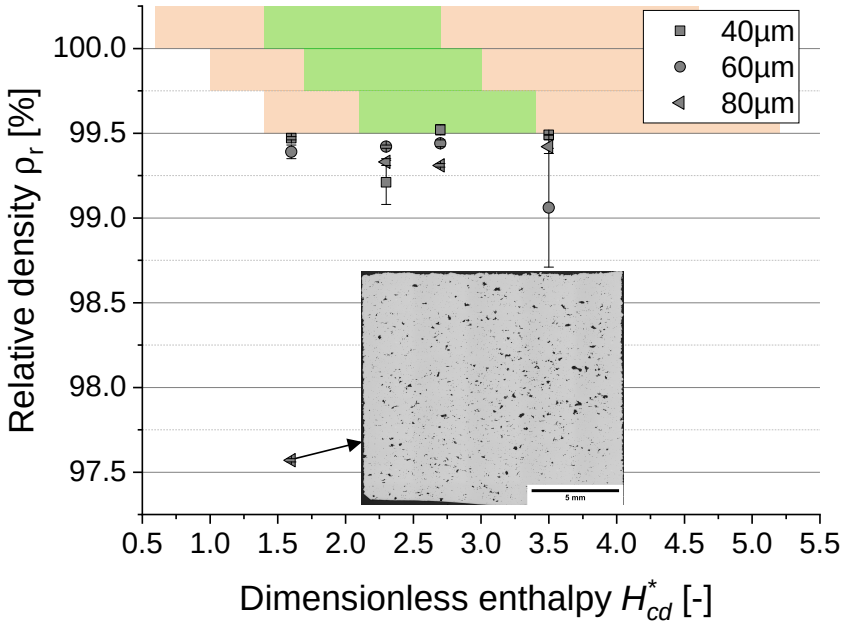

Figure 4.28: Relative density measured by Archimedes' principle of sample cubes built at different nominal layer thicknesses; inset showing a micrograph of a sample containing lack-of-fusion porosity; the calculated process window and the 50% probability range to achieve stable and defect free tracks are indicated in green and orange, respectively

in the inset. Interestingly, this parameter set resulted in stable scan tracks for the corresponding hatch package experiment at $390\,\mu\mathrm{m}$ applied powder layer thickness ($l_t \approx 80\,\mu\mathrm{m}$). A possible explanation could be an increase in instability due to the difference in surface roughness from layer to layer within a multi layer build, compared to the smooth sample substrate. This shows that additional influencing factors have to be taken into account when transferring process parameters to multi layer builds.

To conclude, the results of the density cube experiments qualitatively match the proposed outcomes and the process window seems to be conservatively approximated with the proposed H^*_{cd} range. Thus, the model can be used to get first estimations of viable process parameter combinations to use in a parameter study. Further investigations should concentrate on the connection between porosity fraction and probability of defect formation such that a viable process window might also be defined at a single line defect probability less than 90%. Moreover, the applicability should be tested with other alloys and different quality measures, e.g., surface roughness or residual stresses.

5 Summary

With industrialization of LPBF, requirements on part quality, productivity, and material selection become ever more demanding, arising the need for continuous revision of existing processes and process development for new alloys. To enable a timely and cost efficient process parameter screening, the applicability of dimensionless scaling laws for characterizing melt pool dimensions and process windows in a machine and material agnostic way was investigated. The dimensionless enthalpy H^*, representing a ratio of energy input by the laser to the energy required for the interacting material to melt, has been used as a starting point to correlate melt pool dimensions of single scan tracks for five different alloys commonly used in LPBF and covering a range of thermophysical properties, namely IN718, MS1, 316L, Ti64, and AlSi10Mg. Besides geometrical evaluation, single scan tracks were characterized based on surface stability and porosity formation to evaluate respective process windows. In addition, single layer hatch packages and density cubes were built to give an outlook on the applicability of the proposed scaling laws to three dimensional parts.

The dimensionless enthalpy H^* alone was found insufficient to describe melt pool dimensions for different process parameter combinations and a dependence of melt pool dimensions on the Peclet number Pe was observed. The variation of melt pool dimensions with Pe is divided in a low Pe region, where melt pool dimensions increase with increasing Pe, and a high Pe region, with a decrease of melt pool dimensions with increasing Pe. This division can be attributed to a change in the primary heat loss mechanism from convection to conduction towards lower Pe. The Pe value at which this transition happened was observed to vary for melt pool depth and melt pool width. In addition, it was found to be dependent on the material. For melt pool depth, the transition occurred at a higher Pe compared to melt pool width. This was attributed to additional heat loss within the melt pool by convective melt pool flows, such as the Marangoni convection, at low Pe. Thereby, also the shift in transition from Pe around 4 for the investigated steels to lower Pe numbers for Ti64 and AlSi10Mg was explained. Based on the observed Pe dependence for melt pool width and depth, two new dimensionless numbers combining H^* and Pe were proposed to correlate melt pool dimensions. For dimensionless melt pool depth d^*, experimental data was observed to fall on a common trend line for all investigated alloys when plotted over $H^*_{cd} = H^* / \sqrt{Pe}$. The common trend line was fit by $d^* = 0.559 H^{*1.17}_{cd}$ with a prediction error of $\pm 32\%$ for samples in keyhole mode. For samples in conduction mode a trend for over-prediction was observed and quality of prediction was diminished, with the maximal error being -62%. In addition to H^* and Pe, for melt pool width, the ratio between boiling and solidus isotherms $T_b/T_{solidus}$, defining the relation between keyhole and melt pool width, had to be taken into account for a common scaling of all investigated alloys. This gave a scaling law for melt pool width of $w^* T_{solidus}/T_b = 1.439(1 - H^{*-0.65}_{cw})$ with $H^*_{cw} = H^* / Pe^{0.2}$. The prediction error for melt pool width was within $\pm 20\%$ for 95% of data. Thus, application of H^*_{cd} and H^*_{cw}

enabled the introduction of material agnostic scaling laws to predict melt pool dimensions depth and width within acceptable accuracy.

Defect formation is strongly correlated to melt pool depth since insufficient melting of the underlying substrate leads to balling instability, while deep melt pools are prone to keyhole porosity formation. Therefore, process windows for the different alloys were evaluated based on H^*_{cd}. For IN718, MS1, 316L, and Ti64, a common process window, defined by 90% probability to create stable and defect free single scan tracks, was found with $2.1 < H^*_{cd} < 3.4$. Despite AlSi10Mg matching the scaling for dimensionless melt pool depth of the other investigated alloys, data did not show a process window falling within the proposed range and further research should concentrate on investigating the difference in melt pool dynamics for this alloy. The proposed process window was found only valid within a material specific speed range limited on the lower side by the previously observed change in Pe scaling and on the upper side by the onset of humping. While the lower limiting speed is of less importance in an industrial context, knowledge about the humping onset velocity u_{Hump} is especially important as it limits productivity. At scan speeds above u_{Hump}, stable single scan tracks were not achievable irrespective of laser power scan speed combination. Thus, u_{Hump} sets an upper limit on processing speed. The value of u_{Hump} was observed to depend on material properties and increased from about $1200\,\mathrm{mm/s}$ to $1270\,\mathrm{mm/s}$ for the investigated steels and IN718 to around $1550\,\mathrm{mm/s}$ for Ti64. Due to the significantly different thermophysical properties compared to the other alloys, the knowledge of u_{Hump} for AlSi10Mg would be of special interest to understand its material dependence. However, a conclusive estimate of u_{Hump} for AlSi10Mg could not be deduced from the presented data.

To extend the applicability of the observed single scan track results for varying powder layer thicknesses, a method was suggested how to shift the proposed process window and predict melt pool depths in dependence of powder layer thickness. Good results were achieved for depth prediction of single scan tracks built at different applied powder layer thicknesses as well as scan tracks within a hatch package. The majority of predicted melt pool depths obtained an error within the 32% error range of the original fit. The predicted process window shift for single scan tracks and tracks within a hatch package with layer thickness variation qualitatively agreed with experimental observations. Similarly, regions of lack-of-fusion defects and keyhole porosity in density cube evaluations were explained by process parameter combinations with unfavorable H^*_{cd}.

To summarize, the proposed scalings for melt pool width and depth can be used to predict respective melt pool dimensions if process parameters and material thermophysical properties are known. Process parameters can then be selected based on predefined geometrical requirements or additional process parameters not included within the scaling laws can be selected in accordance with the geometrical results, e.g., hatch distance in relation to melt pool width. Additionally, the probability to achieve a stable and defect free track can be evaluated for different parameter

combinations prior to experiments using the logistic regression fit for the common process window. This enables a fast and easy screening of a vast parameter space and a selection of promising parameter subsets prior to an experimental evaluation. However, the proposed process window is only valid for parameter and material combinations with scan speeds above the transition value of the Pe dependence and below u_{Hump}.

While this work provided a hypothesis on the physical mechanism behind the transition in Pe dependence of melt pool dimensions, the influence of the beam diameter, as another important parameter to calculate Pe, was not evaluated. Therefore, further research should focus on the influence of the beam diameter on the Pe transition as well as on checking the proposed hypothesis that melt pool convection is responsible for the material dependence of the transition value. Correspondingly, supplemental research should focus on the characterization of u_{Hump}, using dimensionless numbers to enable a prediction of the limiting process speeds for specific material and hardware characteristics. Deeper investigations into the effect of focus position, beam size and shape on u_{Hump} are proposed not only in regard to better understand the humping phenomenon, but also to enable the development of effective prevention strategies. In general, proposed scalings for melt pool dimensions and the process window should be tested with further alloys, especially ones having high thermal diffusivity, such as Cu-alloys, to ensure universality. Although laser beam diameter a and initial temperature T_0 are included within the used dimensionless numbers, their correct scaling was not evaluated, since neither a nor T_0 were greatly varied within this work. Furthermore, the proposed method to calculate melt pool depth and process window limits with variation of nominal layer thickness was only tested for IN718 within this work and should therefore be validated studying other materials. To enable process parameter combinations to be optimized for specific process outcomes, e.g., a specific build rate with allowance of a certain defect percentage, it would be of high interest to quantitatively correlate part quality attributes, such as density or surface roughness, with H^*_{cd}. Such a direct scaling would enable the process developer to easily select process parameter combinations for different materials based on costumer specific requirements and machine hardware options. Besides part density and topography, it can also be assumed that H^*_{cd} influences microstructure and texture formation within a part due to the influence on remelting area as well as the surface to volume ratio of a melt pool.

Bibliography

[1] T. T. Wohlers and Wohlers Associates. *Wohlers Report 2011: Additive Manufacturing and 3D Printing State of the Industry*. Wohlers Associates, Fort Collins, 2011.

[2] T. T. Wohlers, I. Campbell, O. Diegel, R. Huff, J. Kowen, and Wohlers Associates. *Wohlers Report 2020: 3D Printing and Additive Manufacturing State of the Industry*. Wohlers Associates, Fort Collins, 2020.

[3] AMFG Autonomous Manufacturing. Industrial Applications of 3D Printing: The Ultimate Guide. `https://amfg.ai/industrial-applications-of-3d-printing-the-ultimate-guide/`, Accessed: 06.11.2021.

[4] Clare Scott. BMW Impresses with 3D Printed Roof Bracket for BMW i8 Roadster. `https://3dprint.com/222268/bmw-3d-printed-roof-bracket`, Accessed: 06.11.2021.

[5] M. Munsch, M. Schmidt-Lehr, and E. Wycisk. *AMPOWER Report 2021: Metal Additive Manufacturing*. AMPOWER GmbH & Co. KG, Hamburg, 2021.

[6] SmarTech Analysis. *Additive Manufacturing with Metal Powders 2020*. SmarTech Analysis, Crozet, 2020.

[7] M. Revilla-León, M. Sadeghpour, and M. Özcan. A review of the applications of additive manufacturing technologies used to fabricate metals in implant dentistry. *Journal of prosthodontics: official journal of the American College of Prosthodontists*, 29(7):579–593, 2020.

[8] X. Wang, S. Xu, S. Zhou, W. Xu, M. Leary, P. Choong, M. Qian, M. Brandt, and Y. M. Xie. Topological design and additive manufacturing of porous metals for bone scaffolds and orthopaedic implants: A review. *Biomaterials*, 83:127–141, 2016.

[9] A. Katz-Demyanetz, V. V. Popov, A. Kovalevsky, D. Safranchik, and A. Koptyug. Powder-bed additive manufacturing for aerospace application: Techniques, metallic and metal/ceramic composite materials and trends. *Manufacturing Review*, 6:5–18, 2019.

[10] L. Berrocal, R. Fernández, S. González, A. Periñán, S. Tudela, J. Vilanova, L. Rubio, J. M. Martín Márquez, J. Guerrero, and F. Lasagni. Topology optimization and additive manufacturing for aerospace components. *Progress in Additive Manufacturing*, 4(2):83–95, 2019.

[11] R. Leal, F. M. Barreiros, L. Alves, F. Romeiro, J. C. Vasco, M. Santos, and C. Marto. Additive manufacturing tooling for the automotive industry. *The International Journal of Advanced Manufacturing Technology*, 92(5):1671–1676, 2017.

[12] C. Tan, Di Wang, W. Ma, Y. Chen, S. Chen, Y. Yang, and K. Zhou. Design and additive manufacturing of novel conformal cooling molds. *Materials & Design*, 196:109147, 2020.

[13] F. Cooper. Sintering and additive manufacturing: the new paradigm for the jewellery manufacturer. *Johnson Matthey Technology Review*, 59(3):233–242, 2015.

[14] A. Vafadar, F. Guzzomi, A. Rassau, and K. Hayward. Advances in metal additive manufacturing: A review of common processes, industrial applications, and current challenges. *Applied Sciences*, 11(3):1213, 2021.

[15] F. Bosio, A. Aversa, M. Lorusso, S. Marola, D. Gianoglio, L. Battezzati, P. Fino, D. Manfredi, and M. Lombardi. A time-saving and cost-effective method to process alloys by laser powder bed fusion. *Materials & Design*, 181:107949, 2019.

[16] A. K. Agrawal, G. Meric de Bellefon, and D. Thoma. High-throughput experimentation for microstructural design in additively manufactured 316L stainless steel. *Materials Science and Engineering: A*, 793:139841, 2020.

[17] K. Huang, C. Kain, N. Diaz-Vallejo, Y. Sohn, and Le Zhou. High throughput mechanical testing platform and application in metal additive manufacturing and process optimization. *Journal of Manufacturing Processes*, 66:494–505, 2021.

[18] S. A. Khairallah, A. T. Anderson, A. Rubenchik, and W. E. King. Laser powder-bed fusion additive manufacturing: Physics of complex melt flow and formation mechanisms of pores, spatter, and denudation zones. *Acta Materialia*, 108:36–45, 2016.

[19] A. M. Philo, S. Mehraban, M. Holmes, S. Sillars, C. J. Sutcliffe, J. Sienz, S. G. R. Brown, and N. P. Lavery. A pragmatic continuum level model for the prediction of the onset of keyholing in laser powder bed fusion. *The International Journal of Advanced Manufacturing Technology*, 101(1):697–714, 2019.

[20] P. S. Cook and A. B. Murphy. Simulation of melt pool behaviour during additive manufacturing: Underlying physics and progress. *Additive Manufacturing*, 31:100909, 2020.

[21] C. Körner, E. Attar, and P. Heinl. Mesoscopic simulation of selective beam melting processes. *Journal of Materials Processing Technology*, 211(6):978–987, 2011.

[22] Z. Zhang, Y. Huang, A. Rani Kasinathan, S. Imani Shahabad, U. Ali, Y. Mahmoodkhani, and E. Toyserkani. 3-dimensional heat transfer modeling for laser powder-bed fusion additive manufacturing with volumetric heat sources based on varied thermal conductivity and absorptivity. *Optics & Laser Technology*, 109:297–312, 2019.

[23] B. Rankouhi, A. K. Agrawal, F. E. Pfefferkorn, and D. J. Thoma. A dimensionless number for predicting universal processing parameter boundaries in metal powder bed additive manufacturing. *Manufacturing Letters*, 27:13–17, 2021.

[24] R. Fabbro. Scaling laws for the laser welding process in keyhole mode. *Journal of Materials Processing Technology*, 264:346–351, 2019.

[25] A. Großmann, J. Mölleney, T. Frölich, H. Merschroth, J. Felger, M. Weigold, A. Sielaff, and C. Mittelstedt. Dimensionless process development for lattice structure design in laser powder bed fusion. *Materials & Design*, 194:108952, 2020.

[26] A. M. Rubenchik, W. E. King, and S. Wu. Scaling laws for the additive manufacturing. *Journal of Materials Processing Technology*, 257:234–243, 2018.

[27] J. Ye, S. A. Khairallah, A. M. Rubenchik, M. F. Crumb, G. Guss, J. Belak, and M. J. Matthews. Energy coupling mechanisms and scaling behavior associated with laser powder bed fusion additive manufacturing. *Advanced Engineering Materials*, 21(7):1900185, 2019.

[28] Z. Gan, O. L. Kafka, N. Parab, C. Zhao, L. Fang, O. Heinonen, T. Sun, and W. K. Liu. Universal scaling laws of keyhole stability and porosity in 3D printing of metals. *Nature communications*, 12(1):2379, 2021.

[29] Z. Wang and M. Liu. Dimensionless analysis on selective laser melting to predict porosity and track morphology. *Journal of Materials Processing Technology*, 273:116238, 2019.

[30] H. Ghasemi-Tabasi, J. Jhabvala, E. Boillat, T. Ivas, R. Drissi-Daoudi, and R. E. Logé. An effective rule for translating optimal selective laser melting processing parameters from one material to another. *Additive Manufacturing*, 36:101496, 2020.

[31] Z. Islam, A. K. Agrawal, B. Rankouhi, C. Magnin, M. H. Anderson, F. E. Pfefferkorn, and D. J. Thoma. A high-throughput method to define additive manufacturing process parameters: Application to Haynes 282. *Metallurgical and Materials Transactions A*, 53(1):250–263, 2022.

[32] W. Yuan, H. Chen, T. Cheng, and Q. Wei. Effects of laser scanning speeds on different states of the molten pool during selective laser melting: Simulation and experiment. *Materials & Design*, 189:108542, 2020.

[33] E. Kundakcıoğlu, I. Lazoglu, Ö. Poyraz, E. Yasa, and N. Cizicioğlu. Thermal and molten pool model in selective laser melting process of Inconel 625. *The International Journal of Advanced Manufacturing Technology*, 95(9):3977–3984, 2018.

[34] S. I. Shahabad, Z. Zhang, A. Keshavarzkermani, U. Ali, Y. Mahmoodkhani, R. Esmaeilizadeh, A. Bonakdar, and E. Toyserkani. Heat source model calibration for thermal analysis of laser powder-bed fusion. *The International Journal of Advanced Manufacturing Technology*, 106(7):3367–3379, 2020.

[35] W. E. King. Laser powder bed fusion additive manufacturing of metals; physics, computational, and materials challenges. *Applied Physics Reviews*, 2(4):041304, 2015.

[36] DIN EN ISO/ASTM 52900:2022-03, Additive Manufacturing - General principles - Fundamentals and vocabulary (ISO/ASTM 52900:2021).

[37] D. Herzog, V. Seyda, E. Wycisk, and C. Emmelmann. Additive manufacturing of metals. *Acta Materialia*, 117:371–392, 2016.

[38] T. DebRoy, H. L. Wei, J. S. Zuback, T. Mukherjee, J. W. Elmer, J. O. Milewski, A. M. Beese, A. Wilson-Heid, A. De, and W. Zhang. Additive manufacturing of metallic components – process, structure and properties. *Progress in Materials Science*, 92:112–224, 2018.

[39] O. Diegel. Additive manufacturing: An overview. In S. Hashmi, ed., *Comprehensive Materials Processing*, vol. 10, p. 3–18. Elsevier, Amsterdam, 2014.

[40] I. Gibson, D. Rosen, and B. Stucker. *Additive Manufacturing Technologies*. Springer, New York, 2015.

[41] S. Kumar. Selective laser sintering/melting. In S. Hashmi, ed., *Comprehensive Materials Processing*, vol. 10, p. 93–134. Elsevier, Amsterdam, 2014.

[42] SLM Solutions Group AG. The-nxg. `https://www.slm-pushing-the-limits.com`, Accessed: 14.06.2021.

[43] EOS Electro Optical Systems GmbH. Metal materials. `https://www.eos.info/en/additive-manufacturing/3d-printing-metal/dmls-metal-materials`, Accessed: 02.11.2021.

[44] SLM Solutions Group AG. Powders. `https://www.slm-solutions.com/products-and-solutions/powders`, Accessed: 02.11.2021.

[45] Oerlikon AG. Metal powders. `https://www.oerlikon.com/am/en/offerings/metal-powders`, Accessed: 02.11.2021.

[46] A. Aversa, G. Marchese, A. Saboori, E. Bassini, D. Manfredi, S. Biamino, D. Ugues, P. Fino, and M. Lombardi. New aluminum alloys specifically designed for laser powder bed fusion: A review. *Materials*, 12(7), 2019.

[47] S. L. Sing and W. Y. Yeong. Laser powder bed fusion for metal additive manufacturing: perspectives on recent developments. *Virtual and Physical Prototyping*, 15(3):359–370, 2020.

[48] L. Thijs, K. Kempen, J.-P. Kruth, and J. van Humbeeck. Fine-structured aluminium products with controllable texture by selective laser melting of pre-alloyed AlSi10Mg powder. *Acta Materialia*, 61(5):1809–1819, 2013.

[49] J. Metelkova, L. Vanmunster, H. Haitjema, and B. van Hooreweder. Texture of inclined up-facing surfaces in laser powder bed fusion of metals. *Additive Manufacturing*, 42:101970, 2021.

[50] J. L. Bartlett and X. Li. An overview of residual stresses in metal powder bed fusion. *Additive Manufacturing*, 27:131–149, 2019.

[51] J. Metelkova, Y. Kinds, K. Kempen, C. de Formanoir, A. Witvrouw, and B. van Hooreweder. On the influence of laser defocusing in selective laser melting of 316L. *Additive Manufacturing*, 23:161–169, 2018.

[52] M. Van Elsen. *Complexity of Selective Laser Melting: A new optimisation approach*. PhD thesis, Katholieke Universiteit Leuven, Leuven, 2007.

[53] J. T. Sehrt. *Möglichkeiten und Grenzen bei der generativen Herstellung metallischer Bauteile durch das Strahlschmelzverfahren*. Berichte aus der Fertigungstechnik. Shaker, Aachen, 2010. (PhD thesis at University Duisburg-Essen).

[54] T. M. Wischeropp, H. Tarhini, and C. Emmelmann. Influence of laser beam profile on the selective laser melting process of AlSi10Mg. *Journal of Laser Applications*, 32(2):022059, 2020.

[55] T. T. Roehling, S. S. Wu, S. A. Khairallah, J. D. Roehling, S. S. Soezeri, M. F. Crumb, and M. J. Matthews. Modulating laser intensity profile ellipticity for microstructural control during metal additive manufacturing. *Acta Materialia*, 128:197–206, 2017.

[56] W. E. King, H. D. Barth, V. M. Castillo, G. F. Gallegos, J. W. Gibbs, D. E. Hahn, C. Kamath, and A. M. Rubenchik. Observation of keyhole-mode laser melting in laser powder-bed fusion additive manufacturing. *Journal of Materials Processing Technology*, 214(12):2915–2925, 2014.

[57] W. Meiners. *Direktes selektives Laser Sintern einkomponentiger metallischer Werkstoffe*. PhD thesis, RWTH Aachen, Aachen, 1999.

[58] T. M. Wischeropp, C. Emmelmann, M. Brandt, and A. Pateras. Measurement of actual powder layer height and packing density in a single layer in selective laser melting. *Additive Manufacturing*, 28:176–183, 2019.

[59] H. W. Mindt, M. Megahed, N. P. Lavery, M. A. Holmes, and S. G. R. Brown. Powder bed layer characteristics: The overseen first-order process input. *Metallurgical and Materials Transactions A*, 47(8):3811–3822, 2016.

[60] Y. Mahmoodkhani, U. Ali, S. Imani Shahabad, A. Rani Kasinathan, R. Esmaeilizadeh, A. Keshavarzkermani, E. Marzbanrad, and E. Toyserkani. On the measurement of effective powder layer thickness in laser powder-bed fusion additive manufacturing of metals. *Progress in Additive Manufacturing*, 4(2):109–116, 2019.

[61] P. Bidare, R. Maier, R. J. Beck, J. D. Shephard, and A. J. Moore. An open-architecture metal powder bed fusion system for in-situ process measurements. *Additive Manufacturing*, 16:177–185, 2017.

[62] P. Bidare, I. Bitharas, R. M. Ward, M. M. Attallah, and A. J. Moore. Fluid and particle dynamics in laser powder bed fusion. *Acta Materialia*, 142:107–120, 2018.

[63] S. Ly, A. M. Rubenchik, S. A. Khairallah, G. Guss, and M. J. Matthews. Metal vapor microjet controls material redistribution in laser powder bed fusion additive manufacturing. *Scientific reports*, 7(1):4085, 2017.

[64] M. J. Matthews, G. Guss, S. A. Khairallah, A. M. Rubenchik, P. J. Depond, and W. E. King. Denudation of metal powder layers in laser powder bed fusion processes. *Acta Materialia*, 114:33–42, 2016.

[65] Q. B. Nguyen, D. N. Luu, S. Nai, Z. Zhu, Z. Chen, and J. Wei. The role of powder layer thickness on the quality of SLM printed parts. *Archives of Civil and Mechanical Engineering*, 18(3):948–955, 2018.

[66] P. Mercelis and J.-P. Kruth. Residual stresses in selective laser sintering and selective laser melting. *Rapid Prototyping Journal*, 12(5):254–265, 2006.

[67] O. Illies. *Simulationsbasierte thermische Analyse zur Anpassung der Hatching-Strategie beim selektiven Laserstrahlschmelzen*. PhD thesis, University Bremen, Bremen, 2020.

[68] A. A. Martin, N. P. Calta, J. A. Hammons, S. A. Khairallah, M. H. Nielsen, R. M. Shuttlesworth, N. Sinclair, M. J. Matthews, J. R. Jeffries, T. M. Willey, and J. R. Lee. Ultrafast dynamics of laser-metal interactions in additive manufacturing alloys captured by in situ x-ray imaging. *Materials Today Advances*, 1:100002, 2019.

[69] S. A. Khairallah, A. A. Martin, J. R. I. Lee, G. Guss, N. P. Calta, J. A. Hammons, M. H. Nielsen, K. Chaput, E. Schwalbach, M. N. Shah, M. G. Chapman, T. M. Willey, A. M. Rubenchik, A. T. Anderson, Y. M. Wang, M. J. Matthews, and W. E. King. Controlling interdependent meso-nanosecond dynamics and defect generation in metal 3D printing. *Science*, 368(6491):660–665, 2020.

[70] K. Kempen, L. Thijs, B. Vrancken, S. Buls, J. Van Humbeeck, and J.-P. Kruth. Lowering thermal gradients in selective laser melting by pre-heating the base plate. In *Solid Freeform Fabrication Symposium Proceedings*, Austin, 2013.

[71] R. Mertens, S. Dadbakhsh, J. Van Humbeeck, and J.-P. Kruth. Application of base plate preheating during selective laser melting. *Procedia CIRP*, 74:5–11, 2018.

[72] A. B. Anwar and Q.-C. Pham. Selective laser melting of AlSi10Mg: Effects of scan direction, part placement and inert gas flow velocity on tensile strength. *Journal of Materials Processing Technology*, 240:388–396, 2017.

[73] A. Ladewig, G. Schlick, M. Fisser, V. Schulze, and U. Glatzel. Influence of the shielding gas flow on the removal of process by-products in the selective laser melting process. *Additive Manufacturing*, 10:1–9, 2016.

[74] J. Reijonen, A. Revuelta, T. Riipinen, K. Ruusuvuori, and P. Puukko. On the effect of shielding gas flow on porosity and melt pool geometry in laser powder bed fusion additive manufacturing. *Additive Manufacturing*, 32:101030, 2020.

[75] B. Ferrar, L. Mullen, E. Jones, R. Stamp, and C. J. Sutcliffe. Gas flow effects on selective laser melting (SLM) manufacturing performance. *Journal of Materials Processing Technology*, 212(2):355–364, 2012.

[76] S. Katayama, ed. *Handbook of laser welding technologies*, vol. 41 of *Woodhead Publishing series in electronic and optical materials*. Woodhead Publishing, Oxford, 2013.

[77] E. G. Assuncao. *Investigation of conduction to keyhole mode transition*. PhD thesis, Cranfield University, Cranfield, 2012.

[78] R. Fabbro and K. Chouf. Keyhole modeling during laser welding. *Journal of Applied Physics*, 87(9):4075–4083, 2000.

[79] E. Beyer. *Schweißen mit Laser: Grundlagen*. Springer, Berlin, 1995.

[80] R. Cunningham, C. Zhao, N. Parab, C. Kantzos, J. Pauza, K. Fezzaa, T. Sun, and A. D. Rollett. Keyhole threshold and morphology in laser melting revealed by ultrahigh-speed x-ray imaging. *Science*, 363(6429):849–852, 2019.

[81] C. Zhao, N. D. Parab, X. Li, K. Fezzaa, W. Tan, A. D. Rollett, and T. Sun. Critical instability at moving keyhole tip generates porosity in laser melting. *Science*, 370(6520):1080–1086, 2020.

[82] A. Matsunawa, M. Mizutani, S. Katayama, and N. Seto. Porosity formation mechanism and its prevention in laser welding. *Welding International*, 17(6):431–437, 2003.

[83] S. Tsukamoto, I. Kawaguchi, G. Arakane, and H. Honda. Keyhole behavior in high power laser welding. In *First International Symposium on High-Power Laser Macroprocessing*, vol. 4831, p. 251–256, Osaka, 2003.

[84] P. Berger, H. Hügel, and T. Graf. Understanding pore formation in laser beam welding. *Physics Procedia*, 12:241–247, 2011.

[85] C. Zhao, Q. Guo, X. Li, N. Parab, K. Fezzaa, W. Tan, L. Chen, and T. Sun. Bulk-explosion-induced metal spattering during laser processing. *Physical Review X*, 9(2):021052, 2019.

[86] J. Y. Lee, S. H. Ko, D. F. Farson, and C. D. Yoo. Mechanism of keyhole formation and stability in stationary laser welding. *Journal of Physics D: Applied Physics*, 35(13):1570–1576, 2002.

[87] R. W. Cunningham. *Defect formation mechanisms in powder bed metal additive manufacturing*. PhD thesis, Carnegie Mellon University, Pittsburgh, 2018.

[88] C. Zhao, K. Fezzaa, R. W. Cunningham, H. Wen, F. de Carlo, L. Chen, A. D. Rollett, and T. Sun. Real-time monitoring of laser powder bed fusion process using high-speed x-ray imaging and diffraction. *Scientific reports*, 7(1):3602, 2017.

[89] J. J. S. Dilip, S. Zhang, C. Teng, K. Zeng, C. Robinson, D. Pal, and B. Stucker. Influence of processing parameters on the evolution of melt pool, porosity, and microstructures in Ti-6Al-4V alloy parts fabricated by selective laser melting. *Progress in Additive Manufacturing*, 2(3):157–167, 2017.

[90] A. V. Gusarov, I. Yadroitsev, P. Bertrand, and I. Smurov. Model of radiation and heat transfer in laser-powder interaction zone at selective laser melting. *Journal of Heat Transfer*, 131(7):1–10, 2009.

[91] I. Yadroitsev and I. Smurov. Selective laser melting technology: From the single laser melted track stability to 3D parts of complex shape. *Physics Procedia*, 5:551–560, 2010.

[92] I. Yadroitsev, A. Gusarov, I. Yadroitsava, and I. Smurov. Single track formation in selective laser melting of metal powders. *Journal of Materials Processing Technology*, 210(12):1624–1631, 2010.

[93] J. P. Kruth, L. Froyen, J. van Vaerenbergh, P. Mercelis, M. Rombouts, and B. Lauwers. Selective laser melting of iron-based powder. *Journal of Materials Processing Technology*, 149:616–622, 2004.

[94] T. H. C. Childs, C. Hauser, and M. Badrossamay. Selective laser sintering (melting) of stainless and tool steel powders: Experiments and modelling. *Proceedings of the Institution of Mechanical Engineers, Part B: Journal of Engineering Manufacture*, 219(4):339–357, 2005.

[95] C. Weber. Zum Zerfall eines Flüssigkeitsstrahles. *Zeitschrift für Angewandte Mathematik und Mechanik*, 11(2):136–154, 1931.

[96] R. Li, J. Liu, Y. Shi, L. Wang, and W. Jiang. Balling behavior of stainless steel and nickel powder during selective laser melting process. *The International Journal of Advanced Manufacturing Technology*, 59(9):1025–1035, 2012.

[97] Y. Lee and W. Zhang. Mesoscopic simulation of heat transfer and fluid flow in laser powder bed additive manufacturing. In *Solid Freeform Fabrication Symposium Proceedings*, p. 1154–1165, Austin, 2015.

[98] M. Rombouts, J. P. Kruth, L. Froyen, and P. Mercelis. Fundamentals of selective laser melting of alloyed steel powders. *CIRP Annals*, 55(1):187–192, 2006.

[99] J. Bliedtner, H. Müller, and A. Barz. *Lasermaterialbearbeitung: Grundlagen - Verfahren - Anwendungen - Beispiele*. Carl-Hanser-Verlag, Munich, 2013.

[100] U. Gratzke, P. D. Kapadia, J. Dowden, J. Kroos, and G. Simon. Theoretical approach to the humping phenomenon in welding processes. *Journal of Physics D: Applied Physics*, 25(11):1640–1647, 1992.

[101] C. Thomy, T. Seefeld, and F. Vollertsen. Humping effect in welding of steel with single-mode fibre laser. *Welding in the World*, 52(5):9–18, 2008.

[102] A. Hess and F. Dausinger. Humping mechanisms during high-speed welding with brilliant lasers. In *Pacific International Conference on Applications of Lasers and Optics*, p. 140–145, Bejing, 2008.

[103] R. Fabbro. Melt pool and keyhole behavior analysis for deep penetration laser welding. *Journal of Physics D: Applied Physics*, 43(44):445501, 2010.

[104] P. Berger, H. Hügel, A. Hess, R. Weber, and T. Graf. Understanding of humping based on conservation of volume flow. *Physics Procedia*, 12:232–240, 2011.

[105] M. Seiler, A. Patschger, and J. Bliedtner. Investigations of welding instabilities and weld seam formation during laser microwelding of ultrathin metal sheets. *Journal of Laser Applications*, 28(2):022417, 2016.

[106] A. Patschger, M. Seiler, and J. Bliedtner. Influencing factors on humping effect in laser welding with small aspect ratios. *Journal of Laser Applications*, 30(3):032409, 2018.

[107] R. Fabbro, S. Slimani, F. Coste, and F. Briand. Analysis of the various melt pool hydrodynamic regimes observed during cw Nd-YAG deep penetration laser welding. In *International Congress on Applications of Lasers & Electro-Optics*, p. 802, Orlando, 2007.

[108] M. Beck, P. Berger, F. Dausinger, and H. Huegel. Aspects of keyhole/melt interaction in high-speed laser welding. In *Eighth International Symposium on Gas-Flow and Chemical Lasers*, p. 769–774, 1991.

[109] R. Fabbro, S. Slimani, F. Coste, and F. Briand. Experimental study of the humping process during Nd:YAG laser welding. In *Proceedings of the LIM Conference*, p. 18–21, Munich, 2007.

[110] C. Tang, K. Q. Le, and C. H. Wong. Physics of humping formation in laser powder bed fusion. *International Journal of Heat and Mass Transfer*, 149:119172, 2020.

[111] N. Makoana, I. Yadroitsava, H. Möller, and I. Yadroitsev. Characterization of 17-4PH single tracks produced at different parametric conditions towards increased productivity of LPBF systems - the effect of laser power and spot size upscaling. *Metals*, 8(7):475, 2018.

[112] V. Gunenthiram, P. Peyre, M. Schneider, M. Dal, F. Coste, and R. Fabbro. Analysis of laser–melt pool–powder bed interaction during the selective laser melting of a stainless steel. *Journal of Laser Applications*, 29(2):022303, 2017.

[113] T. Fuhrich, P. Berger, and H. Hügel. Marangoni effect in laser deep penetration welding of steel. *Journal of Laser Applications*, 13(5):178–186, 2001.

[114] H. Niu and I. Chang. Instability of scan tracks of selective laser sintering of high speed steel powder. *Scripta Materialia*, 41(11):1229–1234, 1999.

[115] R. Rai, J. W. Elmer, T. A. Palmer, and T. DebRoy. Heat transfer and fluid flow during keyhole mode laser welding of tantalum, Ti–6Al–4V, 304L stainless steel and vanadium. *Journal of Physics D: Applied Physics*, 40(18):5753–5766, 2007.

[116] R. Rai, S. M. Kelly, R. P. Martukanitz, and T. DebRoy. A convective heat-transfer model for partial and full penetration keyhole mode laser welding of a structural steel. *Metallurgical and Materials Transactions A*, 39(1):98–112, 2008.

[117] L. Wang, Q. S. Wei, Y. S. Shi, J. H. Liu, and W. T. He. Experimental investigation into the single-track of selective laser melting of IN625. *Advanced Materials Research*, 233:2844–2848, 2011.

[118] K. Kempen, L. Thijs, J. Van Humbeeck, and J.-P. Kruth. Processing AlSi10Mg by selective laser melting: parameter optimisation and material characterisation. *Materials Science and Technology*, 31(8):917–923, 2015.

[119] P. Wei, Z. Wei, Z. Chen, J. Du, Y. He, J. Li, and Y. Zhou. The AlSi10Mg samples produced by selective laser melting: single track, densification, microstructure and mechanical behavior. *Applied Surface Science*, 408:38–50, 2017.

[120] A. Keshavarzkermani, E. Marzbanrad, R. Esmaeilizadeh, Y. Mahmoodkhani, U. Ali, P. D. Enrique, N. Y. Zhou, A. Bonakdar, and E. Toyserkani. An investigation into the effect of process parameters on melt pool geometry, cell spacing, and grain refinement during laser powder bed fusion. *Optics & Laser Technology*, 116:83–91, 2019.

[121] S. L. Campanelli, G. Casalino, N. Contuzzi, A. Angelastro, and A. D. Ludovico. Analysis of the molten/solidified zone in selective laser melted parts. In *High-Power Laser Materials Processing: Lasers, Beam Delivery, Diagnostics, and Applications III*, vol. 8963, p. 227–234, 2014.

[122] U. Scipioni Bertoli, A. J. Wolfer, M. J. Matthews, J.-P. R. Delplanque, and J. M. Schoenung. On the limitations of volumetric energy density as a design parameter for selective laser melting. *Materials & Design*, 113:331–340, 2017.

[123] J. Ciurana, L. Hernandez, and J. Delgado. Energy density analysis on single tracks formed by selective laser melting with CoCrMo powder material. *The International Journal of Advanced Manufacturing Technology*, 68(5):1103–1110, 2013.

[124] J. Mutua, S. Nakata, T. Onda, and Z.-C. Chen. Optimization of selective laser melting parameters and influence of post heat treatment on microstructure and mechanical properties of maraging steel. *Materials & Design*, 139:486–497, 2018.

[125] M. Zavala-Arredondo, T. London, M. Allen, T. Maccio, S. Ward, D. Griffiths, A. Allison, P. Goodwin, and C. Hauser. Use of power factor and specific point energy as design parameters in laser powder-bed-fusion (L-PBF) of AlSi10Mg alloy. *Materials & Design*, 182:108018, 2019.

[126] J. P. Oliveira, T. G. Santos, and R. M. Miranda. Revisiting fundamental welding concepts to improve additive manufacturing: From theory to practice. *Progress in Materials Science*, 107:100590, 2020.

[127] I. Yadroitsev, I. Yadroitsava, P. Bertrand, and I. Smurov. Factor analysis of selective laser melting process parameters and geometrical characteristics of synthesized single tracks. *Rapid Prototyping Journal*, 18(3):201–208, 2012.

[128] Q. Guo, C. Zhao, M. Qu, L. Xiong, L. I. Escano, S. M. H. Hojjatzadeh, N. D. Parab, K. Fezzaa, W. Everhart, T. Sun, and L. Chen. In-situ characterization and quantification of melt pool variation under constant input energy density in laser powder bed fusion additive manufacturing process. *Additive Manufacturing*, 28:600–609, 2019.

[129] J. C. Gibbings. *Dimensional analysis*. Springer, London, 2011.

[130] V. Simon, B. Weigand, and H. Gomaa. *Dimensional Analysis for Engineers*. Mathematical Engineering. Springer, Cham, 2017.

[131] A. N. Conejo. *Fundamentals of Dimensional Analysis*. Springer, Singapore, 2021.

[132] E. Buckingham. On physically similar systems illustrations of the use of dimensional equations. *Physical Review*, 4(4):345, 1914.

[133] M. Van Elsen, F. Al-Bender, and J.-P. Kruth. Application of dimensional analysis to selective laser melting. *Rapid Prototyping Journal*, 2008.

[134] U. Gratzke, P. D. Kapadia, and J. Dowden. Heat conduction in high-speed laser welding. *Journal of Physics D: Applied Physics*, (24):2125–2134, 1991.

[135] A. Robert and T. DebRoy. Geometry of laser spot welds from dimensionless numbers. *Metallurgical and Materials Transactions B*, 32(5):941–947, 2001.

[136] A. Patschger and J. Bliedtner. Determination and dependencies of melt pool dimensions in laser micro welding. *Physics Procedia*, 83:494–505, 2016.

[137] K. N. Lankalapalli, J. F. Tu, and M. Gartner. A model for estimating penetration depth of laser welding processes. *Journal of Physics D: Applied Physics*, 29(7):1831–1841, 1996.

[138] T. Mukherjee, V. Manvatkar, A. De, and T. DebRoy. Dimensionless numbers in additive manufacturing. *Journal of Applied Physics*, 121(6):064904, 2017.

[139] T. DebRoy and S. A. David. Physical processes in fusion welding. *Review of Modern Physics*, (67):85–112, 1995.

[140] T. Mukherjee and T. DebRoy. Mitigation of lack of fusion defects in powder bed fusion additive manufacturing. *Journal of Manufacturing Processes*, 36:442–449, 2018.

[141] Y. Yang, A. Großmann, P. Kühn, J. Mölleney, L. Kropholler, C. Mittelstedt, and B.-X. Xu. Validated dimensionless scaling law for melt pool width in laser powder bed fusion. *Journal of Materials Processing Technology*, 299:117316, 2022.

[142] R. Fabbro. Analysis and possible estimation of keyhole depths evolution, using laser operating parameters and material properties. *Journal of Laser Applications*, (30):032410, 2018.

[143] D. B. Hann, J. Iammi, and J. Folkes. A simple methodology for predicting laser-weld properties from material and laser parameters. *Journal of Physics D: Applied Physics*, 44(44):445401, 2011.

[144] N. Saunders, U. K. Z. Guo, X. Li, A. P. Miodownik, and J.-P. Schillé. Using JMatPro to model materials properties and behavior. *JOM*, 55(12):60–65, 2003.

[145] M. Mohr, R. Wunderlich, R. Novakovic, E. Ricci, and H.-J. Fecht. Precise measurements of thermophysical properties of liquid Ti–6Al–4V (Ti64) alloy on board the international space station. *Advanced Engineering Materials*, 22(7):2000169, 2020.

[146] J. Trapp, A. M. Rubenchik, G. Guss, and M. J. Matthews. In situ absorptivity measurements of metallic powders during laser powder-bed fusion additive manufacturing. *Applied Materials Today*, 9:341–349, 2017.

[147] G. Pottlacher, H. Hosaeus, B. Wilthan, E. Kaschnitz, and A. Seifter. Thermophysikalische Eigenschaften von festem und flüssigem Inconel 718. *Thermochimica Acta*, 382(1-2):255–267, 2002.

[148] K. Bartsch, D. Herzog, B. Bossen, and C. Emmelmann. Material modeling of Ti–6Al–4V alloy processed by laser powder bed fusion for application in macro-scale process simulation. *Materials Science and Engineering: A*, 814:141237, 2021.

[149] M. Boivineau, C. Cagran, D. Doytier, V. Eyraud, M.-H. Nadal, B. Wilthan, and G. Pottlacher. Thermophysical properties of solid and liquid Ti-6Al-4V (TA6V) alloy. *International Journal of Thermophysics*, 27(2):507–529, 2006.

[150] ISO/TR 11146-3:2004-02, Lasers and laser-related equipment - Test methods for laser beam widths, divergence angles and beam propagation ratios - Part 3: Intrinsic and geometrical laser beam classification, propagation and details of test methods.

[151] C. A. Schneider, W. S. Rasband, and K. W. Eliceiri. NIH Image to ImageJ: 25 years of image analysis. *Nature methods*, 9(7):671–675, 2012.

[152] DIN EN ISO 3369:2010-08, Undurchlässige Sintermetallwerkstoffe und Hartmetalle - Ermittlung der Dichte (ISO 3369:2006).

[153] B. J. Simonds, J. Tanner, A. Artusio-Glimpse, P. A. Williams, N. Parab, C. Zhao, and T. Sun. The causal relationship between melt pool geometry and energy absorption measured in real time during laser-based manufacturing. *Applied Materials Today*, 23:101049, 2021.

[154] F. Dausinger. *Strahlwerkzeug Laser: Energieeinkopplung und Prozeßeffektivität*. Habilitation, University Stuttgart, Stuttgart, 1995.

[155] F. Cardarelli. *Materials handbook: A concise desktop reference*. Springer, London, 2. edition, 2008.

[156] M. J. Assael, A. E. Kalyva, K. D. Antoniadis, R. Michael Banish, I. Egry, J. Wu, E. Kaschnitz, and W. A. Wakeham. Reference data for the density and viscosity of liquid copper and liquid tin. *Journal of Physical and Chemical Reference Data*, 39(3):033105, 2010.

[157] T. Matsumoto, H. Fujii, T. Ueda, M. Kamai, and K. Nogi. Measurement of surface tension of molten copper using the free-fall oscillating drop method. *Measurement Science and Technology*, 16(2):432–437, 2005.

[158] J. Wisniewski, J.-M. Drezet, D. Ayrault, and B. Cauwe. Determination of the thermophysical properties of a CuCr1Zr alloy from liquid state down to room temperature. *International Journal of Material Forming*, 1(1):1059–1062, 2008.

[159] P. Tolias. Analytical expressions for thermophysical properties of solid and liquid tungsten relevant for fusion applications. *Nuclear Materials and Energy*, 13:42–57, 2017.

[160] G. Pottlacher. Thermal conductivity of pulse-heated liquid metals at melting and in the liquid phase. *Journal of Non-Crystalline Solids*, 250:177–181, 1999.

[161] J. W. Arblaster. Thermodynamic properties of tungsten. *Journal of Phase Equilibria and Diffusion*, 39(6):891–907, 2018.

[162] M. Khorasani, A. Ghasemi, M. Leary, W. O'Neil, I. Gibson, L. Cordova, and B. Rolfe. Numerical and analytical investigation on meltpool temperature of laser-based powder bed fusion of IN718. *International Journal of Heat and Mass Transfer*, 177:121477, 2021.

[163] L. Scime and J. Beuth. Melt pool geometry and morphology variability for the Inconel 718 alloy in a laser powder bed fusion additive manufacturing process. *Additive Manufacturing*, 29:100830, 2019.

[164] L. Sinclair, C. L. A. Leung, S. Marussi, S. J. Clark, Y. Chen, M. P. Olbinado, A. Rack, J. Gardy, G. J. Baxter, and P. D. Lee. In situ radiographic and ex situ tomographic analysis of pore interactions during multilayer builds in laser powder bed fusion. *Additive Manufacturing*, 36:101512, 2020.

[165] M. Miyagi, H. Wang, R. Yoshida, Y. Kawahito, H. Kawakami, and T. Shoubu. Effect of alloy element on weld pool dynamics in laser welding of aluminum alloys. *Scientific reports*, 8(1):12944, 2018.

[166] S. Cornell and K. Hartke. Humping reduction methods for high speed laser welding. In *International Congress on Applications of Lasers & Electro-Optics*, p. 985–989, Orlando, 2009.

[167] A. F. de Souza, K. S. Al-Rubaie, S. Marques, B. Zluhan, and E. C. Santos. Effect of laser speed, layer thickness, and part position on the mechanical properties of maraging 300 parts manufactured by selective laser melting. *Materials Science and Engineering: A*, 767:138425, 2019.

[168] A. Leicht, M. Fischer, U. Klement, L. Nyborg, and E. Hryha. Increasing the productivity of laser powder bed fusion for stainless steel 316L through increased layer thickness. *Journal of Materials Engineering and Performance*, 30(1):575–584, 2021.

[169] D. Jansen, T. Hanemann, M. Radek, A. Rota, J. Schröpfer, and M. Heilmaier. Development of actual powder layer height depending on nominal layer thicknesses and selection of laser parameters. *Journal of Materials Processing Technology*, 298:117305, 2021.

[170] D. S. Jansen. *Quantifizierung des Einflusses der Pulverschichtdicke auf den DMLS Prozess*. Master thesis, University of Applied Sciences Munich, Munich, 2020.

List of figures

List of tables

A Appendix

A.1 Determination of effective layer thickness

The methodology and experimental setup to measure the effective powder layer thickness (EPLT) described in Section 2.1.2.1 was developed in the frame of a master thesis by Deniz Jansen [170] and results are partially published in [169].

To apply a realistic powder layer thickness for single layer experiments, the effective powder layer thickness was experimentally determined for the $40\,\mu m$ EOS M290 standard processes of IN718 and MS1, as well as the $30\,\mu m$ EOS M290 standard processes of AlSi10Mg. In addition, samples were built with $30\,\mu m$ nominal layer thickness for IN718 and MS1, and $40\,\mu m$ nominal layer thickness for AlSi10Mg to compare results. Furthermore, samples with the standard IN718 parameters were built at nominal layer thickness of $60\,\mu m$ and $80\,\mu m$. The sample geometry to experimentally determine h_{pow} is shown in Figure A.1. The geometry was chosen in accordance with the sample geometry from Wischeropp et al. [58], consisting of a staircase in the center with single step height similar to l_t. The outer frame was added as reference surface for the measurement and to ensure powder to stay within the measurement area during unpacking. A sample height of $3\,mm$ was chosen to ensure that all steps in the stair geometry were in steady state. The sample geometry was built upon a round build plate of $100\,mm$ diameter screwed on to the standard EOS M290 build plate to enable sample removal and measurement after the build

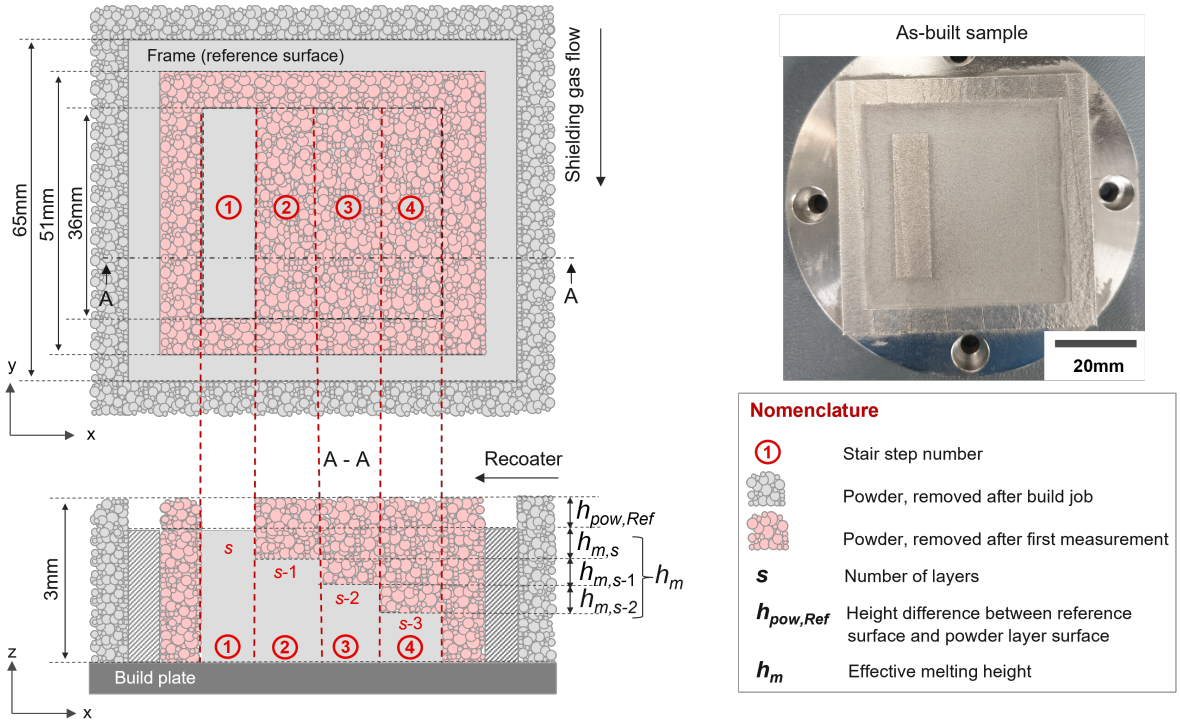

Figure A.1: Experimental setup for EPLT measurements

job. The gray powder marked in the schematic drawing was removed after the build finished, while powder in the red area was kept untouched for measurement (see photograph in Figure A.1). Surface topography of the as-built sample with powder was measured using a Keyence VR3200 3D profilometer. The height difference between reference surface (outer frame and step 1) and powder layer surface, corresponding to $h_{pow,Ref}$, was determined as the average height difference from several line profile measurements. After this measurement, all powder was removed from the sample and the height profile of the staircase geometry was measured. The effective melting height h_m was determined for each stair step and the average calculated. The EPLT h_{pow} was then calculated as the sum of $h_{pow,Ref}$ and h_m.

Results for the M290 standard processes of IN718, MS1 and AlSi10Mg built with l_t = 30 µm and l_t = 40 µm, as well as l_t = 60 µm and l_t = 80 µm for IN718, are shown in Figure A.2. As expected, effective melting heights h_m are close to l_t, verifying that samples were in steady state condition. The EPLT h_{pow} is similar for IN718 and MS1 at both nominal layer thicknesses, while h_{pow} is lower for AlSi10Mg in both cases. The absolute values of EPLT h_{pow} change with l_t, and therefore the ratio of h_{pow}/l_t should be taken into account when comparing EPLTs. For AlSi10Mg this ratio does not change significantly (30 µm: 3.4, 40 µm: 3.5), while for IN718 and MS1 it increases from about 4.7 at 40 µm to 5.3 for IN718 and 5.5 for MS1 at 30 µm. Thus, at similar applied powder layer thickness, a higher amount of powder contributes to material consolidation for AlSi10Mg compared to IN718 and MS1. The graphs shows that the applied powder layer thickness of 190 µm used in the single scan track experiments corresponds to the EPLT of the 40 µm standard processes for IN718 and MS1. However, it is equivalent to higher nominal layer thickness for AlSi10Mg. This difference in EPLT to l_t ratio has to be taken into account, when comparing the presented single scan track results with observations from

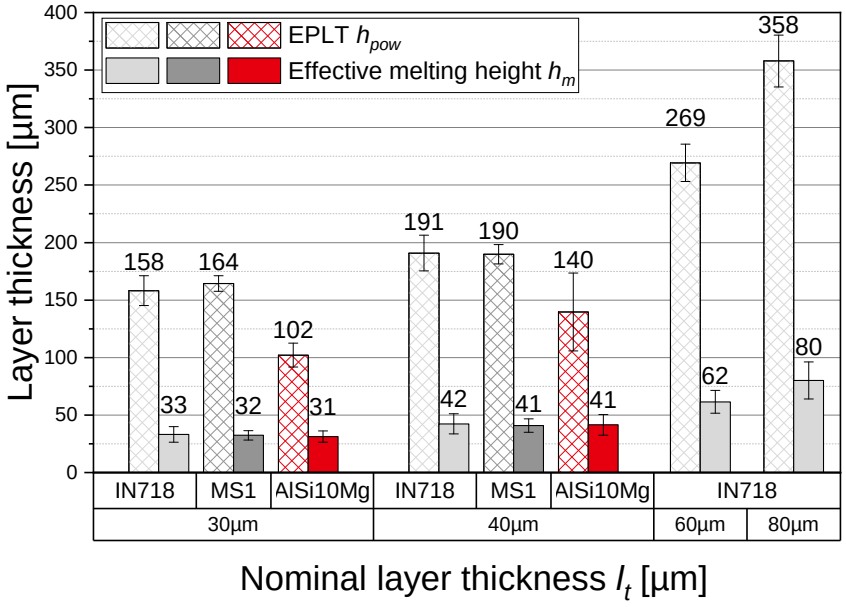

Figure A.2: Effective powder layer thicknesses h_{pow} and effective melting heights h_m for IN718, MS1, and AlSi10Mg built with M290 standard processes at different nominal layer thicknesses

multilayer builds. The applied powder layer thicknesses of $290\,\mu m$ and $390\,\mu m$ used to estimate the influence of a change in powder layer thickness on melt pool dimensions (Section 3.2.3, Section 4.2.4) approximately correspond to nominal layer thicknesses of $60\,\mu m$ and $80\,\mu m$ at standard conditions.

A.2 Process maps

Process maps for MS1, 316L, Ti64, and AlSi10Mg are shown in Figure A.3. Single scan tracks are labeled as stable if they do not obtain surface instabilities according to Section 3.3.3 and do not contain any keyhole porosity. Trendlines for two values of H^*_{cd} are exemplarily indicated. The respective values were calculated based on $a = 80\,\mu\mathrm{m}$ with the yellow areas indicating $\pm$ 5% beam diameter variation. Additionally, dynamic and Pe cut-off speeds are marked as red and blue lines. For MS1, 316L and Ti64 the Pe cut-off is taken as $Pe = 4$, while for AlSi10Mg a value of $Pe = 1.8$ was chosen based on the observed shift in Pe transition value in Section 4.1.2.3.

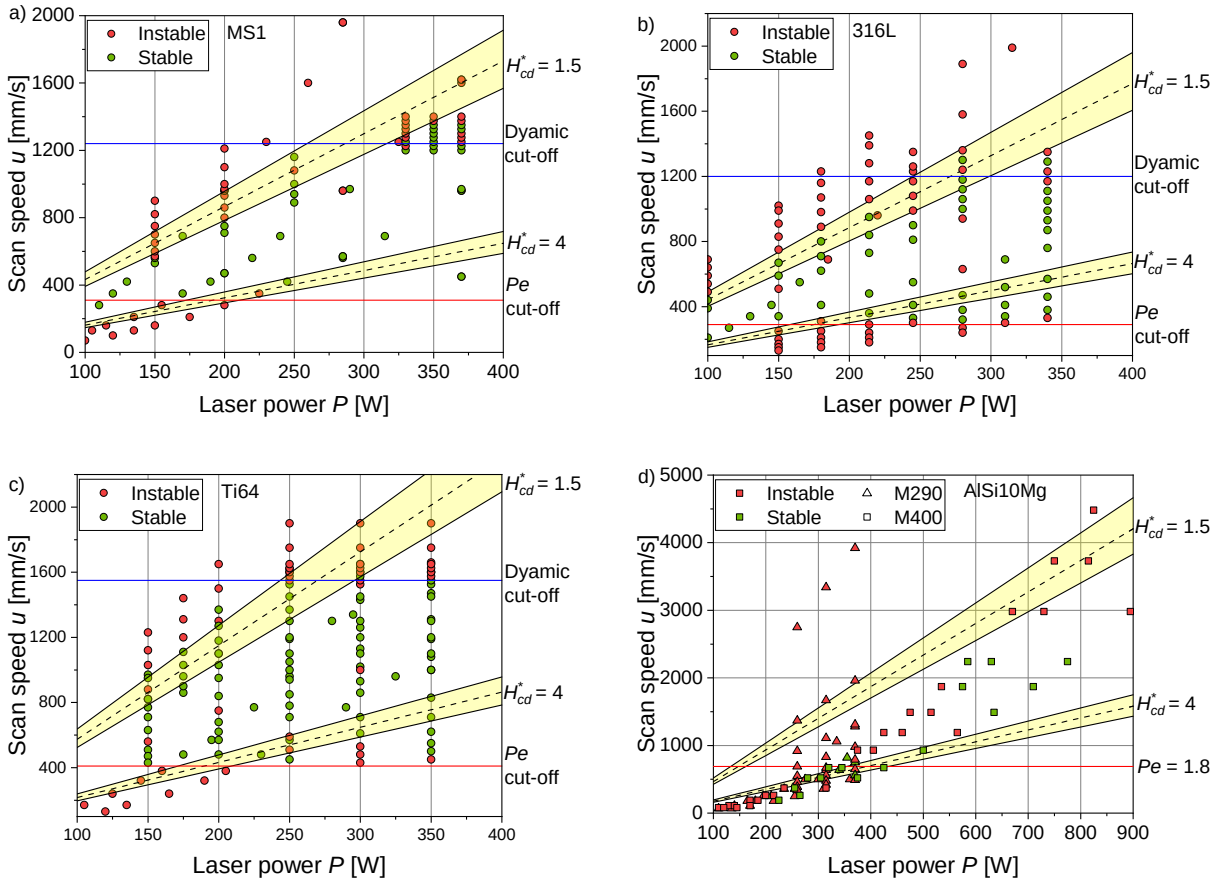

Figure A.3: Experimental process maps for single scan tracks of a) MS1, b) 316L, c) Ti64, and d) AlSi10Mg

A.3 Logistic regressions for process boundary evaluation

Table A.1: Summary of logistic regression fits for process boundary evaluation of the investigated alloys and logistic regression fit for the combined process window of IN718, MS1, 316L, and Ti64 denoted General; $p(2)$ represents the probability to obtain a stable and defect free single scan track

	Lower boundary	Upper boundary
IN718	$p(2) = \frac{\exp(-7.52+5.31H^*_{cd})}{1+\exp(-7.52+5.31H^*_{cd})}$	$p(2) = \frac{\exp(6.87-1.455H^*_{cd})}{1+\exp(6.87-1.455H^*_{cd})}$
MS1	$p(2) = \frac{\exp(-7.65+4.84H^*_{cd})}{1+\exp(-7.65+4.84H^*_{cd})}$	$p(2) = \frac{\exp(8.98-1.78H^*_{cd})}{1+\exp(8.98-1.78H^*_{cd})}$
316L	$p(2) = \frac{\exp(-5.56+3.391H^*_{cd})}{1+\exp(-5.56+3.391H^*_{cd})}$	$p(2) = \frac{\exp(7.81-1.126H^*_{cd})}{1+\exp(7.81-1.126H^*_{cd})}$
Ti64	$p(2) = \frac{\exp(-3.982+3.289H^*_{cd})}{1+\exp(-3.982+3.289H^*_{cd})}$	$p(2) = \frac{\exp(5.69-1.135H^*_{cd})}{1+\exp(5.69-1.135H^*_{cd})}$
AlSi10Mg	$p(2) = \frac{\exp(-5.3+1.738H^*_{cd})}{1+\exp(-5.3+1.738H^*_{cd})}$	
General	$p(2) = \frac{\exp(-4.875+3.416H^*_{cd})}{1+\exp(-4.875+3.416H^*_{cd})}$	$p(2) = \frac{\exp(6.262-1.195H^*_{cd})}{1+\exp(6.262-1.195H^*_{cd})}$

A.4 Process parameter combinations for density cubes

Table A.2: Parameter sets for IN718 density cubes; h_d = 110 µm, l_t = 40 µm

PS	Laser power P [W]	Scan speed u [mm/s]	Dimensionless enthalpy H^* [-]	Peclet number Pe [-]	Depth corrected dimensionless enthalpy H^*_{cd} [-]
1	315	1050	9.5	18.7	2.2
2	300	960	9.4	17.1	2.3
3	158	470	7.1	8.4	2.4
4	354	820	12.0	14.6	3.1
5	236	580	9.5	10.3	3.0
6	370	960	11.6	17.1	2.8
7	202	410	9.7	7.3	3.6
8	266	500	11.6	8.9	3.9
9	305	580	12.3	10.3	3.8
10	276	470	12.4	8.4	4.3

Work-related publications

- **T. Hanemann**, C. Seyfert, P. Holfelder, A. Rota, and M. Heilmaier. Dimensionless enthalpy as characteristic factor for process control in laser powder bed fusion. *Journal of Laser Micro/Nanoengineering*, 15(3):257–266, 2020.
- Ref. [169]: D. Jansen, **T. Hanemann**, M. Radek, A. Rota, J. Schröpfer, and M. Heilmaier. Development of actual powder layer height depending on nominal layer thicknesses and selection of laser parameters. *Journal of Materials Processing Technology*, 298:117305, 2021.

Eigenständigkeitserklärung

Eidesstattliche Versicherung gemäß § 13 Absatz 2 Satz 2 Ziffer 3 der Promotionsordnung des Karlsruher Instituts für Technologie (KIT) für die KIT-Fakultät für Maschinenbau.

Bei der eingereichten Dissertation zu dem Thema

Usability and limitations of dimensionless scaling laws in Laser Powder Bed Fusion

handelt es sich um meine eigenständig erbrachte Leistung. Ich habe nur die angegebenen Quellen und Hilfsmittel benutzt und mich keiner unzulässigen Hilfe Dritter bedient. Insbesondere habe ich wörtlich oder sinngemäß aus anderen Werken übernommene Inhalte als solche kenntlich gemacht. Die Arbeit oder Teile davon habe ich bislang nicht an einer Hochschule des In- oder Auslands als Bestandteil einer Prüfungs- oder Qualifikationsleistung vorgelegt.

Die Richtigkeit der vorstehenden Erklärungen bestätige ich. Die Bedeutung der eidesstattlichen Versicherung und die strafrechtlichen Folgen einer unrichtigen oder unvollständigen eidesstattlichen Versicherung sind mir bekannt.

Ich versichere an Eides statt, dass ich nach bestem Wissen die reine Wahrheit erklärt und nichts verschwiegen habe.

Ort, Datum	Unterschrift

Acknowledgments

I want to thank everyone who supported me during my time as a PhD student at EOS and the preparation of this work. Special thanks go to Prof. Dr.-Ing. Martin Heilmaier and Dr. Astrid Rota for the possibility to do this industrial doctoral dissertation at EOS Electro Optical Systems GmbH in cooperation with the Institute for Applied Materials at the Karlsruher Institute of Technology. Furthermore, I want to thank for their guidance and continually constructive feedback. Moreover, I want to thank Prof. Xinhua Wu for taking the time and interest to review this work as a co-referee.

I want to thank the whole Metal Process Technology team at EOS for the supportive and productive environment. It was a pleasure to work with all of you and I hope you all will maintain this great work atmosphere. Special thanks go to Christoph Seyfert who helped me find my place at EOS and was always in for fruitful scientific discussions, Sebastian Edelhäuser for experimental advice and encouragement, Markus Radek for support in understanding PDE and EOSPrint issues, and Alexander Frey for helpful discussions and motivation. I want to thank Sebastian Kalka for taking the time to explain and support in laser beam caustic measurements, especially on the M4 system. Many thanks also go to my fellow PhD students Tino Pfalz and Philipp Stich for coffee break and lunch walk distractions.

Furthermore, I want to thank the whole administrative PhD-team and PhD students from other groups at EOS, especially Jens Sesseg for always having some motivating words and Vincenzo Abbatiello for the great collaboration and for all the lunches I could share with him and his team (and also some cooking tips). Further, I want to thank my two master students Deniz Jansen and Cécile Laverrière for their support on side topics related to this work.

Many thanks also to the workshop team, especially Zafer Bicer and Bernd Tönert for the large amount of substrate plates carefully and timely milled. Moreover, I want to thank the supporters for machine preparation and laboratory team for support in sample preparation and microscopy. Special thanks go to Omed Murad and Sebastian Bogen who never became tired helping when laboratory equipment didn't work and explaining measurement procedures.

At last I want to thank my friends and family, especially my husband Michael, for believing in me and supporting me during this time.

> The greatest enemy of knowledge is not ignorance, it is the illusion of knowledge.
>
> *Daniel J. Boorstin*